Modelling hydrologically relevant structures and processes of the initial development phase of a man-made catchment

Von der
Fakultät Architektur, Bauingenieurwesen und Umweltwissenschaften
der Technischen Universität Carolo–Wilhelmina
zu Braunschweig

zur Erlangung des Grades eines
Doktors der Naturwissenschaften (Dr. rer. nat.)
genehmigte

Dissertation

von
Markus Hofer
geboren am 25. Juni 1979
aus Zürich

Eingereicht am	24. November 2011
Disputation am	19. Dezember 2011
Berichterstatter	Prof. Dr. Manfred Krafczyk
	Prof. Dr. Wolfgang Durner

2012

Eidesstattliche Erklärung

Name: Markus Hofer
Geburtsdatum / -ort: 25. Juni 1979 / Zürich
Strasse: Im Eisernen Zeit 12
Ort: 8057 Zürich / Schweiz

Hiermit erkläre ich an Eides statt, dass ich die vorgelegte Dissertation mit dem Titel

Modelling hydrologically relevant structures and processes of the initial development phase of a man-made catchment

selbstständig verfasst, nicht schon als Diplom- oder Prüfungsarbeit verwendet und alle in Anspruch genommenen Hilfen in der Dissertation angegeben habe.

Ich versichere an Eides statt, dass ich diesen Promotionsantrag erstmalig einreiche und keine früheren Versuche einer Promotion unternommen habe.

Zürich, 15. Mai 2012

Summary

The present dissertation deals with the model-based investigation of hydrologically relevant structures and processes of the initial development phase of the man-made catchment ‘Chicken Creek’. The 6 ha large catchment located near Cottbus (Germany) was completed in autumn 2005 and since has been left to an undirected and undisturbed primary succession. Based on field observations and the development of new models, a set of hydrologically important structures and processes could be identified.

A highly nonlinear relationship between measured rainfall and total runoff was revealed in the catchment. Runoff shows a threshold-like behaviour and was only triggered for precipitation events with a total rainfall larger than 9 mm. Apparently, preferential subsurface flow paths exist, which connect only after a critical amount of rainfall. In the first part of the thesis, a new model based on Percolation Theory was developed to simulate the subsurface flow paths and the nonlinear catchment runoff response to rainfall. The sudden establishment of a high hydrologic connectivity between the soil elements of the catchment is shown to be the key factor to explain the threshold-like behaviour of the runoff response to rainfall.

In contrast to most mature hydrological catchments in temperate areas, surface water flow is an important runoff process of the initial development phase of the Chicken Creek catchment. This becomes evident from the evolution of erosion rills driven by surface runoff in the first few years after completion of the catchment. The development of the erosion rill network was characterised by a nonlinear function describing rapid rill growth in the first year and successively declining growth in following years. In the second part of the thesis, two models using different approaches were developed to describe the emergence of the erosion rills. First, we used a self-organised critical network approach with soil erosion and sediment deposition governed by a local critical shear stress. The second approach was based on the computation of particle transport as function of flow velocity determined by the Manning equation. The Manning-based model was developed to compare the results of the self-organised critical network approach with results from a simple, but more physically-based approach. Both models were able to qualitatively reproduce the observed main rill network. Geometric characteristics, such as rill network length and rill depth were simulated in the right order of magnitude compared to measurements. The models also succeeded in describing the position and the temporal evolution of the erosion rills in the catchment. The simulations further showed that erosion and deposition processes forced the surface flow paths to change gradually during rill evolution. However, surface flow paths were only locally affected by the growth of the erosion rills. Thus, the mature rill network is largely the result of the very initial surface micro-topography of the catchment.

The development of both types of structures, the water flow paths (surface and subsurface) and the surface erosion rills can be regarded as emergent patterns, that is macro-scale structures, which develop from micro-scale processes, but are entirely unpredictable only from these. Most current hydrological models fail in describing the emergence of these hydrologically relevant macro-scale patterns or the non-linear processes such as the threshold-like runoff-rainfall response observed in the catchment. In the third part of the thesis, a new hydrological model was conceptualised to tackle these drawbacks of present models. By describing water transport in discrete volume units, the new model was able to represent (nonlinear) runoff processes, water transit times and the emergence of macro-scale patterns in the same model framework. First model simulations were able to reproduce realistic surface runoff patterns and transit times and to simulate the temporal evolution of subsurface flow paths. Comparing simulation runs with and without erosion rills revealed that the rills have a distinctive effect on the quantity of the runoff components, and on the flow distances, flow times and flow velocities of the surface water. The increased local topographic gradients along the rills promoted flow of surface water to the rills from where it was effectively transported to the catchment outlet. Therefore, the volume, transport distances and velocities of the surface water were generally higher for the topography with rills. These first model simulation results demonstrate the practicability of the new model concept and provide an encouraging basis for the further enhancement of the model.

Zusammenfassung

Die vorliegende Dissertation behandelt die modellgestützte Untersuchung hydrologisch relevanter Strukturen und Prozesse in der initialen Entwicklungsphase des künstlich geschaffenen Einzuggebiets ‘Hühnerwasser’ (auf Englisch ‘Chicken Creek’). Das 6 ha umfassende Einzugsgebiet, welches in der Nähe von Cottbus (Deutschland) liegt, wurde im Herbst 2005 fertiggestellt und wurde seither einer ungerichteten und ungestörten Primärsukzession überlassen. Gestützt auf Beobachtungen und Messungen im Feld, sowie auf der Entwicklung neuer Modelle konnte eine Reihe hydrologisch wichtiger Strukturen und Prozesse identifiziert werden.

Im Einzugsgebiet wurde ein stark nichtlinearer Zusammenhang zwischen gemessenem Niederschlag und Gesamtabfluss beobachtet. Der Abfluss zeigte ein deutliches Schwellwertverhalten und wurde nur für Niederschlagsereignisse mit einem Gesamtniederschlag von über 9 mm initiiert. Offensichtlich existieren präferentielle Fliesspfade im Einzugsgebiet, die sich nur bei einer kritischen Menge von Niederschlag miteinander verbinden und dann für schnellen Abfluss sorgen. Im ersten Teil dieser Arbeit wurde ein neues perkolationstheoretisches Modell entwickelt, mit dem Ziel unterirdische Fliesspfade und das gegenüber dem Niederschlag nichtlineare Verhalten von Gebietsabfluss zu simulieren. Das plötzliche Eintreten einer hohen hydrologischen Konnektivität zwischen Bodenelementen des Einzugsgebiets wurde dabei als Schlüsselfaktor zur Erklärung des Schwellwertverhaltens des Gebietsabfluss ermittelt.

Im Gegensatz zu den meisten Einzugsgebieten, die sich in gemässigten Klimaregionen natürlich entwickelt haben, ist Wasserfluss an der Bodenoberfläche eine wichtige Abflusskomponente in der initialen Entwicklungsphase des Hühner-

wassers. Dies erkennt man deutlich an den Erosionsrillen, die sich in den ersten Jahren nach der Fertigstellung des Einzugsgebiets durch Oberflächenabfluss gebildet haben. Die Entwicklung des Erosionsrillennetzwerks folgte einer nichtlinearen Funktion mit intensivem Wachstum der Rillen im ersten Jahr und allmählich nachlassendem Wachstum in den folgenden Jahren. Im zweiten Teil der Arbeit wurden zwei verschiedene Modelle entwickelt, um die Entstehung der Erosionsrillen zu beschreiben. Das erste Modell basiert auf dem Prinzip der selbstorganisierten Kritikalität. Erosion und Deposition werden dabei durch die Über-, bzw. Unterschreitung der lokalen kritischen Scherspannung bestimmt. Das zweite Modell simuliert Sedimenttransport basierend auf der Fliessgeschwindigkeit des Oberflächenflusses, die im Modell mit der Manning-Gleichung beschrieben wurde. Dieses Modell wurde entwickelt um die Resultate des ersten Modells mit jenen eines einfachen aber physikalisch basierten Ansatzes zu vergleichen. Beide Modelle waren in der Lage das gemessene Rillennetzwerk qualitativ abzubilden. Geometrische Eigenschaften, wie die Länge oder die Tiefe der Erosionsrillen wurden, im Vergleich zu den Messungen, von den Modellen in der richtigen Grössenordnung wiedergegeben. Zudem konnten die Modelle die räumliche und zeitliche Entwicklung der Erosionsrillen erfolgreich vorhersagen. Die Simulationen zeigten, dass sich das räumliche Muster der Oberflächenabflusspfade mit der Rillenentwicklung änderte. Das Wachstum der Rillen wirkte sich jedoch nur lokal auf das Fliesspfadmuster aus. Infolgedessen ist das vollentwickelte Rillennetzwerk das Resultat der initialen Mikrotopographie der Bodenoberfläche des Einzugsgebiets.

Beide Strukturtypen, die Fliesspfade (im Untergrund und an der Oberfläche), sowie auch die Erosionsrillen lassen sich als emergente Muster bezeichnen, dass heisst Muster auf der Makroskala, die sich aufgrund von mikroskaligen Prozessen entwickeln, die aber alleine durch diese Prozesse nicht vorhersagbar sind. Die meisten gegenwärtigen hydrologischen Modelle vermögen weder die Entwicklung von emergenten Mustern noch nichtlinearen Prozesse (wie zum Beispiel das Schwellwertverhalten des Gebietsabfluss) abzubilden. Im dritten Teil der Arbeit wurde ein neues hydrologisches Modell konzipiert, um diese Nachteile gegenwärtiger hydrologischer Modelle in Angriff zu nehmen. Durch die Beschreibung des Wassertransportes in diskreten Volumeneinheiten ist das neue Modell in der Lage (nichtlineare) Abflussprozesse, Wassertransportzeiten und die Entwicklung von emergenten Mustern in ein und derselben Modellstruktur zu beschreiben. Erste Modelsimulationen konnten realistische Oberflächenabflussmuster, Transportzeiten von Wasser und die zeitliche Entwicklung von unterirdischen Fliesspfaden nachbilden. Der Vergleich zwischen zwei Simulationen, eine ohne und eine mit Erosionsrillen, zeigte, dass die Erosionsrillen einen deutlichen Effekt auf die Quantität der Abflusskomponenten, sowie auf die zurückgelegte Distanz, die Zeit und die Geschwindigkeit des Wasserflusses auf der Oberflächen haben. Durch die Erosion erhöhten sich die lokalen topographischen Gradienten um die Rillen, wodurch der Wasserfluss in die Rillen verstärkt wurde. Deshalb waren Volumen, Transportdistanz und Geschwindigkeit des Oberflächenwassers generell höher für die Simulation, die die Erosionsrillen berücksichtigte. Diese ersten Modellresultate zeigen die Realisierbarkeit des neuen Modellkonzepts und stellen eine ermutigende Basis für die Weiterentwicklung des Modells dar.

Acknowledgements

- I owe my deepest gratitude to my supervisor **Dr. Peter Lehmann** (ETH Zurich) for his never-ending patience, support and helpful advice. Peter has always been a great mentor and a source of constant encouragement.

- I am highly grateful to my supervisor **Dr. Manfred Stähli** (WSL Birmensdorf) for giving me the opportunity to work in his team and for keeping his door open to any of my questions.

- I also wish to express my gratitude to **Prof. Dr. Manfred Krafczyk** (TU Braunschweig) for letting me do this thesis under his supervision and for the helpful comments on my work.

- The compilation of this thesis would not have been possible without my colleagues at the TU Cottbus, who made their help available in many ways. I would like to thank …

  … **Dr. Werner Gerwin**, project coordinator of the Transregional Collaborative Research Centre (SFB/TRR 38) for his helpful support to all kinds of enquiries concerning the field site.

  … **Anna Schneider** and **Dr. Thomas Maurer** for providing the Digital Elevation Models of the field site, which are an essential data set for this thesis.

  … **Kai Mazur** and **Dr. Detlef Biemelt** for informative insights into the hydrological behaviour of the field site and for the help with hydrological and meteo data.

… **Michael Elmer** for always guaranteeing quick and reliable data transfers.

… **Dr. Hartmut Holländer** for interesting discussions on modelling the hydrology of the field site.

… the field staff in Cottbus, especially **Rossen Nenov** and **Silvio Vogt** for their support with data collection.

- Sincere thanks are given to **Stefan Seifert** (TU München) for the fruitful collaboration and for the laser scanning data.

- I am grateful to **Dr. Jan Hegewald** (TU Braunschweig) for his very helpful crash course in programming.

- Many thanks to **Prof. Dr. em. Hannes Flühler** (ETH Zurich), who has always been very positive and supportive about my work.

- It is a pleasure to thank **Bruno Fritschi** (WSL Birmensdorf) for his help with measurement devices.

- I am greatly indebted to my parents, **Edith Hofer** and **Karl Hofer**, for their constant support of my ideas and for offering me a solid education.

- Last but not least, I am very grateful to **Simone Ammann**, who probably best perceived all my thesis-related ups and downs during the last few years. I greatly appreciate her unlimited patience and the freedom she offered me to achieve my goals.

- This study is part of the Transregional Collaborative Research Centre 38 (SFB/TRR 38), which is financially supported by the **German Research Foundation** (DFG, Bonn) and the Brandenburg Ministry of Science, Research and Culture (MWFK, Potsdam). I would also like to thank **Vattenfall Europe Mining AG** for providing the research site.

Contents

List of Figures **15**

List of Tables **19**

List of Symbols **21**

1 Introduction **25**

1.1 Background. 25

1.2 Contents and focus of the thesis 26

1.3 Model aspects 29

2 Experimental site **31**

2.1 Location 31

2.2 Catchment design 31

2.3 Soil properties 34

2.3.1 Soil texture 34

2.3.2 Soil hydraulic properties 35

2.4 Hydrological characteristics of the Chicken Creek catchment 37

2.4.1 Rainfall threshold for catchment runoff 37

2.4.2 Subsurface flow across the clay wall 39

2.4.3 Surface erosion structures 42

3 Subsurface drainage pathways 47
3.1 Motivation 47
3.2 Application of Percolation Theory 49
3.2.1 Basic concept of Percolation Theory 49
3.2.2 Model adaption to hillslope geometry 52
3.2.3 Percolation threshold of hillslope model 52
3.2.4 Definition of occupation probability and drainage capacity in a hillslope model 56
3.3 Results 59
3.3.1 Characterisation of drainage pathways 59
3.3.2 Controls on the development of drainage pathways 61
3.3.3 Outflow 63
3.4 Discussion 64
3.4.1 Drainage pathways. 64
3.4.2 Model assumptions 66
3.4.2.1 Model structure 66
3.4.2.2 Water content 67
3.4.2.3 Water flow 67
3.4.2.4 Soil properties 68
3.5 Conclusions. 69

4 The emergence of surface erosion rills 71
4.1 Motivation 71
4.2 Model description and methods 74
4.2.1 Self-organised critical network (SOCN) model 75
4.2.1.1 Representation of the surface flow paths 76
4.2.1.2 Erosion and deposition 76
4.2.1.3 Delineating the surface flow network 79
4.2.2 Manning-based (MB) model 79
4.2.2.1 Modelling surface water flow 80

4.2.2.2 Erosion and deposition 82
4.2.2.3 Delineating the surface flow network 84
4.2.2.4 Quantifying the surface flow network 84
4.2.2.5 Quantifying the rill network 85
4.3 Results 87
4.3.1 Surface flow networks 87
4.3.2 Rill networks 88
4.3.3 Simulated rill network evolution 93
4.3.4 Change of surface flow patterns 94
4.4 Discussion 96
4.4.1 Surface flow networks 96
4.4.2 Erosion rills. 97
4.4.3 Rill network evolution and stability 98
4.4.4 Sensitivity of free parameters. 99
4.4.4.1 Parameters in the SOCN model 99
4.4.4.2 Parameters in the Manning-based model 100
4.5 Conclusions. 101

5 A new model concept to describe catchment-scale water flow . . 103
5.1 Motivation 103
5.2 Model description 106
5.2.1 Model grid 106
5.2.2 Water flow as transport of water elements 107
5.2.3 Potential water transport capability: From continuous to discrete water flow 108
5.2.4 Infiltration 109
5.2.5 Surface flow. 111
5.2.6 Subsurface flow. 111
5.2.7 Model time step 111

- 5.3 Model setup . . . 112
  - 5.3.1 Random distribution of soil characteristics . . . 112
  - 5.3.2 Initial soil water content . . . 112
  - 5.3.3 Rainfall input and catchment outlet . . . 113
  - 5.3.4 Adaptation of the surface saturated hydraulic conductivity . . 113
  - 5.3.5 Simulations . . . 114
- 5.4 Results . . . 115
  - 5.4.1 Surface runoff . . . 115
  - 5.4.2 Subsurface flow. . . . 120
- 5.5 Discussion . . . 123
  - 5.5.1 Practicability of the new model concept. . . . 123
  - 5.5.2 Open issues concerning the current model state . . . 124
    - 5.5.2.1 Subsurface flow . . . 124
    - 5.5.2.2 Surface flow . . . 125
    - 5.5.2.3 Validation against measurements . . . 126
    - 5.5.2.4 Effect of discretisation. . . . 126
- 5.6 Summary . . . 127

6 Future work in the light of current issues in hydrological catchment modelling . . . 129

- 6.1 Modelling hydrological processes . . . 129
- 6.2 Application of small-scale equations . . . 130
- 6.3 Model validation . . . 131
- 6.4 Model uncertainty . . . 132

References . . . 135

Currivulum vitae . . . 149

Appendix . . . 151

List of Figures

2.1 Construction of the field site Chicken Creek. (a) Overview of the Chicken Creek catchment after completing the construction work in September 2005. (b – d) Different steps during construction 32

2.2 Overview of the catchment geometry. Digital elevation model of (a) the catchment surface and (b) the clay layer. (c) Longitudinal cross-section through the catchment 33

2.3 Location of the soil texture samples in the soil texture triangle of the United States Department of Agriculture (USDA) 35

2.4 Relation between the saturated hydraulic conductivity K_s and the two van Genuchten parameters α and n 36

2.5 Soil hydraulic properties deduced from soil texture using transfer functions for the sample with the highest (96 %) and the lowest sand fraction (66 %), respectively 36

2.6 Rainfall threshold to trigger catchment runoff for the period between the 21^{st} of February 2007 and the 4^{th} of August 2009. (a) Relationship between cumulated precipitation ($\sum P$) and cumulated total catchment runoff ($\sum Q_{tot}$). (b) Sum curves for precipitation and catchment runoff 38

2.7 Aerial picture showing the location of the clay wall and the surface moisture pattern as indicator for flow across the clay wall 40

2.8 Precipitation, subsurface runoff measured at the weir in the clay wall and soil moisture difference index $\Delta\theta$ between the 4th of July 2008 and the 26th of December 2008 41

2.9 Overview of the man-made catchment Chicken Creek (aerial image from June 2007) with erosion rills visible at the footslope. Insets: Erosion rills developed in the catchment 43

2.10 Erosion rill evolution with time. (a) Backbone of the rill network extracted from aerial images. (b) Evolution of the total erosion rill length L_r between October 2005 and April 2010 44

3.1 Schematic percolation model for a simplified hillslope 50

3.2 Three-dimensional model lattice structure of the percolation model 53

3.3 Percolation thresholds deduced from Π, the ratio between realisations with a percolating cluster and the total number of realisations with occupation probability p. (a) For lattices with 12 neighbours. (b) For the coordination number 8. (c) For the the ‘Chicken Creek lattice’ (connectivity 8) 55

3.4 Determination of the threshold water contents and their allocation to the model cells. (a) Definition of the free water capacity threshold θ_t as the corresponding water content at the inflection point of the water retention curve. (b) Transformation of the random lattice cell numbers to free water capacity thresholds according to the sum curve of the free water capacity threshold values derived from the 316 sample sites. 58

3.5 Modelled drainage pathways showing the concentration [$\mathrm{m}^3\,\mathrm{m}^{-3}$] and total depth d [mm] of drainable water connected to the lake for an increasing occupation probability p (steps of 0.01) starting from $p = 0.50$ and ending with $p = 0.54$ (corresponding to a catchment water content θ between 0.3286 and 0.3301) 60

3.6 Draining clusters for a single realisation at water content 0.3294 ($p = 0.52$) and detailed three-dimensional view of a section showing different clusters connected to the lake 62

3.7 Sum curve of drainable water and fraction of draining cells for an increasing occupation probability or water content, respectively . . 64

4.1 Flow chart of the self-organised critical network (SOCN) model . . 78

4.2 Flow chart of the Manning-based (MB) model 81

4.3 Comparison of (a) the measured erosion rill network, serving as first order estimate for the surface flow paths in the catchment and surface flow paths simulated by (b) the SOCN model and (c) the MB model, respectively 86

4.4 Quantification of simulated surface flow paths (SOCN model and MB model, respectively) and measured erosion rills (MEAS). (a) Total flow path length of a given Strahler order ω normalised by total flow path length. (b) Relationship between the relative flow path length L_p and the relative flow network length L_n 88

4.5 Comparison of (a) the measured rill network with (b) the rill network simulated with the SOCN model, and (c) the rill network simulated with the MB model, respectively 89

4.6 Three-dimensional plots of the rill network (a) derived from the DEM 2008, (b) simulated with the SOCN model and (c) simulated with the MB model 92

4.7 Simulated network evolution starting from an unrilled state. (a) Results of the SOCN model. (b) Results of the MB model 93

4.8 Comparison of the contributing area of the initial, unrilled surface topography and the evolved surface topography after (a) the SOCN model run and (b) the MB model run 95

5.1 Schematic description of the hydrological model for a sub-system including a rill and six selected fcc soil cells 107

5.2 Infiltration rates determined with Philip's equation 114

5.3 Temporal evolution of the surface flow paths defined by tracking every 500^{th} water element 116

5.4 Surface flow paths of every 500^{th} water element displayed at $t = 100\,000\,\mathrm{s}$ for (a) the simulation with the initial surface topography and (b) the developed surface topography including the rill network. The dark blue lines show the contributing area and confirm general flow patterns depicted by the flow simulations of discrete water elements . . . 117
5.5 Cumulated surface runoff for the simulation with the initial surface topography and for the developed topography including the rills and cumulated subsurface outflow for the simulation with the initial topography and for the developed topography . . . 118
5.6 Relation between flow path length and time needed to cover the distance of each water element until it is infiltrating or reaching the outflow. Data are shown for the simulation with the initial surface topography and for the developed topography including the rills . . 120
5.7 Temporal evolution of hydrologically connected clusters in the soil . 121

A.1 Minimum number of realisations needed in order to determine the percolation threshold p_c of each of the three lattice configurations with the full fcc (a) and the modified fcc neighbourhood (b) 151

List of Tables

4.1 Comparison of measured and simulated rill depths at the positions indicated in Figure 10a and 22a (A1 – D4) 90

List of Symbols

Symbol	**Description**	**Dimension**	**Unit**
a	model grid cell area	$[\mathrm{L}^2]$	$[\mathrm{m}^2]$
A	contributing area	$[\mathrm{L}^2]$	$[\mathrm{m}^2]$
A_{crit}	critical contributing area	$[\mathrm{L}^2]$	$[\mathrm{m}^2]$
A_f	catchment area of the footslope	$[\mathrm{L}^2]$	$[\mathrm{m}^2]$
A_s	total catchment area	$[\mathrm{L}^2]$	$[\mathrm{m}^2]$
b	channel width	$[\mathrm{L}]$	$[\mathrm{m}]$
c	fraction of clay	$[-]$	$[-]$
D	diffusivity	$[\mathrm{L}^2\,\mathrm{T}^{-1}]$	$[\mathrm{m}^2\,\mathrm{s}^{-1}]$
d	total depth of drainable water	$[\mathrm{L}]$	$[\mathrm{m}]$
d_d	deposited sediment	$[\mathrm{L}]$	$[\mathrm{m}]$
d_e	erosion parameter	$[\mathrm{L}]$	$[\mathrm{m}]$
d_f	flow depth	$[\mathrm{L}]$	$[\mathrm{m}]$
d_p	sediment particle diameter	$[\mathrm{L}]$	$[\mathrm{m}]$
d_r	rill depth	$[\mathrm{L}]$	$[\mathrm{m}]$
d_s	sink distance of sediment particles	$[\mathrm{L}]$	$[\mathrm{m}]$
e	erosion rate	$[\mathrm{L}\,\mathrm{T}^{-1}]$	$[\mathrm{m}\,\mathrm{s}^{-1}]$
f	reduction factor for K_s at the soil surface	$[-]$	$[-]$
g	gravitational acceleration	$[\mathrm{L}\,\mathrm{T}^{-2}]$	$[\mathrm{m}\,\mathrm{s}^{-2}]$
H	erodibility factor	$[-]$	$[-]$
h	suction pressure	$[\mathrm{L}]$	$[\mathrm{m}]$
h_w	hydraulic head	$[\mathrm{L}]$	$[\mathrm{m}]$

List of Symbols: continued.

Symbol	**Description**	**Dimension**	**Unit**
I	iteration step	$[-]$	$[-]$
i	model grid cell	$[-]$	$[-]$
i_n	neighbour of i in direction of steepest slope	$[-]$	$[-]$
j	index variable	$[-]$	$[-]$
K	hydraulic conductivity	$[\mathrm{L\,T^{-1}}]$	$[\mathrm{m\,s^{-1}}]$
K_s	saturated hydraulic conductivity	$[\mathrm{L\,T^{-1}}]$	$[\mathrm{m\,s^{-1}}]$
k	total number of ECH$_2$0 probes per transect	$[-]$	$[-]$
l	distance between model grid cells	$[\mathrm{L}]$	$[\mathrm{m}]$
L_f	total flow path length on the footslope	$[\mathrm{L}]$	$[\mathrm{m}]$
L_i	individual flow path length between lake and i	$[\mathrm{L}]$	$[\mathrm{m}]$
L_n	relative flow network length	$[\mathrm{L}]$	$[\mathrm{m}]$
L_p	relative flow path length	$[\mathrm{L}]$	$[\mathrm{m}]$
L_r	total erosion rill length	$[\mathrm{L}]$	$[\mathrm{m}]$
m	roughness coefficient	$[-]$	$[-]$
n	pore size index	$[-]$	$[-]$
N	number of flow paths	$[-]$	$[-]$
P	precipitation	$[\mathrm{L\,T^{-1}}]$	$[\mathrm{m\,s^{-1}}]$
p	occupation probability	$[-]$	$[-]$
p_c	percolation threshold	$[-]$	$[-]$
Q_m	mean annual surface runoff	$[\mathrm{L^3}]$	$[\mathrm{m^3}]$
Q_{soil}	subsurface runoff	$[\mathrm{L^3\,T^{-1}}]$	$[\mathrm{m^3\,s^{-1}}]$
Q_{sed}	volumetric sediment discharge	$[\mathrm{L^3\,T^{-1}}]$	$[\mathrm{m^3\,s^{-1}}]$
Q_{surf}	surface runoff	$[\mathrm{L^3\,T^{-1}}]$	$[\mathrm{m^3\,s^{-1}}]$
Q_{tot}	total runoff from the catchment	$[\mathrm{L^3}]$	$[\mathrm{m^3}]$
Q_{weir}	subsurface runoff through the weir in the clay wall	$[\mathrm{L^3\,T^{-1}}]$	$[\mathrm{m^3\,s^{-1}}]$
q_{sed}	volumetric sediment discharge per unit channel width	$[\mathrm{L^2\,T^{-1}}]$	$[\mathrm{m^2\,s^{-1}}]$

List of Symbols: continued.

Symbol	**Description**	**Dimension**	**Unit**
r	sediment particle radius	$[\mathrm{L}]$	$[\mathrm{m}]$
R	random number between 0.0 and 1.0	$[-]$	$[-]$
S	sorptivity	$[\mathrm{L\,T^{-1/2}}]$	$[\mathrm{m\,s^{-1/2}}]$
s	length of grid cell	$[\mathrm{L}]$	$[\mathrm{m}]$
s_{oct}	side length of octagon with area a	$[\mathrm{L}]$	$[\mathrm{m}]$
s_{vf}	fraction of very fine sand	$[-]$	$[-]$
t	time or time step	$[\mathrm{T}]$	$[\mathrm{s}]$
t_{crit}	critical time step for runoff	$[\mathrm{T}]$	$[\mathrm{s}]$
t_{surf}	time step for surface runoff	$[\mathrm{T}]$	$[\mathrm{s}]$
t_{soil}	time step for subsurface runoff	$[\mathrm{T}]$	$[\mathrm{s}]$
t_p	starting time of surface water ponding	$[\mathrm{T}]$	$[\mathrm{s}]$
t_c	corrected starting time of surface water ponding	$[\mathrm{T}]$	$[\mathrm{s}]$
T	number of days with rainfall	$[-]$	$[-]$
u_1, u_2, u_3	empirically derived parameters	$[\mathrm{M\,L^{-1}\,T^{-2}}]$	$[\mathrm{kg\,m^{-1}\,s^{-2}}]$
V	volume of surface runoff	$[\mathrm{L^3}]$	$[\mathrm{m^3}]$
V_d	total volume of subsurface runoff	$[\mathrm{L^3}]$	$[\mathrm{m^3}]$
V_i	volume of a fcc cell	$[\mathrm{L^3}]$	$[\mathrm{m^3}]$
V_w	volume of drainable water from a fcc cell	$[\mathrm{L^3}]$	$[\mathrm{m^3}]$
v	water flow velocity	$[\mathrm{L\,T^{-1}}]$	$[\mathrm{m\,s^{-1}}]$
v_s	sediment sink velocity	$[\mathrm{L\,T^{-1}}]$	$[\mathrm{m\,s^{-1}}]$
x	first horizontal model grid coordinate	$[-]$	$[-]$
y	second horizontal model grid coordinate	$[-]$	$[-]$
Z	coordination number	$[-]$	$[-]$
z	vertical model grid coordinate	$[-]$	$[-]$
α	inverse of a characteristic pressure head	$[\mathrm{L^{-1}}]$	$[\mathrm{m^{-1}}]$
$\Delta\theta$	soil moisture difference index	$[-]$	$[-]$
Δz	depth between model grid cells in a soil column	$[\mathrm{L}]$	$[\mathrm{m}]$

List of Symbols: continued.

Symbol	Description	Dimension	Unit
χ	dimension conversion factor	$\left[\mathrm{L}^{1/3}\,\mathrm{T}^{-1}\right]$	$\left[\mathrm{m}^{1/3}\,\mathrm{s}^{-1}\right]$
δ_f	surface flow path density on the footslope	$\left[\mathrm{L}^{-1}\right]$	$\left[\mathrm{m}^{-1}\right]$
ε	coefficient of proportionality	$\left[\mathrm{M}\,\mathrm{L}^{-3}\,\mathrm{T}^{-2}\right]$	$\left[\mathrm{kg}\,\mathrm{m}^{-3}\,\mathrm{s}^{-2}\right]$
η	fluid viscosity	$\left[\mathrm{M}\,\mathrm{L}^{-1}\,\mathrm{T}^{-1}\right]$	$\left[\mathrm{kg}\,\mathrm{m}^{-1}\,\mathrm{s}^{-1}\right]$
φ	infiltration rate	$\left[\mathrm{L}\,\mathrm{T}^{-1}\right]$	$\left[\mathrm{m}\,\mathrm{s}^{-1}\right]$
Θ	effective water saturation	$[-]$	$[-]$
θ	volumetric water content	$[-]$	$[-]$
θ_0	initial volumetric water content	$[-]$	$[-]$
θ_r	residual water content	$[-]$	$[-]$
θ_s	saturated water content	$[-]$	$[-]$
θ_t	free water capacity threshold	$[-]$	$[-]$
Π	percolation probability	$[-]$	$[-]$
ρ_f	fluid density	$\left[\mathrm{M}\,\mathrm{L}^{-3}\right]$	$\left[\mathrm{kg}\,\mathrm{m}^{-3}\right]$
ρ_s	soil density	$\left[\mathrm{M}\,\mathrm{L}^{-3}\right]$	$\left[\mathrm{kg}\,\mathrm{m}^{-3}\right]$
σ	steepest slope between i and its neighbours	$[-]$	$[-]$
σ_w	water surface slope	$[-]$	$[-]$
τ	shear stress	$\left[\mathrm{M}\,\mathrm{L}^{-1}\,\mathrm{T}^{-2}\right]$	$\left[\mathrm{kg}\,\mathrm{m}^{-1}\,\mathrm{s}^{-2}\right]$
τ_{cd}	critical shear stress for deposition	$\left[\mathrm{M}\,\mathrm{L}^{-1}\,\mathrm{T}^{-2}\right]$	$\left[\mathrm{kg}\,\mathrm{m}^{-1}\,\mathrm{s}^{-2}\right]$
τ_{ce}	critical shear stress for erosion	$\left[\mathrm{M}\,\mathrm{L}^{-1}\,\mathrm{T}^{-2}\right]$	$\left[\mathrm{kg}\,\mathrm{m}^{-1}\,\mathrm{s}^{-2}\right]$
τ^*	Shields number	$[-]$	$[-]$
τ^*_{ce}	dimensionless critical shear stress for erosion	$[-]$	$[-]$
Φ	porosity	$[-]$	$[-]$
Φ^*	dimensionless bedload transport	$[-]$	$[-]$
ω	Strahler order	$[-]$	$[-]$
Ω	set of cells belonging to a drainage cluster	$[-]$	$[-]$

1 Introduction

1.1 Background

To predict the response of natural terrestrial ecosystems to anthropogenic and natural disturbances such as climate change or land use, it is essential to understand the governing hydrological processes and their interactions with biosphere and element fluxes (e.g. Arnell, 2002; Bates et al., 2008; Li et al., 2009). For ecological studies at the landscape scale (e.g. Gburek and Folmar, 1999; Lemonds and McCray, 2007) hydrological catchments are usually chosen as observation units, since they describe clearly defined budget areas for water and elements. However, information on the complex multi-scale inner structure of a catchment (e.g. soil type or bedrock topography) is difficult to retrieve (Kendall et al., 2001; Sivapalan et al., 2003) and corresponding data collection is laborious and cost expensive. Due to the unknown catchment architecture and the manifold of interacting processes, the prediction of the hydrologic response of a catchment to changing boundary conditions remains an unsolved task.

Most large-scale ecosystem research was conducted in mature catchments characterised by a dynamic equilibrium and highly evolved complex structures and processes that limit the possibility to recognise structures and processes driving the evolution of a catchment. As alternative to studies on complex developed ecosystems, analyses of ecosystems in their initial state can help to reveal processes governing the functioning and evolution of ecosystems. The initial phase is crucial as the early evolution of processes and structures directs the further development of the system. In addition to studying hydrological processes during the initial phase of naturally developed ecosystems (e.g. after the retreat of glaciers or after landslides), a few catchments were artificially created, e.g. the Hydrohill catchment in China described in Kendall et al. (2001) or the El Moral slopes in Spain presented in Nicolau (2002). A major advantage of such man-made catchments is that boundaries and inner structures can be defined in advance and that heterogeneities (e.g. of the bedrock or of the soil material) can be reduced. As soon as the construction of a man-made catchment is complete, it can be considered to be at 'point zero' in time, a development stage rarely found in nature. In addition, a man-made ecosystem in its initial development stage is much less complex than mature natural catchments. There are, for example, only a very limited number of organisms, like abundant microorganisms, but no higher plants and animals present at this stage. The reduction in complexity of structure and interaction due to the absence of most biological agents considerably eases the investigation and quantification of hydrological processes and fluxes.

To delineate hydrological processes affecting the development of terrestrial ecosystems, the man made 'Chicken Creek' catchment (6 ha) near Cottbus (Germany) was established in 2005. The catchment represents an entire ecosystem at full landscape scale (Chapter 2). It combines the advantage of well-known inner structures and system boundaries with the opportunity of observing the initial phase of ecosystem development starting from point zero.

1.2 Contents and focus of the thesis

The focus of the present thesis lies on the model-based investigation of hydrologically relevant structures and processes of the initial development phase of the man-made catchment Chicken Creek. The key questions addressed in this thesis are:

- What are characteristic hydrological processes of the initial phase?
- Which types of structures control the hydrological processes of the initial phase?
- How do hydrological structures and processes evolve during the initial phase?

- What are the effects of evolving structures on water fluxes?

Chapter 2: The catchment Chicken Creek is introduced with a comprehensive description of the field site including hydrological measurements and properties. In the following three chapters different modelling concepts to simulate hydrologically relevant structures and their impact on water flow paths in the catchment are presented.

Chapter 3: Based on measured wetness patterns and runoff and rainfall data the existence of fast subsurface drainage pathways is postulated. The observation that runoff is triggered only for rainfall above a well-defined threshold indicates that preferential flow paths with high water flow velocities exist that connect only for rainfall above the threshold. Further analyses revealed that subsurface flow paths developed in areas, where they were not expected according to the initial conceptual model of subsurface water flow. Chapter 3 examines how material properties and geometrical hillslope structures determine subsurface drainage pathways and how the connectivity of these pathways affects catchment runoff. The following specific questions are addressed:

- What are the factors controlling the establishment of a network of subsurface flow paths?
- Where do subsurface drainage pathways evolve in the catchment?
- How does subsurface flow path connectivity relate to the observed rainfall threshold for catchment runoff?

To represent the preferential subsurface flow paths and the nonlinear catchment runoff response to rainfall, a new model focussing on subsurface water flows was developed based on Percolation Theory. For this purpose the three-dimensional geometry of the catchment is subdivided into cells that may be in a conductive or non-conductive state and control the connectivity of subsurface drainage flow paths.

Chapter 4: Preferential flow through subsurface drainage pathways is not the only mechanism transporting water quickly to the catchment outlet. The extensive erosion rill network on the catchment surface indicates that surface runoff is also an important hydrological process of the initial development phase of the Chicken Creek catchment. Erosion rills affect water flow by channelling surface runoff, by locally changing the infiltration capacity of the soil, by altering hydraulic gradients, or by preventing the establishment of a vegetation cover. Therefore, the hydrologic response of the catchment cannot be understood based on flow models that neglect the time-dependent surface structures and pathways. To successfully model the hydrology of a young developing slope system it is indispensable to simulate the generation of the erosion rills adequately. In Chapter 4 two model approaches that simulate the dynamics of rill growth and predict the spatial location of evolving rills were modified and tested. First, we used a self-organised critical network approach (Rinaldo et al., 1993) with soil erosion and sediment deposition governed by a local critical shear stress. The second approach is a surface runoff model based on Manning's equation. Soil erosion was activated in the case of high local shear stress and deposition of the entrained sediment load was determined as a function of sedimentation velocity. The models were validated against observed rill patterns from the Chicken Creek catchment. The following questions are addressed in Chapter 4:

- Are the models able to predict the location of evolving surface erosion rills in the Chicken Creek catchment?
- What are the factors controlling the development of surface rills in a new developing ecosystem?
- Does the rill network extension converge to a steady state?
- How do the surface flow paths change with developing erosion rills?

Chapter 5: The hydrology of the Chicken Creek catchment is governed by nonlinear processes and the development of hydrologically relevant structures at the catchment scale. Current hydrological models often can represent neither such nonlinear behaviour nor the evolution of macro-scale patterns. The goal of Chapter 5 is to tackle these model drawbacks by conceptualising a new hydrological model, which is capable to reproduce nonlinear runoff processes, the transit times of water, and the emergence and effect of hydrologically relevant structures at the macro-scale within a single model framework.

Results obtained in Chapter 3 and Chapter 4 are integrated in the new model. On the one hand, model concepts of the presented Percolation Theory model were used in combination with traditional physically-based water flow equations. On the other hand, the erosion rill structures derived from model simulations are incorporated in the new model to assess the effect of the rills on water flows in the catchment. The focus of Chapter 5 lies on testing the feasibility of the new model concept rather than on simulating runoff components as precise as possible compared to measurements. The following questions were addressed:

- How do hydrological surface and subsurface flow paths connect in space and time?
- What are characteristic flow distances, times and velocities of surface water and how do they change in the presence of surface erosion rills?
- What effect do the erosion rills have on total surface water outflow?

Although the model at the current state was tested under simplified initial conditions and processes, the practicability of the model could be demonstrated by first encouraging simulation results.

Chapter 6: The thesis concludes with a short overview on necessary research to improve the predictability of dynamic hydrological processes and evolving structures in catchments. In the light of current issues in hydrological catchment modelling a few suggestions for the successful realisation and further development of the model concept presented in Chapter 5 are provided and discussed.

1.3 Model aspects

The different models developed in the framework of this thesis (Chapters 3, 4 and 5) describe structures and processes at a small spatial scale (one metre resolution or less). The basic design of all models is a two- or three-dimensional

Cartesian grid. To reconstruct the relevant structure heterogeneities and to reasonably reproduce the considered processes, a grid resolution of 0.25 – 1.0 m and a high coordination number (eight to twelve adjacent neighbours per cell depending on the dimensionality of the model) was chosen. Consequently, all the models consist of a large number of grid nodes (up to nearly 4 000 000). As each node enquires information from all of its neighbours a multitude of operations have to be calculated per single simulation iteration step. Thus, optimised algorithms are necessary to minimise computational resources.

2 Experimental site

2.1 Location

The man-made catchment Chicken Creek is located in the post-mining landscape of the opencast lignite mine Welzow-South, 150 km south from Berlin (Germany). The research site was planned and realised under supervision of the Brandenburg University of Technology in Cottbus and the mining company Vattenfall Europe Mining AG. The catchment serves as study site for the German Transregional Collaborative Research Centre (SFB/TRR 38) which is funded by the Deutsche Forschungsgemeinschaft (DFG). After completion in late 2005 the catchment was left to an undirected and undisturbed development (Kendzia et al., 2008).

2.2 Catchment design

The Chicken Creek catchment was designed as hillslope with the extension of about 450 m in northwest and 140 m in north–northeast direction resulting in a catchment area of approximately 6 ha (Figure 2.1a). The catchment has an elevation difference of 15 m and an average longitudinal inclination of 3.2 %. The catchment is comprised of three major sections (Gerwin et al., 2009a): the backslope with low inclination (2.7 % in average), the footslope with a steeper inclination (5.4 % in average), and the lake basin. During the first year the basin was filled gradually by catchment runoff and direct precipitation input and evolved to a small lake with a surface of $3600\,\mathrm{m}^2$ and an average depth of 1 m. The backslope of the catchment is gently v-shaped with an eastern and a western side facing together

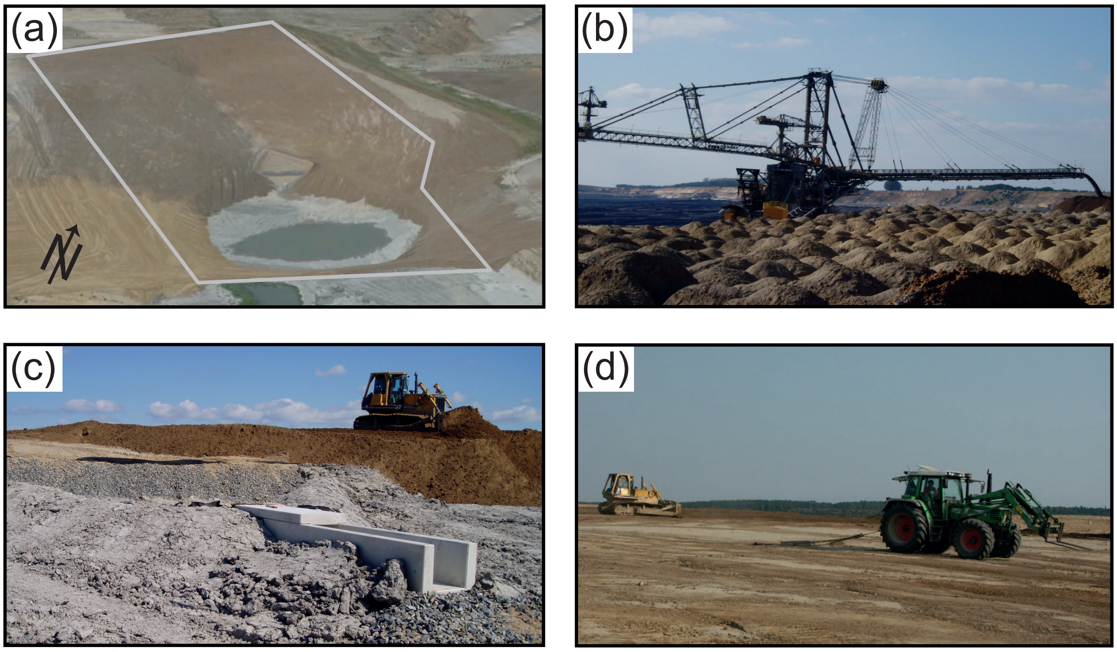

Figure 2.1: Construction of the field site Chicken Creek. (a) Overview of the Chicken Creek catchment (encompassed by grey lines) after completing the construction work in September 2005. (b – d) Different steps during construction with (b) stacker dumping the base layer (September 2004), (c) impermeable clay layer (grey) below sand body (brown) with concrete weir to catch subsurface flow in the middle of the picture (July 2005), and (d) flattening of the surface by tractors dragging rails in order to remove caterpillar tracks (September 2005).

with an inclination of 0.3 – 2.1 % (Schneider et al., 2011) causing surface runoff to concentrate at the centre line. The inner structure of the catchment comprises a general base layer on top of which a clay layer of 2 – 3 m thickness was dumped by means of mining technology (Figure 2.1b). The same clay material was used before in another reclaimed area and has proven to be an optimal vertical barrier to seepage water (Gerwin et al., 2009a). The clay layer was designed in a tub shape to ensure a closed system to water flows. The actual soil body of the catchment, acting as aquifer, is composed of Quaternary sand, which was dumped by stackers on top of the clay layer (Figure 2.1c). The soil surface was levelled by caterpillars and tracks were removed by final flattening at the end of the construction works (Gerwin et al., 2009b) (Figure 2.1d). Figure 2.2 shows the digital elevation models (DEM) of the initial catchment surface and of the clay layer. The DEM of the

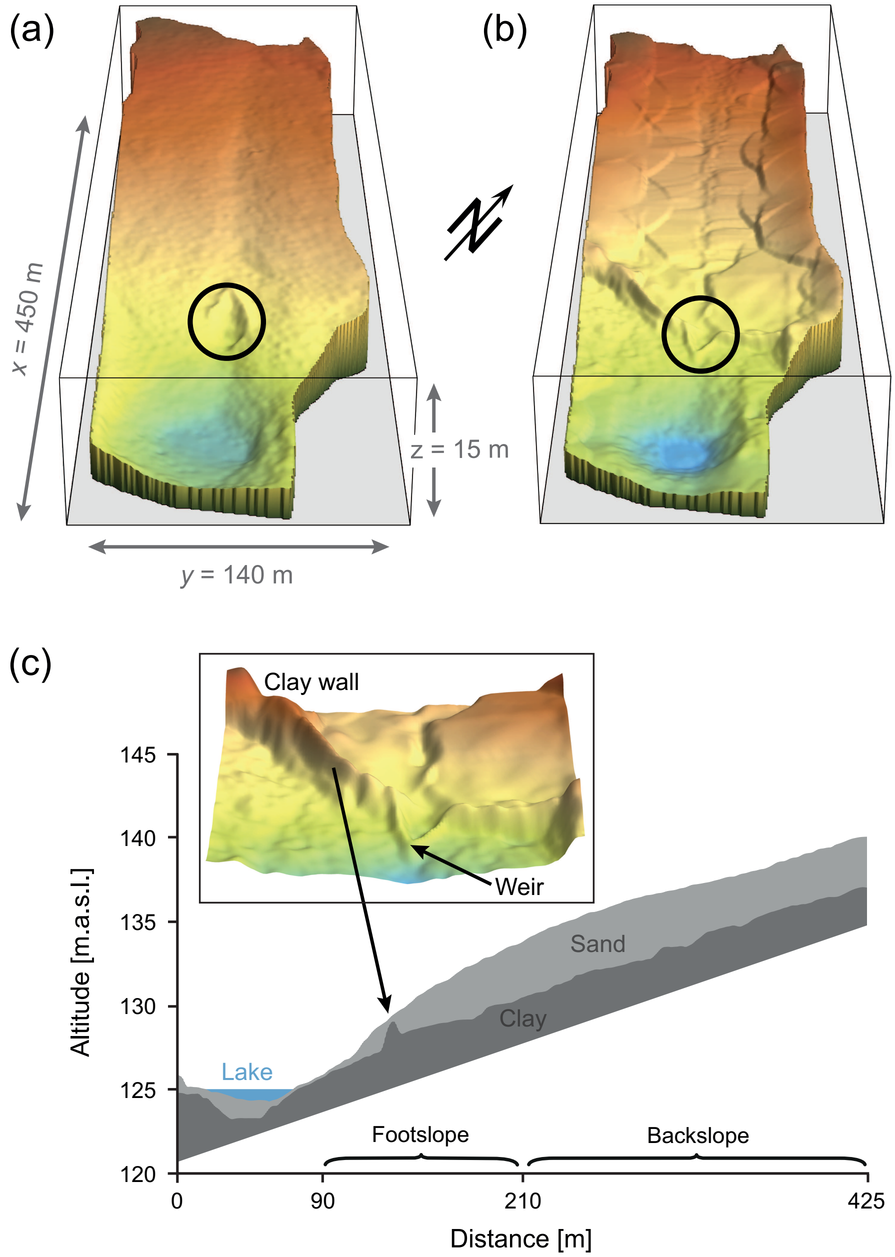

Figure 2.2: Overview of the catchment geometry. Digital elevation model (DEM) of (a) the catchment surface and (b) the clay layer (vertical exaggeration 17×). The structure in the lower middle of the catchment (indicated by the circles) is the weir facility (described at the end of Section 2.2). The surface is exposed to water and wind erosion and its initial state is shown in (a). The structures in the clay layer are caused by the filling procedure. (c) Longitudinal cross-section through the catchment highlighting the clay wall planned to collect surface water from the upper part of the catchment. The inset shows a three-dimensional view of the clay wall (vertical exaggeration 5×).

surface was produced by means of automated digital photogrammetry based on aerial images taken in November 2005 (courtesy of Vattenfall Europe Mining AG, Cottbus) and improved by filtering out systematic errors and artefacts (Schneider et al., 2011). The clay layer DEM was realised according to aerial pictures and interpolation between drilling measurements (Gerwin et al., 2009b). Soil depth in the catchment varies between 0 and 4 m, the average soil depth is 2 m (Figure 2.2c). Shallow soil depths are generally observed in the topographically lower area of the catchment near the lake, whereas larger soil depths are found on the backslope of the catchment. A special feature and dominant structure of the catchment is the clay layer elevation separating the lower third of the catchment from the upper part. The clay elevation has the form of a wall of about 1 m height and extends along the entire width of the catchment, reducing soil depths locally (Figures 2.2b and 2.2c). The construction of the clay wall was done for two reasons: First, it assures the stability of the sandy soil layer upslope of the wall, and second, it was designed as a barrier to capture the subsurface flow along the clay layer at the weir located in the middle of the clay wall (Figure 2.1c and Figure 2.2c).

2.3 Soil properties

2.3.1 Soil texture

Soil texture was measured for 316 samples taken from soil core probes at the intersection points of a 20 m × 20 m raster spanning the research site. The samples were taken from depth intervals: 0 – 30 cm (124 samples), 30 – 100 cm (121 samples), 100 – 150 cm (29 samples), 150 – 200 cm (26 samples) and $>$ 200 cm (16 samples) (Gerwin et al., 2009b). According to the soil texture triangle of the United States Department of Agriculture (USDA) the samples can be classified as sand, loamy sand or sandy loam (Figure 2.3). The mean composition of the soil consists of 83 % sand of which 13 % were classified as coarse sand (0.63 – 2 mm), 44 % as middle-sized sand (0.2 – 0.63 mm), and 26 % as fine sand (0.063 – 0.2 mm). The average clay and silt fractions account for 7 and 10 %, respectively (Gerwin et al., 2009b).

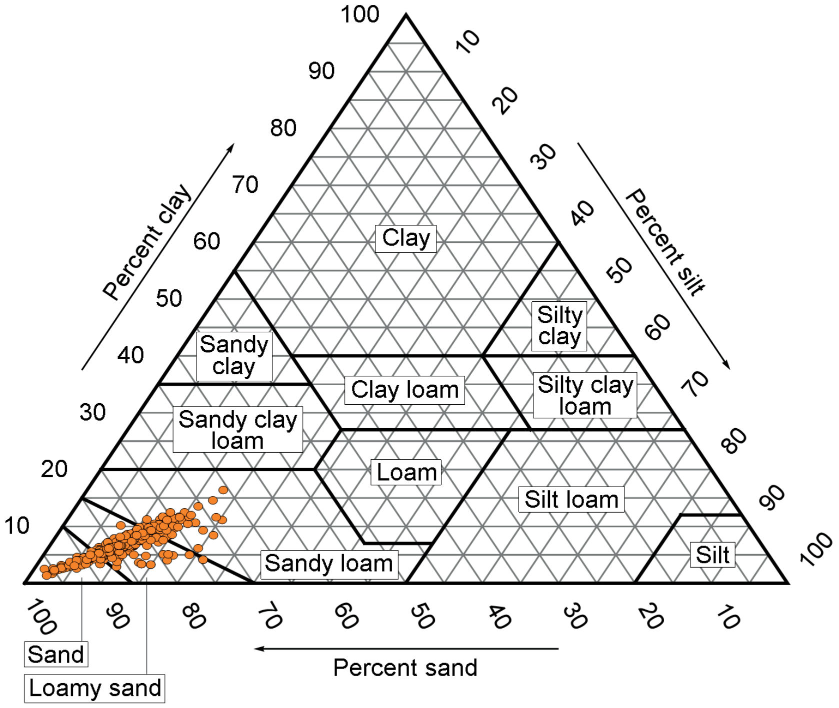

Figure 2.3: Location of the soil texture samples in the soil texture triangle of the United States Department of Agriculture. The high sand contents indicate high water conductivity for high water saturations and abruptly decreasing conductivity for partially saturated samples.

2.3.2 Soil hydraulic properties

The hydraulic properties (hydraulic conductivity and capillary pressure as function of soil water content) of the soil texture samples were parameterised according to the van Genuchten model (van Genuchten, 1980). The required parameters were deduced from texture measurements using a pedotransfer function (Rosetta model; Schaap et al., 2001). Pedotransfer functions are relationships between soil hydraulic parameters and the easier measurable properties usually available from soil survey (Pachepsky et al., 2006). The relationship between the computed van Genuchten parameters is displayed in Figure 2.4. While the saturated hydraulic conductivity K_s is highly correlated with the pore size width n, the parameter α (inverse of characteristic capillary pressure head) has no well-defined effect on K_s. The hydraulic material functions of the most and the least sandy texture

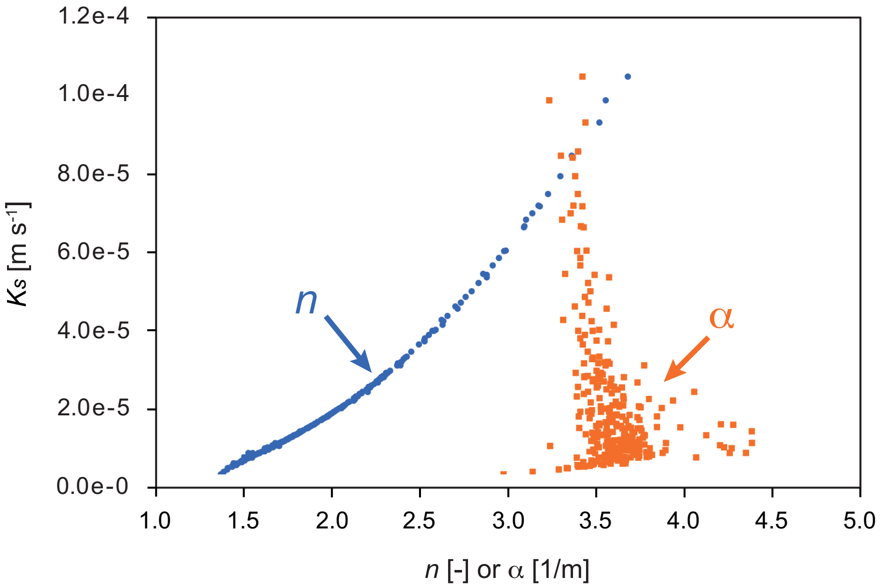

Figure 2.4: Relation between the saturated hydraulic conductivity K_s and the two van Genuchten parameters α and n determined by the Rosetta model for all the 316 soil texture samples. In contrast to the parameter α, n is highly correlated with K_s.

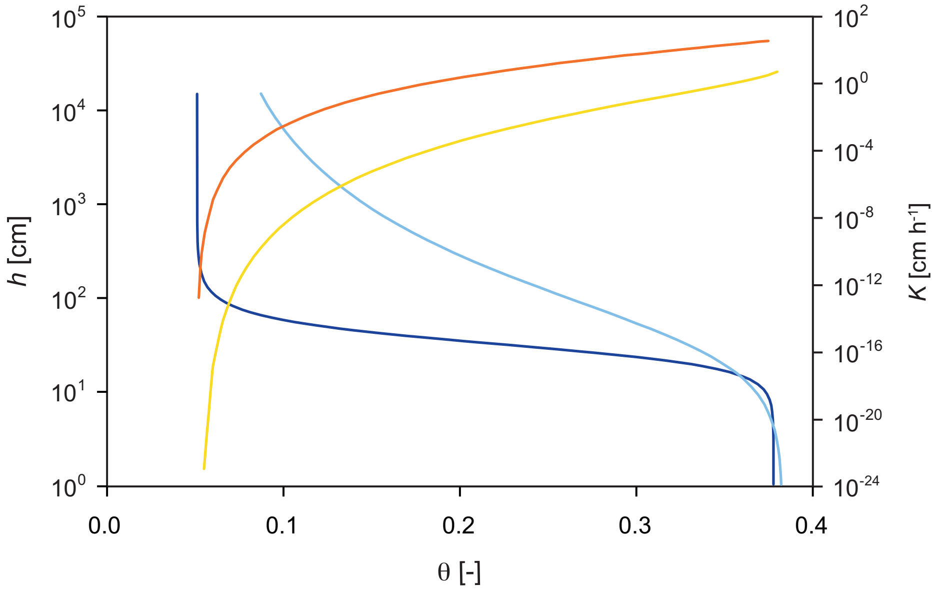

Figure 2.5: Soil hydraulic properties deduced from soil texture using transfer functions for the sample with the highest (96 %) and the lowest sand fraction (66 %), respectively. The soil water characteristics are given in blue tones (dark blue for maximum sand fraction) and hydraulic conductivity in red tones (orange for minimum sand fraction).

sample are shown in Figure 2.5 in order to approximate the range of hydraulic properties in the catchment. Volumetric water content at saturation is around 0.38 with saturated hydraulic conductivities deduced from pedotransfer functions ranging from 4 to 340 mm h^{-1}. These K_s values are in agreement with independent infiltrometer measurements at different locations in the catchment (K_s from 9 to 99 mm h^{-1}) (Gerwin et al., 2009b).

2.4 Hydrological characteristics of the Chicken Creek catchment

2.4.1 Rainfall threshold for catchment runoff

A basic hydrologic property of catchments is the relationship between rainfall amount and catchment outflow (surface and subsurface). To determine this relationship for the period between February 2007 and August 2009 we used precipitation data measured every 10 minutes with a meteo station located in the middle of the catchment and lake level fluctuation values recorded every 10 minutes using two pressure transducers. Catchment outflow was estimated by the increase in lake volume (corrected for rainfall into the lake) and outflow from the lake. Since catchment runoff started in general during the rainfall with conditions of very low evaporation rate, evaporation from the lake surface was neglected. To determine water fluxes during rainfall events, the time series was split into different events according to the constraint that no precipitation occurs between two events for a certain duration (as discussed below we tested time gaps between 1 and 8 days to separate two events). The entire cumulated outflow before the onset of a new rainfall was assigned to a precipitation event. Because it is unknown how long water needs to flow through the catchment into the lake, it is not straightforward to define the waiting time without rainfall before a new rainfall event begins. Therefore, we tested various waiting times to classify rainfall events and we found that a rainfall threshold of 9 mm must be exceeded before catchment runoff occurred, independent of the waiting time used to define rainfall events. In Figure 2.6a the relationship between cumulated precipitation ($\sum P$)

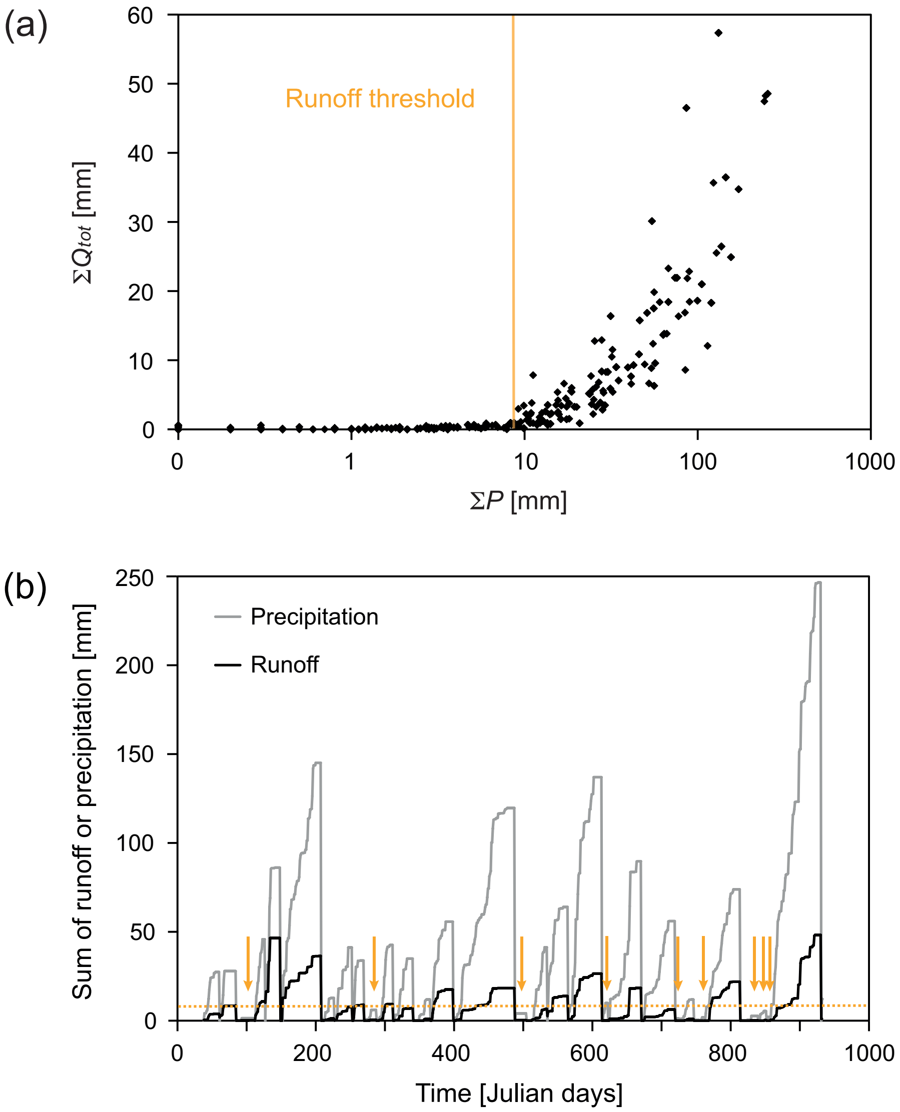

Figure 2.6: Rainfall threshold to trigger catchment runoff for the period between the 21st of February 2007 (day 52) and the 4th of August 2009 (day 947). (a) The relationship between cumulated precipitation ($\sum P$) and cumulated total catchment runoff ($\sum Q_{tot}$) is shown for each precipitation event. A precipitation event was separated by a time span of several days without rainfall. For each time span value ranging from 1 to 8 days precipitation events were classified and resulting rainfall and runoff data are presented in the same figure. Independent of the value of the time span to separate between two rainfall events, a rainfall threshold of 9 mm must be exceeded to produce runoff. (b) The sum curves for precipitation and catchment runoff are displayed for events separated by dry period of four days or more. The dashed line marks the threshold of minimum rainfall amount required to create catchment runoff (9 mm). The arrows denote precipitation events where no (negligible) runoff is produced.

and cumulated total catchment runoff ($\sum Q_{tot}$) for all precipitation events with waiting times between 1 and 8 days are shown. It can be seen that Q_{tot} is induced only for precipitation events with a total precipitation rate P larger than 9 mm. For a waiting period of four days Figure 2.6b shows the cumulated precipitation and catchment runoff. The runoff coefficients (ratios between rainfall and outflow volume) for precipitation events above the precipitation threshold ($\sum P > 9\,\text{mm}$) are in the range of 0.02 – 0.7 (mean = 0.21, median = 0.21).

2.4.2 Subsurface flow across the clay wall

The man-made catchment was constructed according to the following conceptual model of water flow: First, water percolates vertically down to the groundwater table. From there it flows laterally along the slope of the clay layer and finally through the weir in the clay wall. However, several observations and data suggest that this conceptual model must be modified because subsurface flow is not entirely captured at the weir as expected, but also takes place across the orographic left hand side of the clay wall. Figure 2.7 presents the section of an aerial picture showing the location of the clay wall. We believe that the distinct moist structure downslope the clay wall, following an east–west alignment, is the result of subsurface water flowing across the clay wall and re-entering the surface layer of the soil. It is unlikely that the moisture originates from the large erosion rill nearby, since there is no slope gradient in east–west direction for water to flow along. Visual inspection during summer also shows vegetation to be denser in the region of the structure, indicating better moisture conditions for plants to grow. Subsurface flow through the weir at the clay wall (Q_{weir}) was measured every 10 minutes with a tipping bucket. The gauged values ranging from 0.27 to $8.6\,\text{l}\,\text{min}^{-1}$ (average of $0.9\,\text{l}\,\text{min}^{-1}$) follow the precipitation dynamics (Figure 2.8). The generally small values of Q_{weir} can be explained on the one hand by the considerable fraction of surface runoff occurring at this stage of the catchment development. On the other hand, the low values also indicate that subsurface water may flow lakewards besides the weir. Additionally, there were a few technical problems with the measuring instrument (e.g. inhibition of flow caused by eroded material and freezing

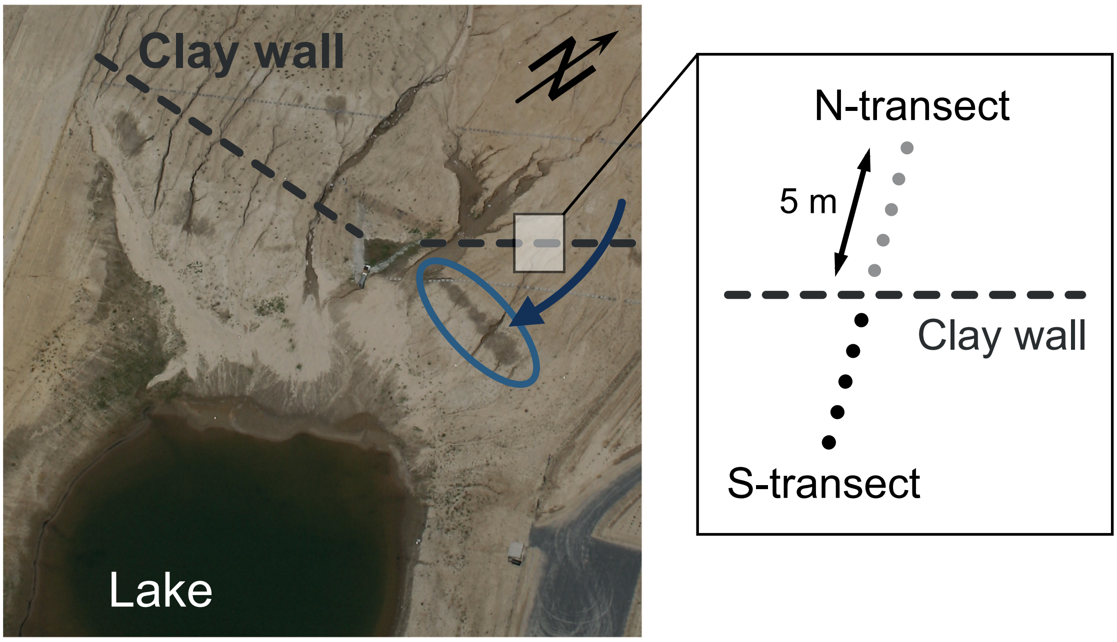

Figure 2.7: Aerial picture showing the location of the clay wall (dashed line) and the surface moisture pattern as indicator for flow across the clay wall (encircled). The dark-toned (moist) features crossing the clay wall in north–south direction are erosion rills. The square locates the position of the water content sensors (dots) that were installed to monitor water flow across the wall.

during wintertime), so that the absolute values of Q_{weir} have to be interpreted carefully.

To attain more information on subsurface flow, especially in the vicinity of the clay wall, the moisture conditions near the observed wet soil pattern described above were measured with ten water content sensors (ECH$_2$O probes, Decagon Devices, Inc., Pullman, USA) buried in 0.1 m soil depth. The ECH$_2$O instruments measure the dielectric constant of the substrate (every 5 minutes in our case) and convert it to volumetric water content according to a calibration curve. The probes were arranged in flow direction along a transect, where water is expected to flow across the clay wall and cause the moisture pattern at the soil surface. The transect was further divided into two subtransects with 5 probes each, separated by the clay wall in the underground. The subtransect northwards from the clay wall is named N-transect, whereas the subtransect located southwards (downslope) is termed S-transect (Figure 2.7). The spacing between the probes is 1 m. We expect

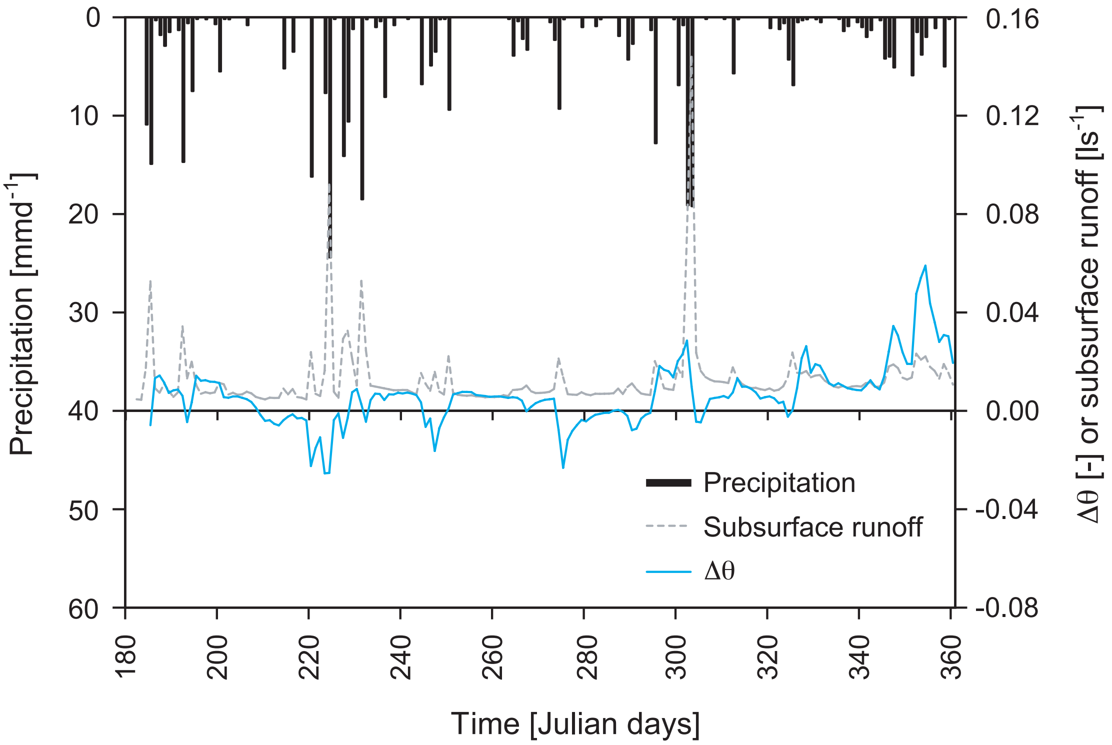

Figure 2.8: Precipitation, subsurface runoff measured at the weir in the clay wall and soil moisture difference index, $\Delta\theta$, between the 4th of July 2008 (day 185) and the 26th of December 2008 (day 360). The soil moisture difference index quantifies the water content difference between the northern part (upslope of wall) and the southern part in downslope direction. Negative values occurring in course of heavy rainfall events indicate water flow across the wall. Occasionally, negative index values are related to outflow from the weir, which is a result of water collection behind the clay wall.

that before water can cross the clay wall, it is collected behind the wall resulting in higher water contents than downslope until water is spilled across the wall increasing water content in downslope direction. To indicate the water flow over the clay wall, we introduced a soil moisture difference index $\Delta\theta$ defined as

$$\Delta\theta = \frac{1}{k}\left(\sum_{j=1}^{k}\theta_{N,j} - \sum_{j=1}^{k}\theta_{S,j}\right) \tag{2.1}$$

where θ is volumetric water content, subscripts N and S denote N-transect and S-transect, respectively, and j stands for the probe number (with $k = 5$ probes). Thus, a positive value of $\Delta\theta$ indicates collection of water in the N-transect while negative values corresponds to higher water content in the southern part because of water crossing the clay wall. Figure 2.8 shows the moisture difference index for the time period between the 4th of July 2008 and the 26th of December 2008. It can be seen that soil conditions on the southern transect become wetter (negative $\Delta\theta$) for large precipitation events, which points to the occurrence of water flow across the clay wall as soon as a certain amount of rainfall is reached. The comparison between the soil moisture difference index and the runoff data at the clay wall weir shows a good agreement in that runoff peaks are often correlated with moister soil conditions on the S-transect. This is a clear evidence of flow over the clay wall for wet conditions.

2.4.3 Surface erosion structures

Surface runoff led to the formation of a gully network immediately after completion of the catchment (Figure 2.9). In the first year of ecosystem development the groundwater table of the catchment was located one to two metres below the soil surface (Mazur et al., 2011). Therefore, the influence of exfiltrating groundwater on the rill development was negligible and rill erosion must have been controlled by limited infiltration. The relatively low measured saturated hydraulic conductivities at the soil surface and the initially completely missing vegetation cover support this assumption. To investigate the evolution of the catchment surface in time, microdrone- and helicopter-borne aerial images were taken once per year between September 2005 and April 2010. The assessment of erosion rills by remote sensing techniques has proven to be a successful method to determine the geometry of erosion rills (Bobrovitskaya and Vorozhbitov, 1979; Hancock et al., 2008; Waythomas et al., 2010), their dynamics (Daba et al., 2003) and the volume of eroded soil on a slope (Watson and Evans, 1991). From the aerial images, we visually digitised the backbone of the rill network of the different years (Figure 2.10a). The main rill network connecting the slope with the lake area established already during the first year (between October 2005 and September 2006). A major rill formed in the middle of the catchment, running around the weir facility at the lower end of the slope, and spanning the entire area in northwest–southeast direction.

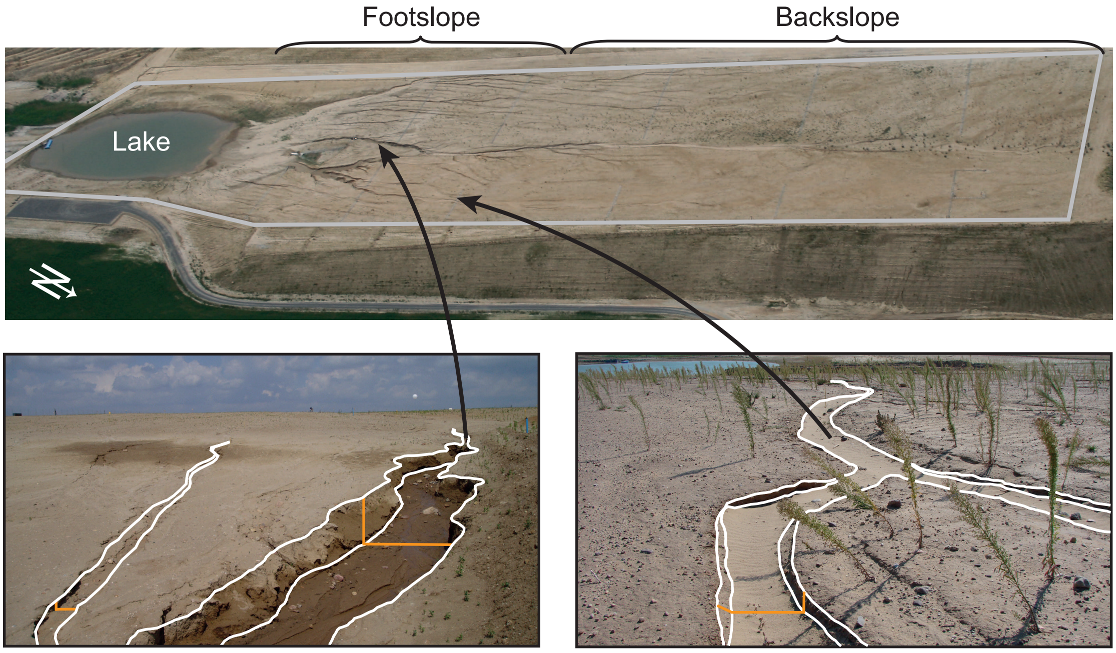

Figure 2.9: Overview of the man-made catchment Chicken Creek (aerial image from June 2007) with grey lines marking the boundary of the field site. Note the erosion rills visible at the footslope. Insets: Erosion rills developed in the catchment (left image taken in June 2006, right image taken in September 2006) with white and orange lines emphasising contour and depth of the rills. The large rill in the left image is about 0.5 m deep, whereas the depth of the rill in the right image is only a few centimeters.

The network density was high on the footslope, and, apart from the main middle rill, negligible on the backslope. The second year (September 2006 – June 2007) was characterised by elongation and further branching of the existing erosion rills, but no new major rills reaching down to the lake were formed. In the following years (July 2007 – April 2010) only minor rill expansions and short new tributaries were detected and the rill network approached a steady state. Figure 2.10b quantifies the network evolution over the years and reveals that 63 % of the maximum rill network (the network in 2010) formed in the first year, 25 % in the second year, 8 % in the third year, and 3 % and 1 % in the fourth and the fifth year, respectively. Additionally to the initial state of the catchment surface (Figure 2.2a), the developed state in 2008 was also reproduced by a DEM (Section 4.3.2). Both of the DEMs have a spatial resolution of 1 m.

Rill depth measurements taken in September 2008 are available for four trans-

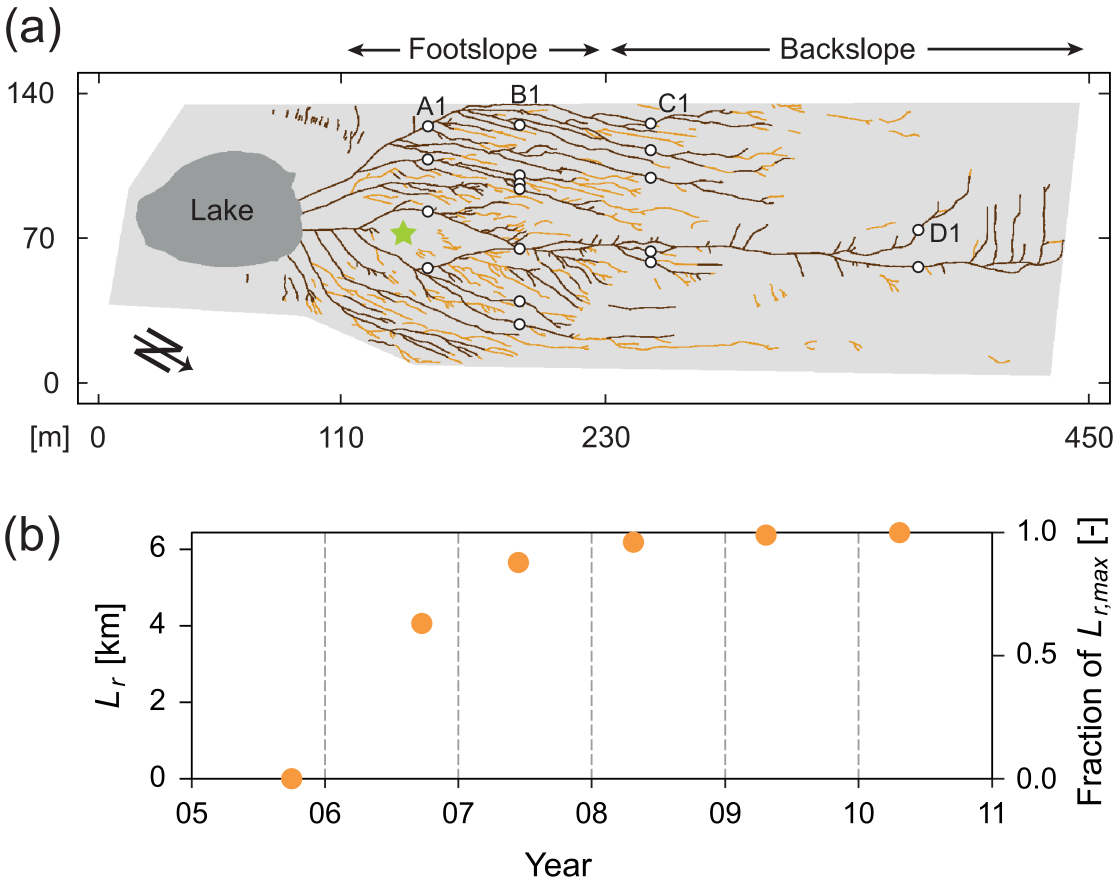

Figure 2.10: Erosion rill evolution with time. (a) Backbone of the rill network extracted from aerial images. The dark brown lines denote the rill network formed in the first year (October 2005 – September 2006). The orange lines represent the rills, which developed after the first year until April 2010. The circles indicate the positions of the rill depth measurements obtained by laser scanning. The positions are enumerated from West to East along the transects. The first position of each transect is marked in the figure with the name of the transect and the number 1 (e.g. A1: A for A-transect and 1 for the first measurement position in the transect). The green star marks the location of the weir facility. (b) Evolution of the total erosion rill length L_r. Rill evolution in the figure starts from the unrilled state of the surface in October 2005 and ends with the most actual aerial image available in April 2010. Rill growth was intense in the first year and successively decreased afterwards. The network length in 2010 is considered as maximum total rill length. In the first year 63 % of the total network length developed.

verse transects in the catchment. The data were obtained by a Riegl LMS-Z420i laser scanner mounted on a 6 m high tower on various positions inside of the catchment. The four transects were extracted from the data and a raster based minimum filter was applied to remove the vegetation from the data. To reconstruct the surface without the rills, a spline with 30 degrees of freedom was fitted using a 90 %-quantil regression (R Development Core Team, 2008; Koenker, 2011). The distances from the measured minimum points to this spline was used as rill depth. By applying a local minimum finder ('peak' from Ruckstuhl et al., 2010) the major individual rills were extracted. The depth measurements of totally 18 rills (Figure 2.10a) were used to compare the simulated with the observed rills.

3 Subsurface drainage pathways

3.1 Motivation

Catchment discharge after rainfall events is a nonlinear relationship of the rainfall pattern controlled by the catchment topography, soil hydraulic properties and spatial arrangement of hillslope elements. Regarding the spatial arrangement of hillslope structures the concept of hydrologic connectivity was recently introduced. In a broad sense, hydrologic connectivity relates to the passage of water from one part of the landscape to another, eventually generating a catchment runoff response (Bracken and Croke, 2007). However, as Stieglitz et al. (2003), we confined our definition of hydrologic connectivity to the condition by which disparate regions on the hillslope are linked via subsurface water flow. These flow paths consist of soil regions of increased hydraulic conductivity due to high soil moisture content, coarse texture or macropores. In catchment and hillslope hydrology, hydrologic connectivity becomes especially important if the network of subsurface flow paths connects to the outflow of the system and substantially contributes to stream runoff. Research on the generation of connected subsurface flow paths, the dynamics of merging and disconnection of conductive patterns and the spatial extension of flow path networks has become an intense area of research in recent years. However, there is still a lack of understanding regarding controls on development and spatial distribution of subsurface flow paths, and the relation of hydrologic connectivity to stream runoff. One reason for this uncertainty is the difficulty to deduce subsurface flow paths directly from field observations. Although there are several studies where subsurface flow paths were measured directly by geophysical methods (e.g. Gish et al., 2002; Holden, 2004) or where flow paths were derived from chemical analysis of soil water (e.g. Prestrud Anderson et al., 1997; Hogan and Blum, 2003), the localisation of subsurface flow paths at the catchment scale remains an unsolved issue. In addition to the unknown spatial distribution of conductive hillslope elements, the uncertainty regarding hydraulic functions and conditions of the soil constituents such as hydraulic conductivity (Nyberg, 1995) or initial soil moisture (Merz and Plate, 1997; Bronstert and Bárdossy, 1999) lead to considerable difficulty to predict catchment discharge.

With increasing availability of digital elevation models (DEMs) topography was often used as an indirect pointer for water flow paths. Hydraulic gradients derived from surface topography have been widely used in topographic indices to simulate the direction of flow paths (e.g. Beven and Kirkby, 1979; Sivapalan et al., 1987; Barling et al., 1994). However, the use of such indices has been questioned for catchments with distinctly different bedrock topography than surface topography. Freer et al. (1997) and Freer et al. (2002) have shown that the bedrock surface can have a considerable influence on local hydrological gradients and therefore the dominant flow path directions. Tromp-van Meerveld and McDonnell (2006) formulated the fill and spill hypothesis, stating that bedrock depressions on the hillslope have to be filled by the transient water table before water spills over the microtopographic relief in the bedrock and connects to other saturated areas and eventually to the outflow. A similar mechanism was observed by Spence and Woo (2003) for a soil filled valley on the subarctic Canadian Shield, where segments of the valley, representing storages, have to be filled above their capacity before spillage allows flow in downslope direction.

The sudden connection of subsurface flow paths to the hillslope or catchment outflow was used to explain the highly nonlinear relationship between rainfall and subsurface stormflow observed in many catchments (Lehmann et al., 2007; Tromp-van Meerveld and McDonnell, 2006). It was only recently that the threshold-like behaviour of this process has been noticed as an emergent behaviour at the hillslope scale (McDonnell, 2003). Further research is needed for a clearer understanding of the linkages between patterns and processes, i.e. the internal hillslope conditions that create the threshold behaviour (McDonnell et al., 2007).

In this Chapter we investigate the three-dimensional structure and connectivity of subsurface flow paths in the catchment and we examine the impact of flow path connectivity on catchment runoff. As already outlined in the introduction the study intends to answer the following questions:

- Where do subsurface drainage pathways evolve in the catchment?
- What are the factors controlling the establishment of a flow path network?
- How does subsurface flow path connectivity relate to the observed rainfall threshold for catchment runoff?

We hypothesise that the evolving flow path structures in the catchment depend on small-scale heterogeneity of soil physical and hydraulic properties, soil depth and slope topography. To model subsurface drainage pathways we need three-dimensional models with accurate spatial resolution to reconstruct relevant heterogeneities. Due to the hydraulic properties of the soil material from the Chicken Creek catchment with a threshold-like behaviour regarding water flow (high conductivity for wet conditions and limited conductivity for dry soil) we will apply Percolation Theory to model the drainage network in three dimensions. In Section 3.2 the concepts of percolation theory and its application on subsurface flow in the man-made catchment are introduced. The results of the three-dimensional percolation model are presented in Section 3.3 and discussed in Section 3.4, followed by concluding remarks in Section 3.5.

3.2 Application of Percolation Theory

3.2.1 Basic concept of Percolation Theory

Percolation Theory is a useful tool to describe and quantify complex structures and relationships between connectivity and threshold phenomena (Hunt and Ewing, 2009). In the following section the core concept of Percolation Theory and its relation to catchment hydrology are briefly introduced. As an artificial example we choose water flow on a simplified hillslope represented by a two dimensional orthogonal lattice with $x \times y$ cells, where y_{max} represents the top of the slope and the outflow is located at y_{min} (Figure 3.1a). Every cell $i_{(x,y)}$ of the lattice can be in one of two states, either occupied or non-occupied, and defines in the context of hillslope drainage if a hillslope element is ‘open’ or ‘closed’ regarding water flow. By definition the state of a cell, occupied or non-occupied, is assigned by a random process (Broadbent and Hammersley, 1957) and is independent of the state of the other cells (Figure 3.1b). The occupation probability p describes the fraction of occupied cells in the system. For a certain occupation probability p the distribution of the cell states can be achieved by assigning to every cell a random value R between 0.0 and 1.0. Comparing R to the occupation probability p a cell becomes occupied if $R \leq p$ and non-occupied if $R > p$. For lattices of infinite size the occupation probability equals the fraction of occupied cells. Note

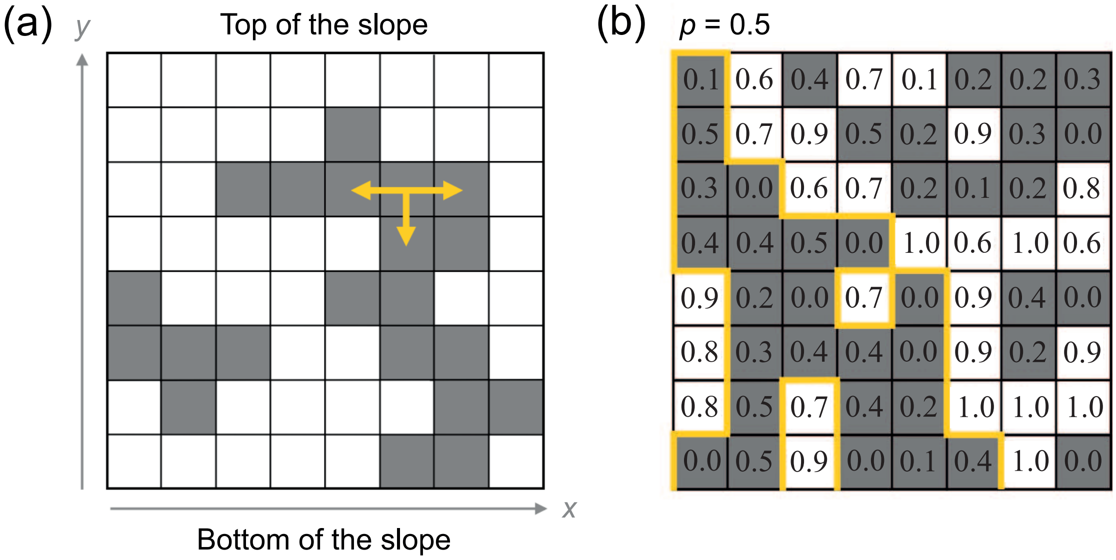

0.1	0.6	0.4	0.7	0.1	0.2	0.2	0.3
0.5	0.7	0.9	0.5	0.2	0.9	0.3	0.0
0.3	0.0	0.6	0.7	0.2	0.1	0.2	0.8
0.4	0.4	0.5	0.0	1.0	0.6	1.0	0.6
0.9	0.2	0.0	0.7	0.0	0.9	0.4	0.0
0.8	0.3	0.4	0.4	0.0	0.9	0.2	0.9
0.8	0.5	0.7	0.4	0.2	1.0	1.0	1.0
0.0	0.5	0.9	0.0	0.1	0.4	1.0	0.0

Figure 3.1: Schematic percolation model for a simplified hillslope. (a) The dark cells are occupied, i.e. conductive to water flow. The cluster (group of connected occupied cells) on the left does not account for runoff at the bottom of the slope in contrary to the draining cluster on the right. Due to gravity, water flow is only allowed in horizontal and downslope direction as indicated by the yellow arrows. (b) To determine the state of a cell a random number between 0.0 and 1.0 is assigned to each cell and all cells with random number below or equal the chosen occupation probability p ($p = 0.5$ in this example) become occupied. When increasing p gradually from 0.0 to 1.0 more and more cells become connected and eventually a percolating cluster is established. In the given example a percolating cluster (yellow framed cluster) occurs at $p = 0.5$. Note that each cell can only be connected to the four closest neighbours.

that for small lattices the fraction of occupied cells can deviate from the defined occupation probability p.

In addition to the state of a cell its neighbourhood must be specified. A cell is connected to a certain number of cells (for example the four adjacent cells in orthogonal direction) defined as coordination number Z of the lattice. In a hydrological context an open cell can exchange water with the open cells of its neighbourhood. Due to the focus on gravity driven flow in this study a cell at position (x, y) cannot exchange water with a neighbour above $(x, y + 1)$, limiting water exchange to the cell below and the left and right neighbours at the same level.

A cell is connected to a neighbour if both cells are occupied. A set of connected cells surrounded by non-occupied cells is called a cluster. As all cells in a cluster are open to flow, a cluster is able to conduct water. A cell contributes to outflow from the hillslope if the cluster touches the bottom line of the slope. We call these clusters that are connected to the outflow boundary at the bottom as 'draining clusters'.

With increasing occupation probability p clusters merge and the average size of a cluster increases. At the critical occupation probability denoted as percolation threshold p_c a percolating cluster, i.e. a cluster from the top of the slope to the outflow, establishes and water is able to percolate all through the system (Figure 3.1b). As the percolation threshold depends on the random distribution of states, several simulation runs from $p = 0.0$ to $p = 1.0$ with different random number distribution are required to determine the average percolation threshold of the lattice. Stauffer and Aharony (1992) defined the percolation threshold as

$$p_c = \int_0^1 p \left(\frac{d\Pi}{dp} \right) dp \tag{3.1}$$

where Π denotes the percolation probability, which is defined as the ratio between the number of realisations with percolating cluster (for a certain occupation probability p) and the total number of realisations with occupation probability p.

3.2.2 Model adaption to hillslope geometry

Modelling the complex three-dimensional drainage pathways in the Chicken Creek catchment required several adaptations compared to the simple percolation example presented in the previous section. A three-dimensional simple cubic lattice was used to discretise the geometry of the catchment. In order to realistically represent the relevant structures of subsurface flow a high resolution (0.25 m) in each of the lattice directions x, y and z was chosen. Following the variable catchment extension in x-, y- and z-direction the discretised lattice obtains a specific shape with irregular boundaries and an average slope gradient of 2°.

The simple cubic lattice was further discretised to a face-centred cubic (fcc) lattice. The basic structure of the fcc lattice for a cell and its twelve neighbours is shown in Figure 3.2a. The advantage of the fcc lattice over the simple cubic lattice is its high cell connectivity ($Z = 12$ for the fcc lattice compared to $Z = 6$ for the nearest neighbours of the simple cubic lattice) favouring the representation of systems, where connectivity plays a key role. However, we consider only gravity driven water flow in the model, thus the neighbourhood of a lattice cell $i_{(x,y,z)}$ is not defined by the full fcc neighbourhood, but only by the eight neighbouring cells located topographically at equal height or lower. We further refer to the modified fcc lattice set up for the Chicken Creek catchment as the 'Chicken Creek lattice'. The effective size of the lattice consists of 3 661 303 cells, where each cell represents the volume V_i of a rhombic dodecahedron of 31 litres in volume (Figure 3.2b).

3.2.3 Percolation threshold of hillslope model

Before we will analyse the drainage behaviour of the Chicken Creek lattice, we compare it to properties of other three-dimensional lattices with well-defined properties. Silliman and Wright (1988) have shown that the percolation threshold of a finite simple cubic lattice depends on lattice size. Chatzis and Dullien (1977) have reported that a minimum lattice size in the order of $20 \times 20 \times 20$ cells is reasonable to approximate the percolation threshold of an infinite lattice. In another study, Silliman (1990) investigated the extensions in x-, y- and z-direction of a simple

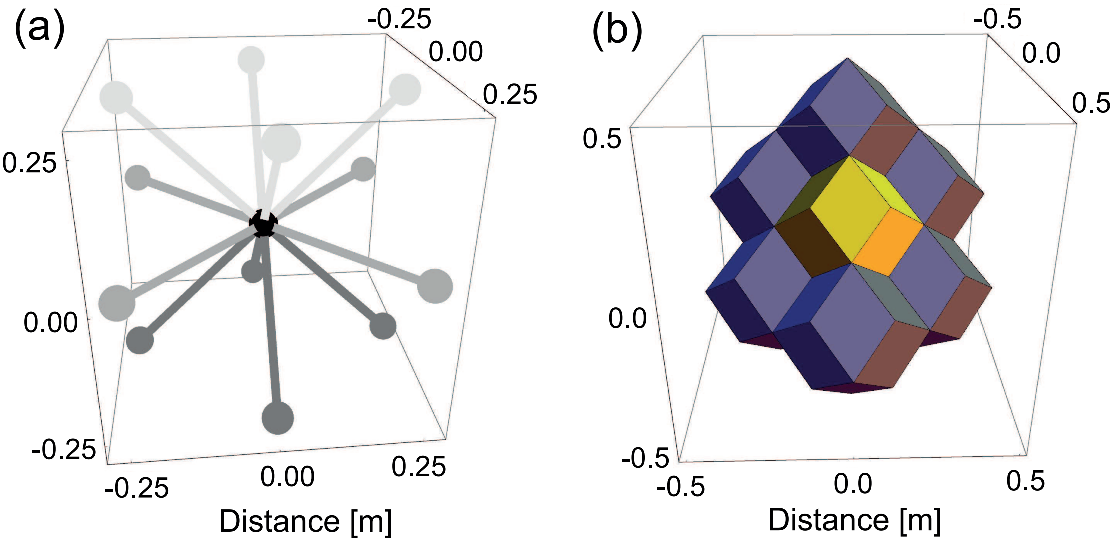

Figure 3.2: Three-dimensional model lattice structure of the percolation model. (a) Basic structure of the face-centred cubic (fcc) lattice for a resolution of 0.25 m. A cell (black sphere) is connected to the 12 neighbouring cells at distance $\sqrt{2}$ 0.25 m (grey spheres). (b) Representative volume V_i of a cell in the fcc lattice (yellow) and six neighbours (blue). The unit volume V_i equals 31 litres for the lattice resolution of 0.25 m.

cubic lattice and found the vertical dimension z to be crucial for the value of the percolation threshold. Independent of the lateral lattice extensions x and y (for x and $y > 5$) a reduction of the vertical dimension z to a value of 10 hardly affected the percolation threshold value of the simple cubic lattice, whereas for $z < 10$ the percolation threshold increased exponentially with decreasing z (Silliman, 1990). Additionally, the percolation threshold of a three-dimensional lattice depends on the coordination number Z, i.e. on the average connectivity of a lattice cell. The percolation threshold decreases with increasing coordination number as has been shown for three-dimensional lattice structures with different coordination number (Sahimi, 1994). Ewing and Gupta (1993) tested the effect of a varying coordination number between 1 and 6 for the simple cubic lattice and also showed an increase of the percolation threshold with decreasing coordination number.

To assess the effect of size, shape, slope and neighbourhood on the percolation threshold of the Chicken Creek lattice, we used three test lattice configurations of the same size (i.e. number of cells) as the Chicken Creek lattice. We designed the ‘box lattice’ ($x = y = z = 194$ cells) to assess the influence of lattice size, the ‘sheet lattice’ ($x = 1750$, $y = 525$, $z = 8$) to examine the effect of the lattice shape, and the ‘slope lattice’ ($x = 1750$, $y = 525$, $z = 8$) to test the effect of a slope gradient of 2°. Additionally, the effect of neighbourhood was tested by simulating each of the three lattice configurations with the full fcc neighbourhood (12 neighbours) and with the modified fcc neighbourhood used for the Chicken Creek lattice (8 neighbours). The percolation thresholds were calculated according to Equation (3.1) for all three test lattice configurations with full and modified fcc neighbourhood, respectively.

To check the minimum number of realisations needed in order to determine the percolation threshold of the Chicken Creek lattice, we performed 80 realisations for each of the test lattices (Appendix). As only the fourth decimal of the percolation threshold is affected after 50 realisations for all of the test lattice configurations, we consider 50 realisations to be appropriate to calculate the percolation threshold (and other properties) of the test lattices and the Chicken Creek lattice.

Figure 3.3a shows the percolation thresholds for the three test lattices with the full fcc neighbourhood. Since the percolation threshold for the box lattice (0.200) is very close to the threshold approximated for the infinite fcc lattice, 0.199 (Lorenz and Ziff, 1998), the number of cells included in the Chicken Creek lattice is considered large enough to minimise the effect from lattice size. The percolation threshold for the sheet lattice was calculated to 0.252. The difference of percolation threshold between the box lattice and the sheet lattice can be explained on the one hand by the increase of surface for the sheet lattice. A cell at the lattice boundaries only has 3, 5 or 8 neighbours depending on the cells location at a corner, boundary edge or boundary face, respectively. This leads to a small reduction of the coordination number causing lattice connectivity to decrease. On the other hand, the reduced lattice extension in z-direction from 194 to 8 cells significantly decreases the probability for the formation of a percolating cluster in x-y-direction of the sheet lattice. Both effects account for a higher percolation threshold. The percolation threshold for the slope lattice with a gradient of 2° is 0.253 and demonstrates that the slope gradient has a negligible effect on the fcc lattice with full neighbourhood.

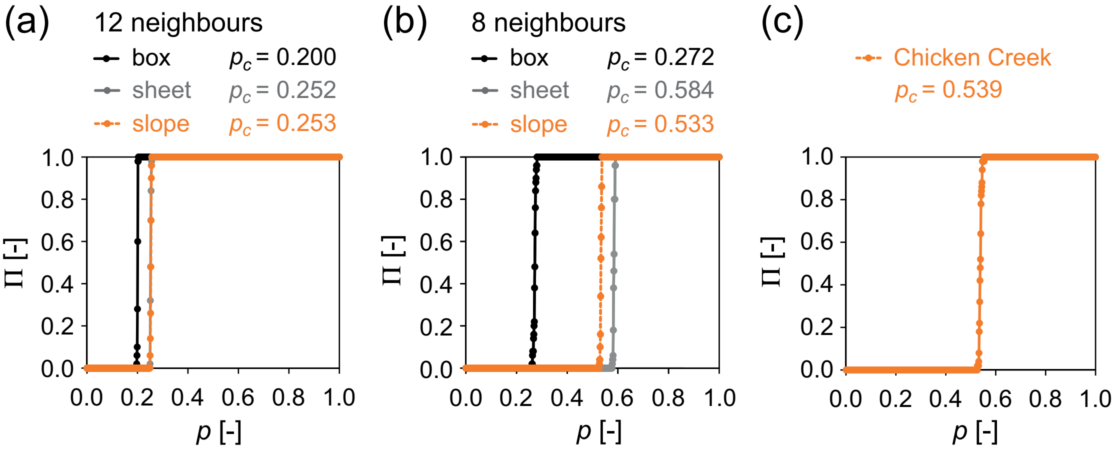

Figure 3.3: Percolation thresholds deduced from Π, the ratio between realisations with a percolating cluster and the total number of realisations with occupation probability p. At the percolation threshold the value of Π changes from 0.0 to 1.0. The lattice used to model the Chicken Creek catchment is compared to lattices of the same size with different geometries (cubic system denoted as 'box', flat system 'sheet' and flat system with a 'slope'. (a) For lattices with 12 neighbours the percolation threshold for the sheet and the slope lattice is higher compared to the box lattice due to a limited number of connections in z-direction. (b) For coordination number 8 all threshold values are increased. The difference between the sheet and slope lattice reveals the effect of slope on percolation properties. (c) The percolation threshold of the 'Chicken Creek lattice' (connectivity 8) is close the value determined for the slope lattice.

Figure 3.3b shows the percolation thresholds for the three test lattice configurations with 8 neighbouring cells. For the box lattice the connectivity reduction from 12 to 8 neighbours led to the increase of the percolation threshold to 0.272. For the sheet lattice and the slope lattice the percolation threshold increased drastically to 0.584 and 0.533, respectively. Again, this can be explained by the increased surface of the sheet lattice and the slope lattice and the fact that the average coordination number of the system is reduced from 12 to 8 neighbours. While the percolation thresholds were almost identical for sheet lattice and the slope lattice in case of coordination number 12, the slope lattice has a smaller percolation threshold than the sheet lattice for $Z = 8$. In case of the sheet lattice it is impossible that a cell at the bottom layer (maximum soil depth) is connected to a cell below because the bottom layer is flat. For the slope lattice this is different because a cell at the bottom can be connected to a cell below located in downslope direction.

The average percolation threshold of the Chicken Creek lattice for the 50 simulation runs is 0.539 (Figure 3.3c) and is very similar to the percolation threshold of the slope lattice. The analysis of the different test lattice configurations shows that the high percolation threshold of the Chicken Creek system can be explained by the combination of two types of connectivity reduction. The first and more important one is attributed to the reduction of the coordination number from 12 to 8. The second lattice connectivity reduction arises from the narrow system shape leading on the one hand to a large lattice surface, and thus to more lattice cells at the boundary having a coordination number smaller than eight, and on the other hand to a reduced probability of percolating cluster formation in x-y-direction.

3.2.4 Definition of occupation probability and drainage capacity in a hillslope model

As described above, an open cell corresponds to a hillslope element that can drain and conduct water. While a random number between 0.0 and 1.0 was used in the simplified example of Section 3.2.1 to define the state of a cell, we have to interpret the random value assigned to each cell from a soil physical point of view. The hydraulic conductivity of the sandy soils in the catchment is very sensitive to water content with large conductivity values for wet and small values for dry conditions. We define a 'free water capacity threshold' θ_t separating conductive ($\theta > \theta_t$) and non-conductive cells ($\theta \leq \theta_t$), assuming that for conductive cells hydraulic conductivity is not limited and water can flow into the lake within a rainfall event. To determine θ_t we used a concept presented in Lehmann et al. (2008). They linearised the water retention function (relationship between capillary pressure and water content) with a tangent defined at the maximum of the pore size distribution function. This line was used to define the disconnection of liquid structures in the sand media. The maximum of the pore size distribution corresponds to the inflection point of the water retention curve. Below the water retention curve according to the van Genuchten parametric model (van Genuchten, 1980) and the free water capacity threshold are given:

$$\Theta = \frac{\theta\left(h\right) - \theta_r}{\Phi - \theta_r} = \left(1 + \left(ah\right)^n\right)^{-\left(1 - \frac{1}{n}\right)} \tag{3.2}$$

$$\theta_t = \left(\Phi - \theta_r\right)\theta_r \left(2 - \frac{1}{n}\right)^{\left(\frac{1}{n} - 1\right)} \tag{3.3}$$

Θ is the effective water saturation, $\theta\left(h\right)$ is the water content at pressure h, θ_r is the residual water content, Φ is the porosity, α is the inverse of a characteristic pressure head, and n is the pore size index. In Figure 3.4a the determination of the threshold water content is shown in an example.

The free water capacity threshold was calculated based on the van Genuchten parameters of all the 316 texture sample sites introduced in Section 2.3.1. Thereafter, we computed the free water capacity threshold values for all the water retention curves according to Equation (3.3). We assume that texture properties, and therefore free water capacity threshold values, are randomly distributed in space. Technically, we assigned random values between 0.0 and 1.0 to all lattice cells. The random numbers were then converted to free water capacity threshold values according to the sum distribution of the 316 texture sample sites (Figure 3.4b).

For the modelling approach presented in this study, we assume uniform soil water content for the entire catchment. Thus, the volumetric water content θ was defined to be equal for each cell of the lattice. For $\theta \leq \theta_{t(x,y,z)}$ no drainable water from the lattice cell $i_{(x,y,z)}$ is available, but for $\theta > \theta_{(x,y,z)}$ drainable water is present at the cell. The lake at the topographically lowest region of the catchment is set as the outflow for the percolation model. Connected cells with water contents above the free water capacity threshold value form clusters. The clusters, which are connected to the lake are called ‘draining clusters’ and represent the drainage pathways. A cell belonging to a draining cluster is called a ‘draining cell’. Note that a cell with drainable water not being part of a draining cluster cannot contribute to catchment runoff. The volume of drainable water from a cell $V_{w(x,y,z)}$, the total volume of drainable water (i.e. the entire subsurface flow from the catchment) V_d, and the total amount of drainable water d scaled according to the catchment area, are given as

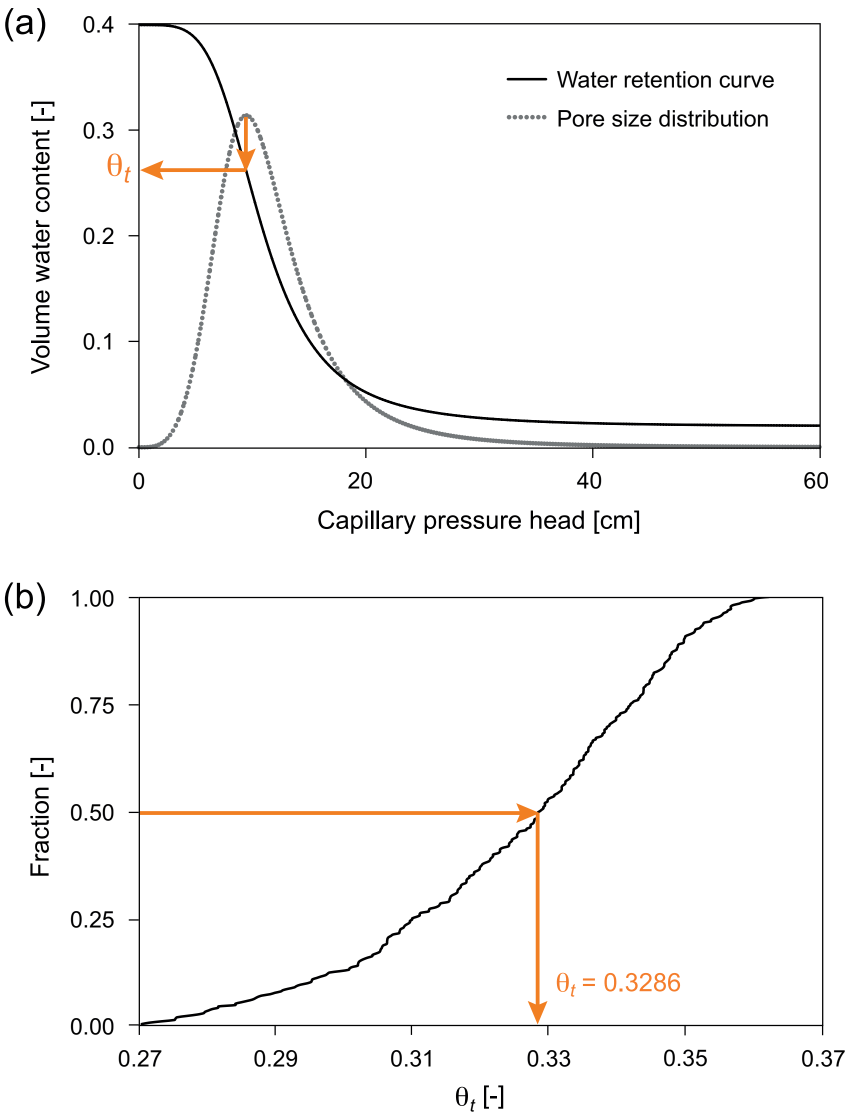

Figure 3.4: Determination of the threshold water contents and their allocation to the model cells. (a) Definition of the free water capacity threshold θ_t as the corresponding water content at the inflection point of the water retention curve. The inflection point denotes the maximum of the pore size distribution. The pore size distribution is expressed as the absolute value of the first derivate of the water retention curve (displayed schematically in the figure). (b) Sum curve of the free water capacity threshold values derived from the 316 sample sites. The random numbers between 0.0 and 1.0 allocated to the lattice cells were transformed to free water capacity thresholds according to the sum curve. For example, the random number 0.5 yields a free water capacity threshold of 0.3286 (arrows). Linear interpolation was used between the 316 points of the sum distribution curve so that there is a corresponding free water capacity threshold value for any number between 0.0 and 1.0.

$$V_{w(x,y,z)} = V_i \left(\theta - \theta_{t(x,y,z)}\right) \quad \text{for } \theta_{t(x,y,z)} < \theta < \Phi_{(x,y,z)} \tag{3.4}$$

$$V_d = \sum_{\Omega} V_{w(x,y,z)} \tag{3.5}$$

$$d = \frac{V_d}{A_s} \tag{3.6}$$

θ is the catchment water content, $\Phi_{(x,y,z)}$ is the porosity at the cell $i_{(x,y,z)}$, Ω denotes the set of cells belonging to a draining cluster and A_s is the catchment area.

We analysed draining clusters, when the water content in the catchment was gradually increased from 0.2701 to 0.362, according to the minimum and maximum free water capacity threshold. We paid special attention to the behaviour of draining clusters near the percolation threshold. The results are presented in the next section.

3.3 Results

3.3.1 Characterisation of drainage pathways

Figure 3.5a shows how draining clusters develop with increasing water content from 0.3286 to 0.3310 (corresponding to the occupation probability from 0.50 to 0.54) for a single simulation run. Up to the water content of 0.3291 ($p = 0.51$) draining clusters (connected to the lake) are only found in the immediate vicinity of the lake. This is because the cells in the catchment containing drainable water ($\theta > \theta_t$) are poorly connected and therefore the probability that a large draining cluster establishes is small. However, with rising water content the number of cells with exceeded free water capacity threshold is augmented, increasing the probability that draining clusters expand and merge. For the water content 0.3294 draining cells near the lake suddenly connect to an upslope cluster and a large draining cluster forms across the clay wall on the orographic left hand of the catchment. This dominant cluster further expands with increasing water content. For the

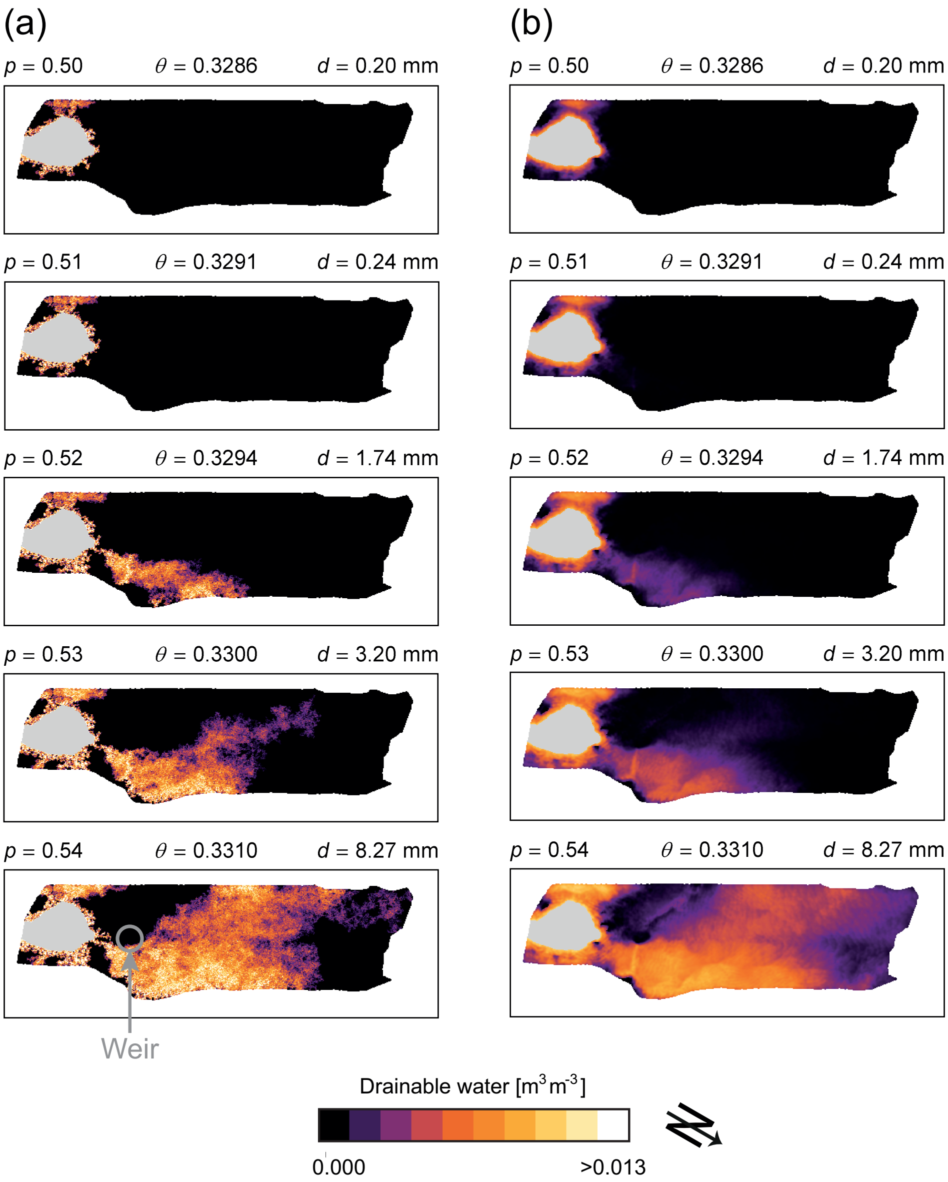

Figure 3.5: Modelled drainage pathways showing the concentration [$\mathrm{m^3\,m^{-3}}$] and total depth d [mm] of drainable water connected to the lake for an increasing occupation probability p (steps of 0.01) starting from $p = 0.50$ and ending with $p = 0.54$ (corresponding to a catchment water content θ between 0.3286 and 0.3301). The results are displayed as two-dimensional projections upscaled to 1 m resolution. The grey area marks the lake. (a) Results for a single realisation of randomly distributed free water capacity thresholds. (b) Average of 50 realisations, filtered by a 3×3 moving window. Note that a small change of water volume in the system has a huge impact on the amount of drained water. For high water contents the drainage pathways cross the clay wall at the orographic left side of the catchment.

water content 0.3301 a percolating cluster establishes and hydrologically connects the lake with the top of the slope.

Figure 3.5b shows the average amount of drainable water of 50 realisations with different underlying random distribution of free water capacity threshold values. The essential characteristics of the single realisation, i.e. the strong tendency for draining clusters to establish on the orographic left hand side of the catchment and the immediate growth of the main draining cluster between the water content 0.3291 and 0.3310 are also revealed with the average of 50 simulations.

3.3.2 Controls on the development of drainage pathways

The catchment geometry has a large influence on the connection of draining cells. This becomes evident when the growing of flow paths with increasing water content is investigated more closely. The region of shallow soil depths around the lake is represented by few cells in the vertical extension of the model lattice, causing a reduction of the probability that cells with drainable water occur in this region. Consequently, the connection of draining cells in the vicinity of the lake with upslope clusters does not establish easily and often depends only on a few cells acting as bottleneck. This is illustrated in Figure 3.6 showing the three-dimensional flow paths of a single simulation for a catchment section near the lake. At $p = 0.52$ the draining cells near the lake connect to upslope clusters and a large draining cluster is formed, which extends far across the clay wall on the orographic left hand side of the catchment. This demonstrates that the rather low clay wall on the eastern part of the catchment does not act much as a barrier to flow path connection. However, on the western catchment part the combination of shallow soil depths around the lake and a high clay wall virtually prevent flow patterns to form across the western clay wall for the range of water content displayed in Figure 3.5. Nevertheless, for a few of the 50 simulations the main draining cluster at water content 0.3310 develops a branch on the orographic right hand side of the catchment. This is indicated by the small values of drainable water in the area around the clay wall northwest from the lake. This area becomes better connected to the lake only for wetter conditions in the catchment.

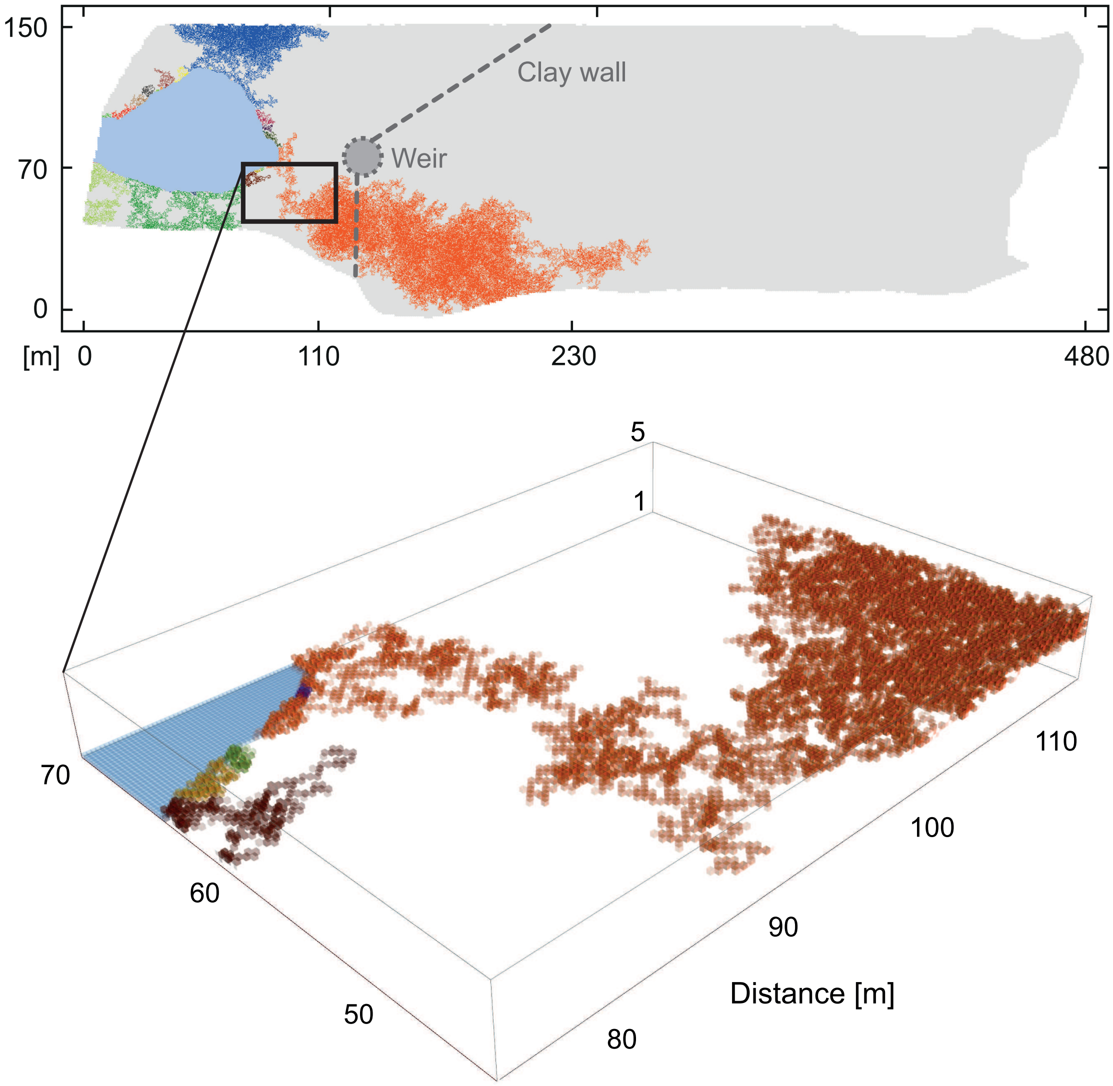

Figure 3.6: Draining clusters for a single realisation at water content 0.3294 ($p = 0.52$) and detailed three-dimensional view of a section showing different clusters connected to the lake. A draining cell connected to the lake is represented by a coloured cube. The relatively sparsely connected areas close to the lake reflect the shallow soil depths in this area. Whether a large cluster can form is highly depending on the connections of cells in this area. The large reddish cluster, for example, is connected only through a few cells around $x = 97$, $y = 62$, $z = 2$ acting as bottleneck for outflow.

It is apparent from the simulation results presented in Figure 3.5 that the weir facility does not manage to concentrate the subsurface flow paths and to capture the entire subsurface flow. This was already indicated by the unreliably low subsurface flow values measured at the weir.

3.3.3 Outflow

The evolution of simulated draining clusters describes the transition from an unconnected to a highly connected system as a nonlinear, threshold-like process depending on a very small increase in water content. Figure 3.7 shows that a rise in water content of only 0.0029 (from 0.3291 to 0.3320 or from $p = 0.51$ to $p = 0.56$, respectively) close to the percolation threshold ($p_c = 0.539$) is needed to switch the system from an unconnected state with a fraction of draining cells of only 0.007 to a highly connected state with a fraction of draining cells of 0.478. For the poorly connected state the outflow does not exceed 0.3 mm, but as soon as the main draining cluster connects to the upslope catchment area the outflow increases drastically. The small water content increase from 0.3291 to 0.3320 (from $p = 0.51$ to $p = 0.56$) accounts for the seventyfold increase of outflow from 0.3 to 21.4 mm (Figure 3.7). For water contents exceeding 0.3320 ($p = 0.56$) the relation between water content and outflow is described by an almost linear function. For high water contents (> 0.3387, i.e. $p > 0.7$) the fraction of draining cells nearly equals the occupation probability illustrating that virtually all cells containing drainable water are connected and contribute to the outflow.

Comparing the simulated amount of drainable water with the measured catchment runoff (Figure 2.6) reveals that the simulated values are in the right order of magnitude. The maximum measured runoff peak lies between 30 and 57 mm (depending on the number of days without rainfall chosen to separate precipitation events) corresponding to the occupation probability 0.652 and 0.936, indicating a highly saturated catchment, respectively. However, keeping in mind that the measured outflow integrates subsurface flow and surface runoff the outflow peaks for subsurface flow from the catchment are considered to be somewhat lower.

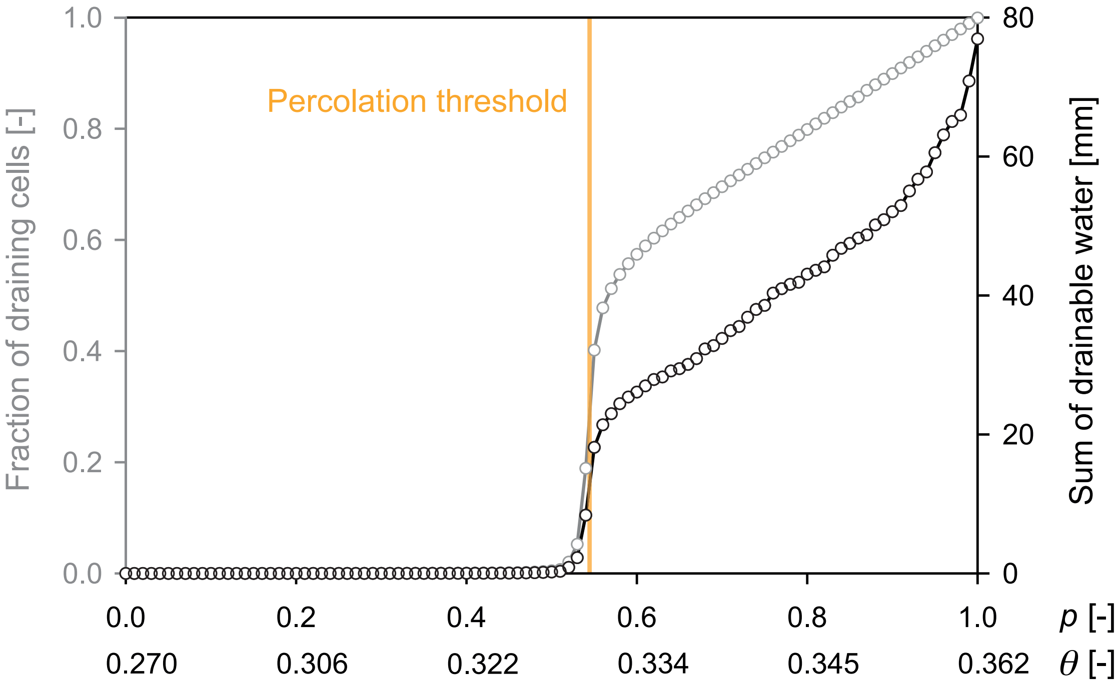

Figure 3.7: Sum curve of drainable water (black circles) and fraction of draining cells (grey circles) for an increasing occupation probability or water content, respectively. The curves represent the average of 50 simulation runs. At the percolation threshold many cells with drainable water form a connected structure resulting in tremendous increase of outflow.

3.4 Discussion

3.4.1 Drainage pathways

In the past few years the role of hydrologic connectivity for catchment outflow and rainfall-runoff behaviour has been recognised for many hillslopes and small catchments. McDonnell (2003) suggested reconsidering common hydrological concepts (such as the variable source area concept, the assumption of a steady-state catchment water table, or the use of topography as a surrogate for flow paths) widely used in hydrological models, because they are not able to describe these threshold-like processes. Although a few studies relating subsurface flow path connectivity and nonlinear catchment outflow have been published recently (e.g. Ocampo et al., 2006; Tromp-van Meerveld and McDonnell, 2006; Lehmann et al., 2007), there is still a lack of understanding about the properties controlling the flow path patterns along a hillslope and how these processes relate to catchment runoff. The present study tackled these issues and gave more insight into the relationship between drainage patterns and subsurface flow.

Percolation theory was applied to describe the drainage pathways in a heterogeneous system consisting of elements in one of two hydraulic states (high or limited conductivity). Percolation theory is appropriate to relate connectivity to threshold phenomena, such as the establishment of a flow path network. The model showed that drainage pathways develop mainly on the orographic left hand side of the Chicken Creek catchment and do not concentrate at the weir in the clay wall as it was planned when the catchment was constructed. Several indicators support these simulation results: the unreliably low subsurface flow values measured at the weir, visual observations (moist structure lakewards from the wall described in Figure 2.7) and soil moisture data (soil moisture difference index described in Figure 2.8). While the 'true' spatial distribution of hydraulic properties is unknown and is chosen based on the distribution of the measured soil properties (Figure 3.4b) the three-dimensional percolation model includes the true geometry (slope, soil depth) of the system. Based on the percolation model a subsurface flow path network is generated as a function of hydrologic connectivity determined by small-scale variables such as soil depth, slope gradient, microtopography of the clay layer and water content. These variables account for the highly threshold-like establishment of the flow path network connecting the outflow (i.e. the lake) with the upslope part of the Chicken Creek catchment. The sudden connection of drainage pathways to a large network involves the instantaneous availability of a large amount of drainable water causing the observed nonlinear behaviour of catchment runoff (Figure 2.6). For precipitation events with a sum of rainfall smaller than 9 mm the occupation probability of the catchment remains lower than the percolation threshold (Figure 3.7). However, as soon as the rainfall threshold of 9 mm is exceeded the percolation threshold is reached and outflow is suddenly initiated.

The percolation model developed in this study emanates from uniform catchment water content without relating it to precipitation events, temporal dynamics or depth dependent soil water content. Therefore, the model should not be compared to a distributed hydrological model describing the dynamics of runoff behaviour in detail. The goals of the percolation model were to explain the nonlinear rainfall-runoff response and to simulate the subsurface flow paths by relating connectivity to soil physical properties and to catchment geometry. With this model approach alternative aspects of subsurface flow generation are added to the scientific field of hydrological modelling.

3.4.2 Model assumptions

3.4.2.1 Model structure

The evolving drainage pathways in the Chicken Creek catchment were very sensitive to the spatial distribution of soil depth and hydraulic properties (conductive or not). Therefore the chosen model must represent structures with a reasonably high resolution. The resolution of 0.25 m in the three lattice directions x, y and z has proven to capture the flow paths indicated by measurements and field observations. However, it has been shown that the establishment of flow path connectivity often depends only on a few lattice cells in the vicinity of the lake even for the small lattice resolution of 0.25 m. Convergence studies for an increasing lattice resolution will give more insight into the relationship between the threshold-like establishment of flow path connectivity and lattice resolution.

Regarding further development of the percolation model the spatial lattice resolution of 0.25 m is appropriate as it is able to capture evolving small-scale structures, such as vegetation patterns, the length of plant roots or surface erosion rills. The evolving vegetation and erosion rill patterns are assessed on the one hand from recurring aerial pictures and on the other hand from high resolution digital elevation models based on a periodic laser scanning of the catchment surface.

Connectivity is an essential feature of flow path development and has to be represented adequately in the model. We used the modified face-centred cubic (fcc) lattice with 8 neighbours to describe the hydrologic connectivity of hillslope elements. The use of the full simple cubic lattice neighbourhood with 26 neighbours or 17 neighbours in gravity driven flow direction, respectively, would certainly refine the results quantitatively. However, the fcc structure of the lattice has the benefit of being equidistant. This is a considerable computational advantage for model studies on soil water dynamics.

3.4.2.2 Water content

In its current state the model describes the subsurface flow paths for static moisture conditions in the catchment. By gradually increasing the water content in the whole catchment we mimicked a very much simplified process of saturating the system. Nevertheless, the assumption of equal water content is rather unrealistic as soil moisture varies within the soil. However, using equal water contents, it was possible to test the sensitivity of outflow patterns on small-scale soil physical heterogeneities. Further simulations including spatially heterogeneous soil water contents, for example increasing water contents with soil depth, could give more insight into the behaviour of subsurface flow paths development. Time-domain reflectometry, tensiometer and groundwater level measurements currently conducted in the catchment will yield the required information about the location of the groundwater table and the distribution of moisture in the soil profile to define realistic distribution of these variables in the model.

3.4.2.3 Water flow

We considered only gravity driven water flow, which is expressed in the model by the rule that a cell is only allowed to connect to a neighbouring cell lying at the same level or below. The model does not account for upward flow such as capillary rise. However, capillarity is a secondary process the Chicken Creek catchment, due to the rather coarse texture of the soils, causing only a small vertical extension of the capillary fringe.

The free water capacity threshold determining the amount of drainable water of a cell is based on soil texture. This implies that macropore flow or pipe flow is neglected in the model. We justify this with the consideration that at the initial state of the catchment evolution the processes accounting for macropores or pipes (e.g. animal burrowing or plant root decay) are playing a minor role.

Since the focus of the present study lies on subsurface flows, surface runoff was not considered in the model, although it is an important runoff component in the current state of development of the Chicken Creek catchment. For this study, neglecting surface runoff has implications for the comparison of simulated and measured outflow, since the latter integrates subsurface and surface runoff. The quantification of surface flow is the matter of current research. Surface runoff measured in flumes will help to estimate the fraction of outflow attributed to surface runoff allowing a refined interpretation of simulated outflow.

3.4.2.4 Soil properties

Sandy soils exhibit large conductivity values for wet and small values for dry soil conditions, a hydraulic function represented by the free water capacity threshold separating conductive and non-conductive model cells. This characteristic behaviour of sand accounts much for the threshold-like process of drainage pathway connection and the nonlinear runoff response of the catchment. However, other soil physical variables than the free water capacity threshold may also lead to the threshold behaviour of flow path connectivity. Groundwater dynamics, the distribution of soil moisture in the vadose zone or the upcoming vegetation likely affect flow path connectivity. The extensive monitoring currently realised in the Chicken Creek catchment will provide a manifold of data, allowing the further investigation of processes and mechanisms related to flow path connectivity.

We assumed that soil texture properties in the range of the 316 measured samples are randomly distributed within the catchment. However, in fact the texture properties of the Chicken Creek catchment do not follow a random distribution. The clay and silt fraction of the soil on the western part of the catchment is slightly higher, especially for soil depths smaller than 0.3 m. This can be explained by the construction procedure of the man-made catchment. Sand was dumped first on the eastern and later on the western part of the catchment. The parent material used for the western part was slightly richer in clay and silt causing the difference in texture. Subsequent levelling of the catchment led to a mixing of the two parent materials at the surface, so that the effect of different texture between the eastern and the western catchment part is less obvious in shallow soil depths. The spatial trend in soil texture can be integrated in the model by using two different texture distributions, one accounting for the finer texture of the western catchment part and the other accounting for the coarser texture of the eastern part. We believe that the implementation of two different distributions would further promote the establishment of subsurface flow paths on the eastern part, as the free water capacity threshold decreases with increasing pore size and sand fraction of a soil. This means that for the same water content in the catchment more cells with drainable water are present on the eastern side (characterised by a generally coarser texture), increasing the probability of the formation of a draining cluster.

3.5 Conclusions

The emphasis of Chapter 3 was to quantify the role of hydrologic connectivity on subsurface flow in the man-made catchment Chicken Creek. Using Percolation Theory we simulated the drainage flow paths focussing on effects of catchment geometry (soil depth, slope gradient and clay layer microtopography) and spatial distribution of soil physical properties. The hydraulic function of the sandy material was simplified by introducing a water content threshold separating between conductive and non-conductive hillslope elements. The catchment geometry and the water content threshold were related to flow path connectivity and catchment outflow. The percolation model achieved to realistically represent the subsurface flow paths, which were indicated by soil moisture measurements and visual observations in the catchment. It has been shown that the establishment of a subsurface flow path network to the catchment outflow is a threshold-like process depending on the spatial distribution of conductive elements. This threshold-like behaviour of flow paths connectivity accounts for the sudden availability of a large amount of drainable water, which explains the nonlinear behaviour of runoff observed in the Chicken Creek catchment.

4 The emergence of surface erosion rills

4.1 Motivation

Erosion on bare soil caused by concentrated ephemeral surface runoff leads to the formation of erosion rills with depths in the order of several centimetres (Soil Science Society of America, 2008). Many studies have shown the hydraulic and soil hydraulic characteristics in such surface erosion rills to be considerably different compared to interrill areas (the reader is referred to the reviews by Knapen et al. (2007) and Gumiere et al. (2009) for a general description of rill and interrill erosion). Slattery and Bryan (1992) and Brunton and Bryan (2000) investigated a selection of hydraulic parameters, such as runoff, Reynolds number (ratio of inertial to viscous forces), and shear velocity in laboratory flume experiments and documented significant changes of the parameters with channel incision and tributary development. Poesen (1984) and Bryan and Poesen (1989) observed higher infiltration rates in rills than on interrill areas. This was confirmed by recent studies showing that saturated hydraulic conductivities in rills on two non-vegetated mining dumps were 5 – 43 times higher than on interrill areas (Biemelt et al., 2005; Gerwin et al., 2009b). Higher infiltration rates in rills cause a reduction of downstream channel discharge (Bryan and Poesen, 1989). Where rills incise down to the capillary fringe of a shallow groundwater table, hydraulic conditions in the rills are determined by seepage water significantly increasing soil erodibility (Huang et al., 2001), hence inducing a positive feedback between rill incision and runoff. Furthermore, the incision of rills alters the local hydraulic gradients and promotes lateral flow from adjacent areas towards the rills.

Because of the hydrological importance of surface erosion rills, a reasonable representation of the rill network is mandatory when modelling water percolation and runoff at the catchment scale. Thus, a model simulating the hydrology of a catchment prone to erosion rill formation ideally should consider (i) the location of rills, (ii) the geometric features of rills such as rill depth, (iii) rill evolution with time, and (iv) the appropriate scale (catchment scale) to account for the entire contributing area. However, most erosion models developed in the last years cannot satisfy all of these requirements. Rill characteristics, such as rill spacing, rill geometries or the location of rills often have to be specified a priori (e.g. Parsons et al., 1997; Ascough et al., 1997; Desmet and Govers, 1997), indicating that these models are static and only applicable to surfaces on which rills are already present. Conversely, dynamic rill evolution models are limited by their dependence on initial conditions of microtopography. Although, some models allow erosion rills to grow in width and depth, the initiation and development, especially the lengthways extension of rills, is poorly modelled when compared to observed rill networks (Favis-Mortlock, 1998; Favis-Mortlock et al., 2000). Studies based on models accounting for the dynamic lengthways growth of drainage networks often investigate the evolution of virtual catchments. Here, the comparison of the simulated drainage networks with real networks is done only in terms of statistical means (Kramer and Marder, 1992; Leheny and Nagel, 1993; Rinaldo et al., 1993; Simpson and Schlunegger, 2003). There are surprisingly few studies, where erosion rills have been mapped and compared to simulated rill networks with observed erosion patterns (Jetten et al., 2003).

A further problem of current erosion models is the lack of accounting for changing microtopography caused by erosion and deposition processes (Zobeck and Onstad, 1987; Nearing et al., 1997; Planchon et al., 2000; Planchon and Mouche, 2010) and related alteration of surface flow paths during a rainfall event (Favis-Mortlock et al., 2000). As a realistic representation of the surface flow network is a prerequisite for modelling reasonable erosion patterns (Jetten et al., 1999; Takken et al., 2001) dynamic surface flow paths and the dynamic representation of erosion and deposition processes should be taken into account. Most research dealing with soil erosion by water has concentrated on erosion processes operating at the plot scale or is based on laboratory studies carried out in small flumes limiting the full development of the rill network (Slattery and Bryan, 1992; Papanicolaou et al., 2010). Only relatively few studies have been conducted on rill erosion operating at larger spatial scales (Poesen et al., 2003; Chaplot et al., 2005).

In this chapter we aim to overcome these shortcomings of existing models. We developed and tested a model that predicts the spatial location of rills and simulates the dynamics of rill growth. The model is based on the self-organised critical network model presented by Rinaldo et al. (1993). Additionally, a second model was developed in order to compare the results of the self-organised critical network approach with results from a simple but more physically-based model approach. The second model was based on the computation of particle transport as function of flow velocity determined by the Manning equation. In Section 2.4.3, it was shown that the major part of the rill network formed in the first year of ecosystem development (October 2005 – September 2006) and afterwards evolved only marginally. Therefore, the study was confined to the rill network evolution of this initial period. The models were validated against rill patterns observed from aerial images and measured rill depths (Section 2.4.3). The observed rill network will be further referred to as the 'measured' rill network. The research questions addressed in Chapter 4 are:

- Are the models able to predict the location of evolving surface erosion rills in the Chicken Creek catchment?
- What are the factors controlling the development of surface rills in a new developing ecosystem?
- Does the rill network extension converge to a steady state?
- How do the surface flow paths change with developing erosion rills?

In Section 4.2 the two model approaches are explained. In Sections 4.3 and 4.4 model results are presented and discussed and the conclusion is presented Section 4.5.

4.2 Model description and methods

The objective of this study is to explore if various characteristics of a measured rill network can be represented by model approaches. For the evaluation of the model simulations the length of the rill network detectable in the air-borne images and the rill depth measurements derived from the laser scanning are available. However, we must be aware that the 'true' structure of the erosion network including complete depth information and location of small rills too shallow to be revealed by airborne imaging is unknown. This uncertainty is a challenge for the comparison between measured and modelled erosion rill networks. For that reason we made two different types of analysis: (1) We compared geometric characteristics of modelled and measured erosion rills like depth, position, length and spatial density of the rills. Simulated rill depths were compared with the laser scanning measurements. A rill was selected from a laser scanning transect if it was detectable on the aerial image and if both of the models also simulated the rill. The resulting 18 points of rill depth comparison are displayed in Figure 2.2a. The difference between the DEM 2008 and the DEM 2005 was used to infer the maximum rill depth in the catchment. We are aware that rill depths obtained from the laser scanning in 2008 and from the DEM 2008 may be larger than at the acquisition date of the aerial image (September 2006). However, since rilling activity decreased after 2006 and based on field inspections and photographs from 2006 the rill depths measured in 2008 are considered to be comparable to the rill depths in 2006. (2) In addition, we investigated if the modelled flow network matches the rill-network deduced from airborne images. Based on the assumption that deep rills occur where surface flow is the most erosive, we hypothesise that the imaged rills correspond to large flow paths and that the measured rill network can be used as a surrogate of the 'true' flow field. This assumption seems reasonable, especially for the footslope, where most of the single segments of the surface flow network are supposed to have enough energy to produce erosion rills due to the steeper slope and the higher contributing area. On the backslope the congruence between the rill network and the 'true' flow field is expected to be less pronounced since the erosive power of surface flow is limited due to flatter slopes and smaller contributing areas.

Two different model approaches were used to simulate the emergence of rill networks in the Chicken Creek catchment. They are presented in Section 4.2.1 and 4.2.2, respectively. A short sensitivity analysis of the free parameters of the models is included in the discussion. The spatial domain of both models is the DEM of the smooth catchment (no rills) imaged in 2005 divided into 53 519 cells with a resolution of 1 m. The overall shape of the catchment generally assures that each model cell has a defined surface flow direction and is connected to the lake or the catchment boundary following a strictly decreasing path. Artefact depressions resulting from the DEM generation procedure were removed using an algorithm developed by Planchon and Darboux (2001). The neighbourhood of a centre cell i is defined by the eight cells surrounding i (Moore neighbourhood). Four neighbours are located in the orthogonal direction at distance 1 m and four neighbours are situated in the diagonal direction at distance $\sqrt{2}$ m.

4.2.1 Self-organised critical network (SOCN) model

The first approach is an adaptation of the self-organising critical network (SOCN) model proposed by Rinaldo et al. (1993) based on the principle of minimum energy dissipation in the network (Rodríguez-Iturbe et al., 1992). The resulting cell elevations and branching patterns are determined by the application of this global optimisation principle (Rodríguez-Iturbe et al., 1992). The authors used the model to compare fractal and multifractal network statistics of randomly generated virtual DEMs with optimal channel networks and with characteristics of naturally evolved large-scale river networks (Rinaldo et al., 1993; Rodríguez-Iturbe et al., 1994). We applied the model to the surface of the Chicken Creek Catchment in order to investigate the evolving erosion rill network at the hillslope scale. As explained in more detail in the next paragraph, the original model was adapted to handle physically based threshold values required in erosion modelling and to describe particle deposition.

4.2.1.1 Representation of the surface flow paths

For the SOCN model the surface flow pattern is represented by the contributing area. Rodríguez-Iturbe et al. (1992) have shown that the mean annual surface discharge from a cell i, $Q_{m,i}$, is proportional to the contributing area A_i, which is defined as the areal sum of all cells eventually draining through cell i. The surface flow direction from a cell i was computed in the direction of steepest slope σ_i between cell i and its neighbourhood. This method is commonly known as the deterministic eight-neighbours (D8) algorithm (O'Callaghan and Mark, 1984; Fairfield and Leymarie, 1991). If there is the same steepest slope between cell i and more than one neighbour, the surface flow direction is chosen randomly towards one of these neighbours.

4.2.1.2 Erosion and deposition

Shear stress τ is one of the key quantities guiding the erosion process (Torri et al., 1987). For flow in dynamic equilibrium shear stress is quantified as product of fluid density ρ_f, gravitational acceleration g, slope σ, and flow depth d_f:

$$\tau = \rho_f g \sigma d_f \tag{4.1}$$

Erosion occurs if a critical shear stress threshold τ_{ce} is exceeded. Shear stress is largely determined by surface runoff Q_m. Justified by experimental evidence and by optimality principles surface runoff is assumed to scale with flow depth as $d_f \propto Q_m^{0.5}$ (Rodríguez-Iturbe et al., 1992; Rodríguez-Iturbe and Rinaldo, 1997). Therefore, at a given grid cell i the shear stress τ_i is proportional to $Q_{m,i}^{0.5}\sigma_i$. Surface runoff in turn is proportional to the contributing area A_i. Thus, following Rodríguez-Iturbe and Rinaldo (1997) and setting the coefficient of proportionality ε to $1\,\mathrm{kg\,m^{-3}\,s^{-2}}$, τ_i can be estimated as:

$$\tau_i = \varepsilon A_i^{0.5} \sigma_i \tag{4.2}$$

The critical shear stress for erosion τ_{ce} was determined following (Alberts et al., 1995), who defined it for cropland surface soils containing 30 % or more sand as

$$\tau_{ce} = u_1 + u_2 c - u_3 s_{vf} \tag{4.3}$$

where u_1, u_2, and u_3 are empirically derived parameters ($u_1 = 2.67\,\mathrm{kg\,m^{-1}\,s^{-2}}$, $u_2 = 6.5\,\mathrm{kg\,m^{-1}\,s^{-2}}$, $u_3 = 5.8\,\mathrm{kg\,m^{-1}\,s^{-2}}$), and c and s_{vf} are the fractions of clay and very fine sand (0.05 mm – 0.1 mm), respectively. For $s_{vf} < 0.40$ the authors recommend to use $s_{vf} = 0.40$ in Equation (4.3). Using the averages of the clay and fine sand texture measurements from the Chicken Creek catchment, a threshold value τ_{ce} of $0.81\,\mathrm{N\,m^{-2}}$ is assigned to all grid cells. This value is in agreement with values for sand surfaces reported in other studies (Mitchener and Torfs, 1996; de Linares and Belleudy, 2007). We also chose $0.81\,\mathrm{N\,m^{-2}}$ for the critical shear stress for deposition τ_{cd} implying that deposition activities in the catchment only take place for $\tau < \tau_{cd}$. Model simulations with $\tau_{ce} \neq \tau_{cd}$ were also conducted and are discussed in Section 4.4.4.1. For each cell i the shear stress is calculated based on Equation (4.3). Between the cells with shear stress exceeding the critical value for erosion ($\tau > \tau_{ce}$) the cell with maximum exceedance is determined and its elevation is decreased by the value of the erosion parameter d_e. Because erosion rills of maximum depth of about 1 m were generated during about 120 days of rainfall (Section 4.2.2), we set $d_e = 0.01\,\mathrm{m}$ (effect of other values will be discussed in Section 4.4.4.1). For all cells where erosion takes place the threshold is increased by 4 % to account for soil erodibility decreasing with increased soil bulk density in higher soil depth (Bradford and Grossman, 1982; Mouzai and Bouhadef, 2011; Amos et al., 1992) . After erosion at the cell with maximum exceedance, the contributing area for all cells is recomputed to account for the modified surface topography. Downslope of the eroded cell, material is deposited at the nearest cell with $\tau < \tau_{cd}$. The amount of deposited material d_d was calculated as $d_d = (\tau_{cd} - \tau) \,/\, (\tau_{cd})\, d_e$. For $0 < \tau < \tau_{cd}$ material is left for deposition and will be deposited at the next cell with $\tau < \tau_{cd}$ in downslope direction. As soon as all eroded material is deposited, the contributing area of all cells is recomputed to account for topography modified by deposition. Erosion and deposition is repeated until a steady state with $\tau < \tau_{ce}$ is reached for all cells. It should be emphasised here that time and precipitation are not represented explicitly in the SOCN model.

Shear stress at a model cell is based on mean flow conditions deviated from the cell's contributing area. Thus, a single iteration step during the simulation cannot be related to time in terms of days, hours or seconds.

The simulation algorithm of the SOCN model is summarised in the flow chart shown in Figure 4.1.

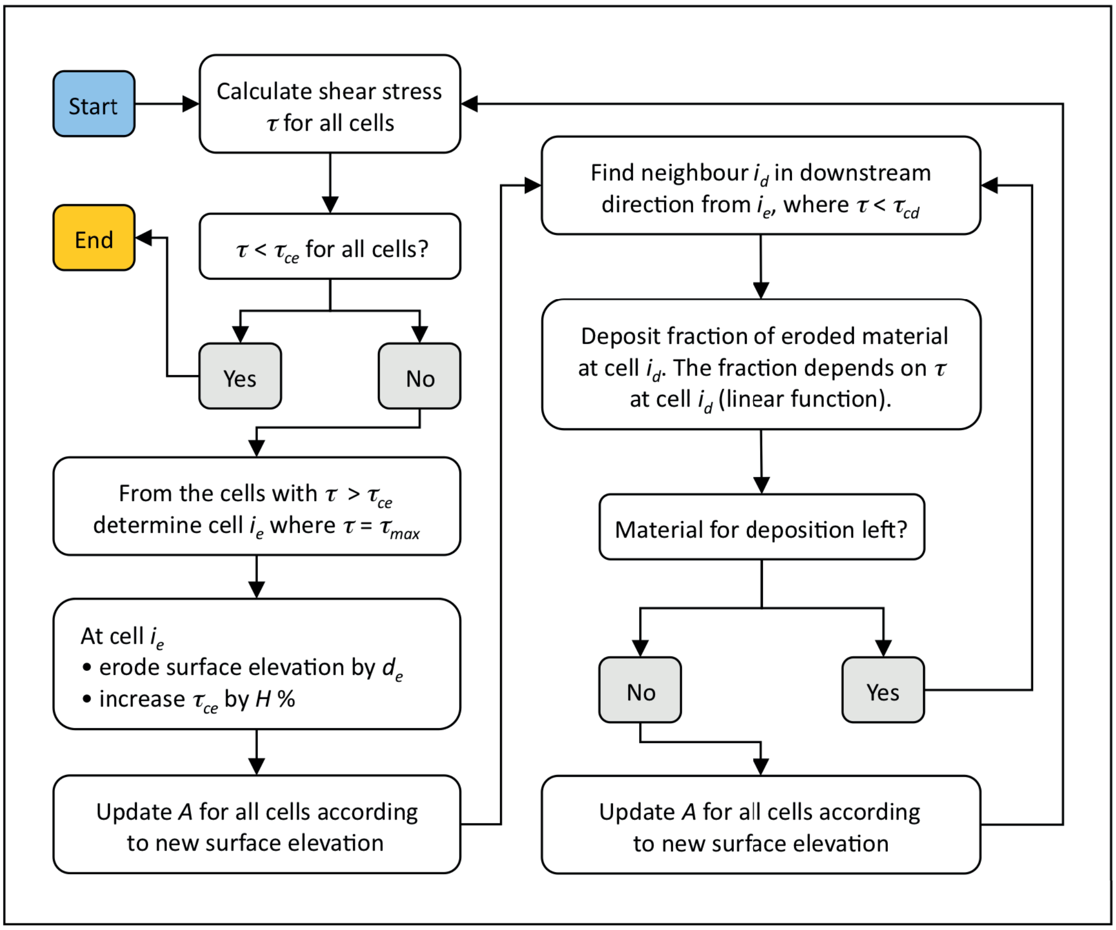

Figure 4.1: Flow chart of the self-organised critical network (SOCN) model where τ_{ce} is the critical shear stress for erosion, τ_{cd} is the critical shear stress for deposition, H is the erodibility factor, d_e is the erosion parameter, A is the contributing area, and i_e and i_d are cells where erosion or deposition occur. The loop stops when all cells are exposed to shear stress below the critical value.

4.2.1.3 Delineating the surface flow network

Later on we will compare modelled and measured flow and rill networks. To determine the surface flow network for the SOCN approach we neglected cells with contributing area smaller than a threshold value A_{crit} (Gómez et al., 2003). The threshold value was chosen according to the density δ_f of the surface flow network and based on the assumption that on the footslope the measured rill network corresponds well with the surface flow field. The density δ_f was defined as the ratio between the total length of the surface flow paths on the footslope L_f and the catchment area of the footslope A_f. Firstly, we calculated the density of the measured rill network for the footslope. Thereafter, we computed the modelled flow path density for increasing values of A_{crit} until the measured rill density and the modelled flow path density for the footslope were identical (for $A_{crit} = 35\,\mathrm{m}^2$). All cells with contributing area smaller than A_{crit} were not taken into account for the flow network.

4.2.2 Manning-based (MB) model

The Manning-based (MB) model accounts for depth and velocity of the ephemeral surface runoff. For that purpose we have to interpret rainfall data from the Chicken Creek catchment in terms of height and volume of available water at the surface. Rainfall dynamics in the temporal resolution of a few minutes or even seconds would be necessary to exactly describe the dynamics of surface runoff. Unfortunately, such high resolution rainfall data were not available. In the model we use a constant rainfall intensity, although we know that this reduces the dynamics of surface runoff in the catchment. However, we argue that mainly rill deepening is affected by the damping of surface runoff dynamics. The location of the flow paths, as well as the position, lengthwise extension and spatial density of the main rill network are less affected. Additionally, using a constant rainfall intensity allows a better comparison with the SOCN model, which is based on mean runoff derived from the contributing area. The rainfall intensity used in the model was determined as follows: For the time series October 2005 – September 2006 twelve intense rainfall events with a total of 324 mm of rainfall could be distinguished.

Rainfall events were separated from each other based on the criterion of minimum four days without rainfall between the events. As shown in Section 2.4.1 more than a total of 9 mm of rainfall per event is needed to generate runoff. We assign these 9 mm to soil sorptivity and subtract its amount from the cumulated total rainfall amount of each event. The remaining rainfall (216 mm) is equally divided between all the days of the twelve events with rainfall larger than zero ($T = 120$ days) resulting in the rainfall intensity of 1.8 mm per day.

4.2.2.1 Modelling surface water flow

The flow chart of the MB model (Figure 4.2) gives an overview of the algorithm described in detail in the next two sections. Precipitation of 1.8 mm is added to each grid cell as rainfall excess. Surface water flow is driven by the elevation difference between surface water levels of neighbouring cells. For each grid cell with surface water the flow velocity v was calculated based on the empirical Manning equation:

$$v = \frac{\chi}{m} d_f^{2/3} \sigma_w^{1/2} \tag{4.4}$$

with hydraulic radius estimated as water depth d_f (Parsons and Fonstad, 2007), downslope gradient of water level σ_w, roughness coefficient m, and dimension conversion factor $\chi = 1\,\mathrm{m}^{1/3}\,\mathrm{s}^{-1}$. Water depth d_f is determined from rainfall input and from eventual lateral surface input calculated by Equation (4.6). The slope σ_w is defined by the difference in surface water level and the distance l between the centroids of adjacent neighbours, that is 1 m in orthogonal and $\sqrt{2}$ m in diagonal direction. As in the case of the SOCN approach, water is flowing only in the direction of the maximum gradient. A low value (0.03) was chosen for m to represent the unvegetated and rather smooth sandy surface (Dingman, 2008). Although widely used in erosion models the application of the Manning equation to describe rill flow was criticised (Govers et al., 2007). Giménez and Govers (2001) and Giménez et al. (2004) noticed that flow velocities in rills tend to be independent of slope due to a feedback between rill bed morphology and flow conditions. Thus, for models using a static topography the assumption of a constant hydraulic

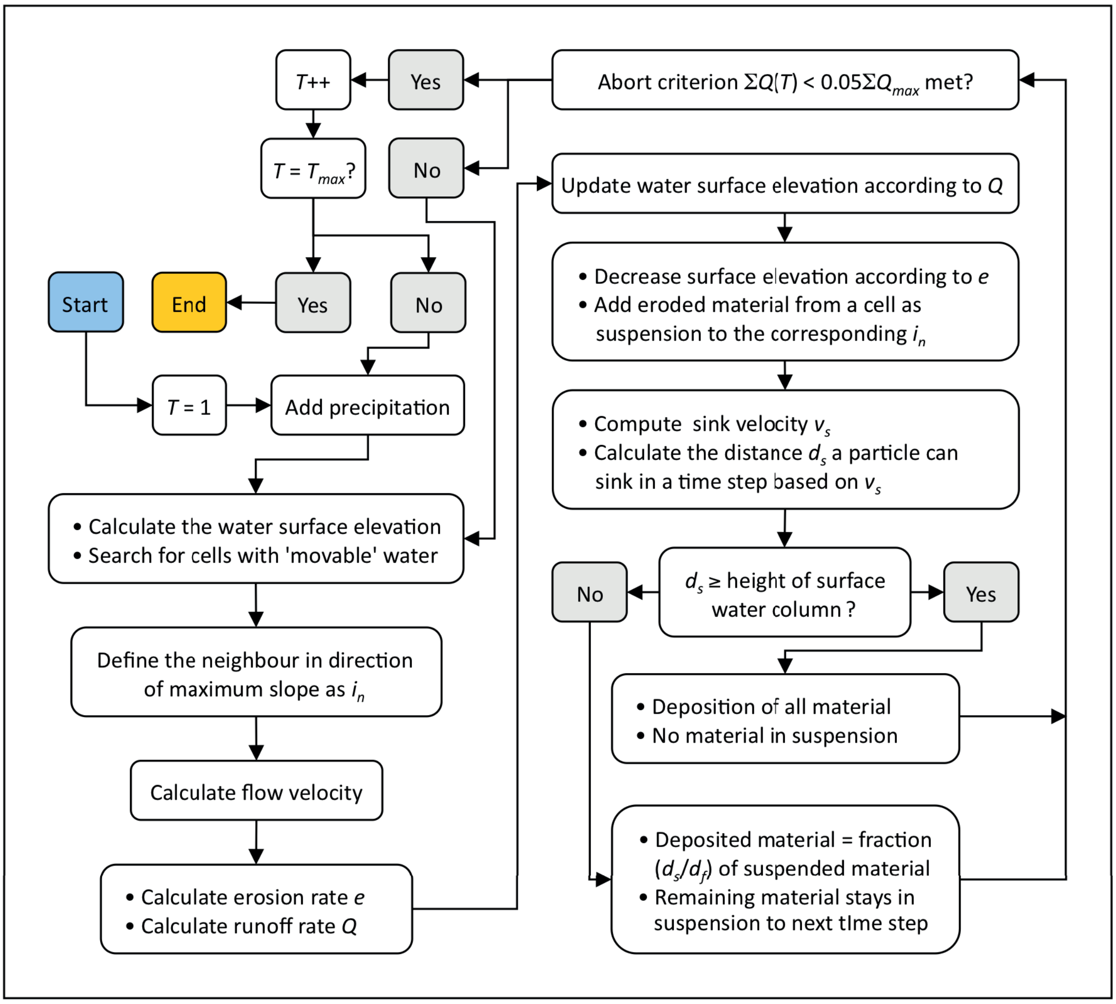

Figure 4.2: Flow chart of the Manning-based (MB) model. T is the number of days with rainfall. T_{max} is 120 and represents the last day at which precipitation (1.8 mm) is added as source term.

roughness m in the Manning equation was considered inappropriate when simulating eroding rills (Govers et al., 2007). However, the use of a constant m in the MB model was justified by the description of a dynamic surface topography during a model simulation. Since slopes are gradually adapted according to the erosive power of the surface flow (Section 4.2.2.2) the feedback between rill bed morphology and flow conditions is considered.

In the case of ponding the velocity of water flow on the equalising water table is described with a wave velocity formula (Garrison, 2009):

$$v = \sqrt{g d_f} \tag{4.5}$$

where g is gravitational acceleration. Within each time step t the water volume V flowing in downslope direction is:

$$V = Q_{surf} t = d_f s_{oct} v t \tag{4.6}$$

with surface runoff Q_{surf} and the width of the stream between two cells determined as side length of an octagon s_{oct} with the same area as the grid cell ($1\,\mathrm{m}^2$). The model time step t was determined based on the condition that a water volume cannot be transported beyond the length l (corresponding to the distance between cells) and is thus limited by the maximum flow velocity v_{max} in the system:

$$t = \frac{l}{v_{max}} \quad \text{for } v_{max} > 0 \tag{4.7}$$

In the course of time, surface water is redistributed in downslope direction towards the lake and the volume of surface water in upslope direction is decreasing. Because according to Equation (4.4) velocity approaches zero for small water depths d_f, we stopped water redistribution when the cumulated surface flow of all cells dropped to less than 5 % of the initial value after adding 1.8 mm water. When this criterion was fulfilled the next portion of 1.8 mm water was added to each cell. The simulation stopped after 120 precipitation events, each contributing 1.8 mm, were distributed.

4.2.2.2 Erosion and deposition

By using a constant average rainfall intensity surface runoff peaks will be damped and runoff is assumed to be comparable to mean runoff. The erosion rate e was calculated as a threshold dependent function based on shear stress τ (Equation (4.1)). The shear stress τ is a function of slope and flow depth and is related to the dimensionless Shields number τ^* (Shields, 1936) in the following way

$$\tau^* = \frac{\tau}{g\left(\rho_s - \rho_f\right) d_p} \tag{4.8}$$

where ρ_s is the density of sediment particles (here $2650\,\mathrm{kg\,m^{-3}}$) and d_p is the mean particle diameter (0.4 mm in our case). The Shields number is used to compute the dimensionless bedload transport (Meyer-Peter and Müller, 1948):

$$\Phi^* = 8\left(\tau^* - \tau^*_{ce}\right)^{3/2} \quad \text{for } \tau^* > \tau^*_{ce} \tag{4.9}$$

τ^*_{ce} is the dimensionless critical shear stress for erosion and was empirically derived by Parker (1979) as 0.03. Einstein (1950) related the dimensionless bedload transport to the volumetric sediment discharge per unit channel width q_{sed}:

$$q_{sed} = \Phi^* d_p \left(\left(\frac{\rho_s}{\rho_f} - 1\right) g d_p\right)^{1/2} \tag{4.10}$$

Volumetric sediment discharge Q_{sed} is then calculated as

$$Q_{sed} = q_{sed} b \tag{4.11}$$

with b corresponding to the channel width (length of a grid cell). Finally, the erosion rate e is computed as

$$e = \frac{Q_{sed}}{a} \tag{4.12}$$

with a being the area of a model cell.

The eroded material at a time step t is transferred in suspension to the downstream cell. The suspended sediment is equally distributed along a vertical profile in the water column. Deposition was calculated according to Stokes' formula:

$$v_s = \frac{2r^2 g\left(\rho_s - \rho_f\right)}{9\eta} \tag{4.13}$$

with sediment velocity v_s of grains with particle radius r, sediment density ρ_s (here $2650\,\mathrm{kg\,m^{-3}}$) and dynamic fluid viscosity η ($0.001\,\mathrm{kg\,s^{-1}\,m^{-1}}$ for water at 20 °C). Because medium and fine sand fractions are the dominant soil texture classes in the catchment we used $r = 0.2\,\mathrm{mm}$ as a representative value for the particle size. The sink velocity determines the maximum change of height d_s of a particle in its settling movement during the time step. The amount of deposited sediment in time step t is the fraction d_s/d_f with d_f being the height of surface water. For $d_s > d_f$ all suspended sediment is deposited.

4.2.2.3 Delineating the surface flow network

The procedure to delineate the flow network in the MB model is very similar to the one used in the SOCN approach. However, instead of using the critical contributing area, a threshold of total discharge from a cell was used in the MB model to decide whether a cell belongs to the flow network or not. The total discharge from each of the model cells was calculated by adding 120 times 1.8 mm of rainfall and successively letting the water flow off according to the model described above. As in case of the SOCN model, the threshold was iteratively increased until the measured rill network density and modelled flow network density on for footslope were identical. This was the case for the discharge threshold of $0.2\,\mathrm{m^3\,d^{-1}}$. All cells with lower discharge were considered not to be part of the flow network. The resulting binary image consisting of cells with flow above threshold was skeletonised according to the algorithm proposed by Vogel et al. (2005) to obtain the backbone of the predicted flow network, which was then compared to the flow network of the SOCN model and to the measured rill network.

4.2.2.4 Quantifying the surface flow network

To estimate the quality of the simulated surface flow networks we compared the simulations with the measured rill network of the Chicken Creek catchment. As explained at the beginning of Section 4.2, we assumed that the measured rill network is a first order estimate for the unknown ephemeral surface flow pattern of the Chicken Creek catchment. Two methods to validate the simulated surface flow networks were applied. Firstly, we used the Strahler order (Horton, 1945; Strahler, 1957), a numerical measure of the networks branching complexity. We compared the total length of the flow paths of individual Strahler orders normalised by the total length of flow paths for all orders. The surface flow path length corresponding to the different Strahler orders was compared with that of the measured rill network (as first order estimate for the flow network). As a prerequisite of this comparison, the Strahler orders of the different flow paths must be quantified. This is straightforward in case of the SOCN model where the flow network equals the contributing area that is characterised by a treelike structure without loops because each cell has just a single outlet. However, for the Manning approach and the measured rill network closed paths (loops) can occur in the network and we used the following procedure to determine Strahler order: At a bifurcation of a surface flow path in downslope direction, the main flow path is defined as the most direct path towards the lake. The less direct path is disconnected and is treated as individual tributary. The second method to validate the simulated surface flow networks is based on the relationship between flow path length ratios. For a cell i belonging to the flow path network the relative flow path length L_p is defined as L_i, the flow path length between the lake and i, divided by the maximum flow path length. The relative flow network length L_n is defined as the total flow network length of all individual flow paths up to the distance L_i divided by the total flow path network length. The relationship between the relative flow path length and the relative flow network length was used to compare the simulated flow path networks with the measured one.

4.2.2.5 Quantifying the rill network

The rill networks simulated with the SOCN and the MB model were compared with mesurements of total rill network length, rill density of the total catchment, the backslope and the footslope, and with rill depths. The ‘true’ maximum rill depth was estimated from the difference between the DEM of 2005 and the DEM of 2008. The simulated rill networks were also compared visually with the measured network in order to verify the location of the simulated rills.

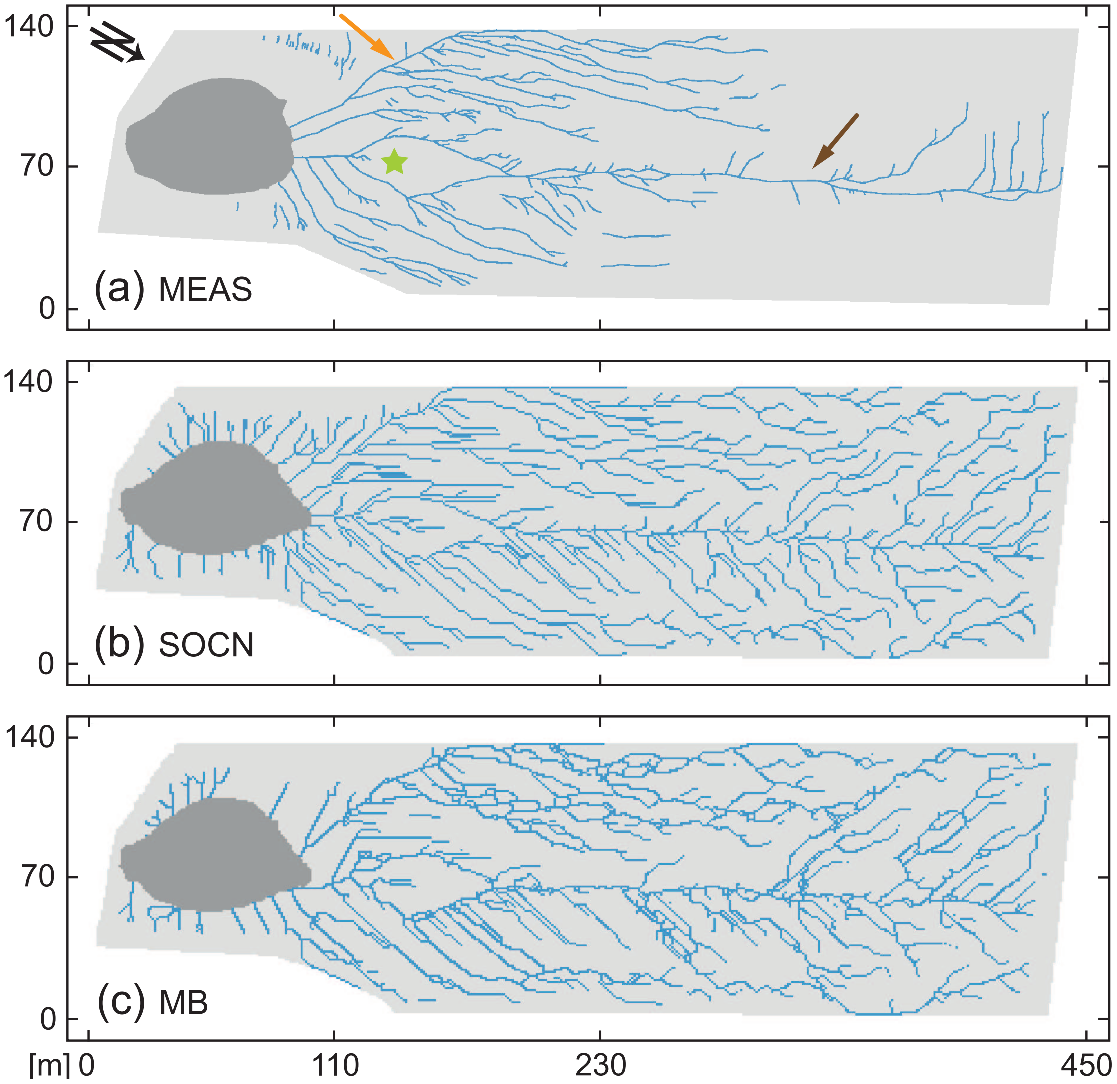

Figure 4.3: Comparison of (a) the measured erosion rill network, serving as first order estimate for the surface flow paths in the catchment and surface flow paths simulated by (b) the SOCN model and (c) the MB model, respectively. The dark brown arrow indicates the main rill emerging at the backslope and flowing around weir facility (green star). The western part of the catchment is not draining via main rill but by an independent rill network (orange arrow). These main characteristics are represented by the two model approaches.

4.3 Results

4.3.1 Surface flow networks

The measured rill network representing the surface flow paths of the Chicken Creek catchment and the simulated flow patterns of both models are displayed in Figure 4.3. The imaged flow network consists of two structures: a main drainage pathway emerging in the centre of the backslope that is entrained by smaller inflows on the footslope and an additional independent flow network in the western part of the catchment. The models match these main characteristics of the observed flow network.

Figure 4.4a shows the total length of flow paths of Strahler order ω normalised by the total surface flow network length on the y-axis and Strahler order on the x-axis. The values show the expected decay of flow path length with increasing Strahler number. The simulations are in good agreement with the measured rill network, although both models overestimated the length of flow paths of order 1. The MB model slightly underestimated all the lengths of flow paths of higher orders whereas for the SOCN model no trend of over- or underestimating flow path lengths of higher orders was observed. Since very fine rills in the catchment are not detectable on the aerial image, we expected the number of order 1 flow paths to be underestimated. Figure 4.4b displays the relationship between the relative flow path length L_p and the relative flow network length L_n. The figure quantifies the differences of the flow path networks shown in Figure 4.3. The increase of L_n with L_p is relatively constant for the two simulations. This is the result of a quite homogeneous distribution of flow paths in the catchment, which is confirmed by the visual inspection of Figure 2.5b and 2.5c. The increase of L_n with L_p is much less uniform for the measured flow paths and deviates from the simulations especially for $0.2 < L_p < 0.8$. The deviation can be explained by the difference of flow path density between the footslope and the backslope of the measured network, which is directly affecting the relative network length L_n.

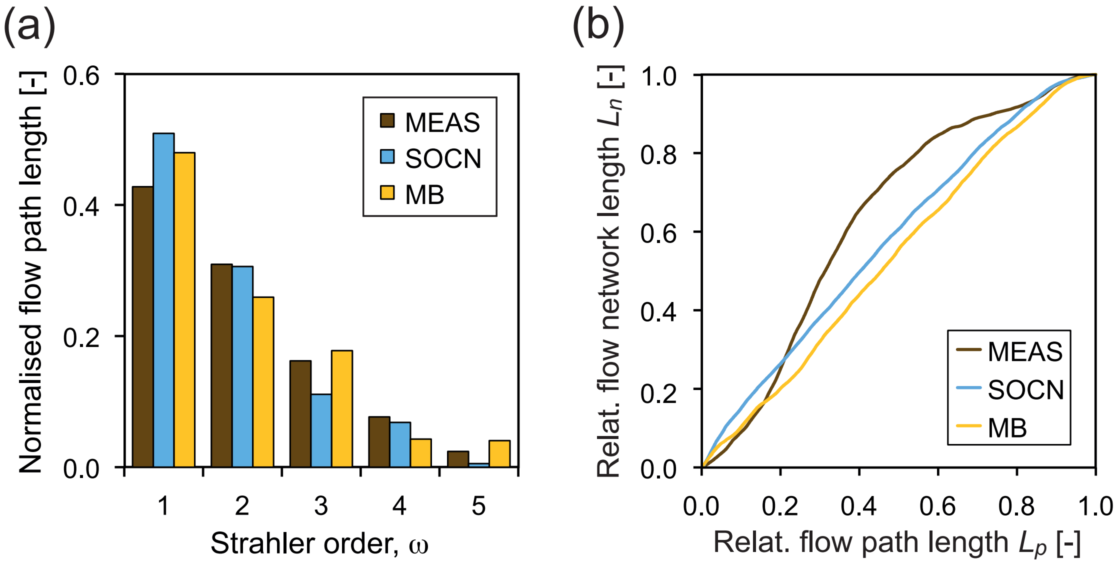

Figure 4.4: Quantification of simulated surface flow paths (SOCN model and MB model, respectively) and measured erosion rills (MEAS). (a) Total flow path length of a given Strahler order ω normalised by total flow path length. The topological relations of the simulated networks are in good agreement with the measured network. (b) Relationship between the relative flow path length L_p and the relative flow network length L_n. The homogeneous distribution of flow paths in the catchment for the two simulations is represented as uniform increase of L_n with L_p. The deviation of the curve representing the measurements is explained by the difference of the flow path density between the footslope and the backslope.

4.3.2 Rill networks

The rill network digitised from the aerial image taken in September 2006 is shown in Figure 4.5a. The main rills were annotated with a number. The total rill network length accounted for 4066 m, which results in a rill density of $0.09\,\mathrm{m}^{-1}$ for the entire catchment. Rill density on the footslope is about three times higher ($0.17\,\mathrm{m}^{-1}$) than on the backslope ($0.05\,\mathrm{m}^{-1}$).

The maximum measured rill depth is located in the erosion rill North from the weir and is a result of the combination of steep terrain and high flow depths in this area (Figure 4.5a). The measured rill depths derived from the laser scanning were between 0.07 m and 0.65 m (Table 4.1). Generally, two trends for the measured rill depths were observed. Rills on the footslope are deeper than rills on the backslope and rills besides the main middle rill are more shallow than the main rill.

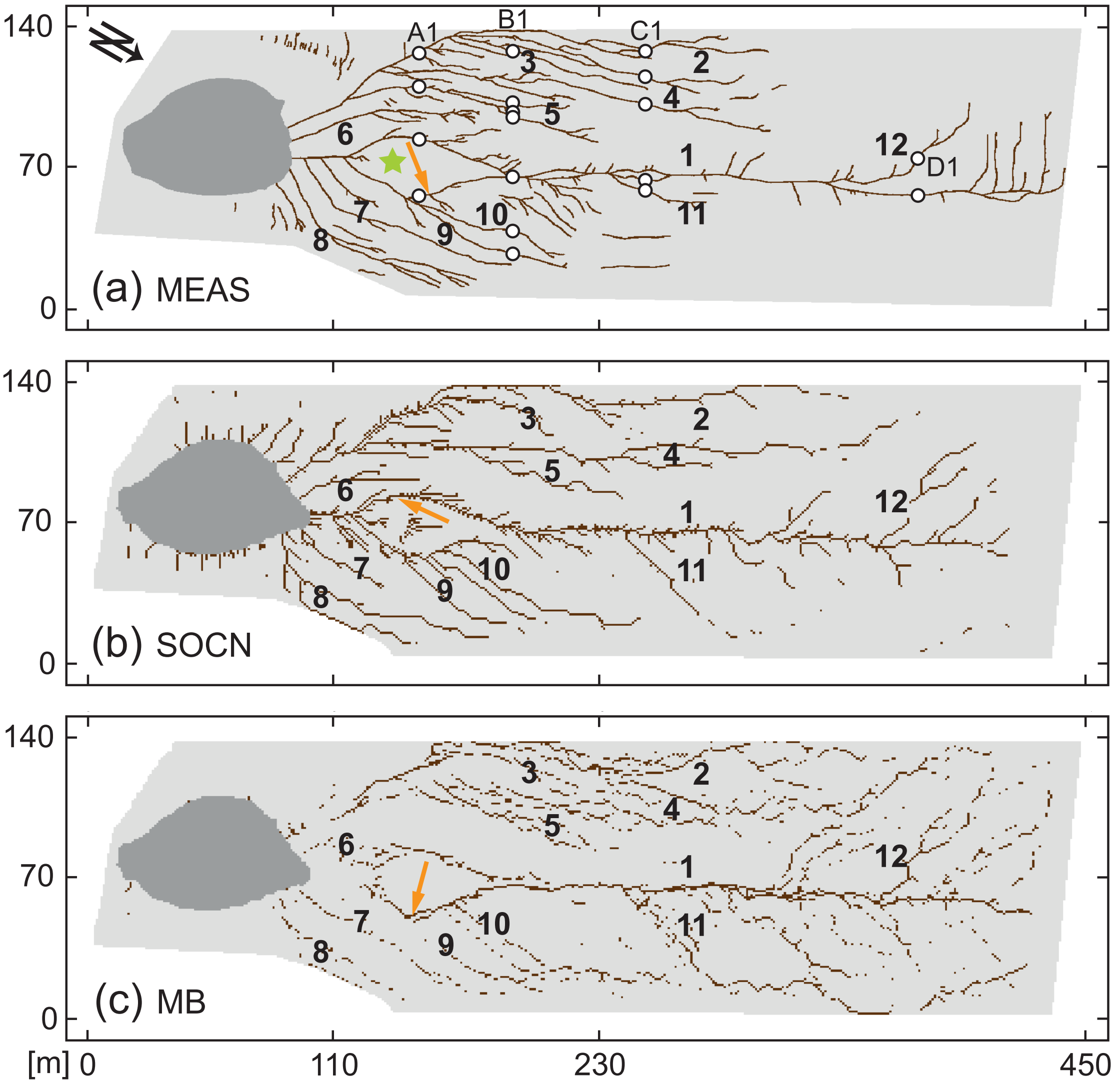

Figure 4.5: Comparison of (a) the measured rill network with (b) the rill network simulated with the SOCN model, and (c) the rill network simulated with the MB model, respectively. The numbers indicate the main rills developed in the first year. The main 12 erosion rills are represented by the models. In case of the Manning-based model approach the rill network is not continuous due to the high impact of deposition of material. The orange arrows indicate the location of maximum rill depth, which is measured and simulated near the weir (green star). The circles indicate the positions of the rill depth measurements obtained by laser scanning (A1 – D1 mark the first measurement position of transect A – D).

Position	**MEAS**	**SOCN**	**MB**
A1	0.28	0.42	0.15
A2	0.15	0.31	0.03
A3	**0.58**	**0.65**	**0.17**
A4	**0.65**	**0.31**	**0.53**
B1	0.23	0.30	0.01
B2	0.28	0.37	0.02
B3	0.11	0.03	0.06
B4	0.21	0.16	0.01
B5	**0.60**	**0.52**	**0.38**
B6	0.23	0.23	0.09
B7	0.26	0.03	0.01
C1	0.13	0.27	0.02
C2	0.10	0.21	0.03
C3	0.16	0.17	0.01
C4	**0.47**	**0.43**	**0.25**
C5	0.21	0.23	0.02
D1	0.07	0.05	0.07
D2	**0.22**	**0.10**	**0.10**
Max	0.81	0.77	0.89

Table 4.1: Comparison of measured (laser scanning) and simulated rill depths at the positions indicated in Figure 10a and 22a (A1 – D4). Values for the main middle rill are given in bold. Maximum rill depth (Max) was derived from the difference between the DEMs of 2008 and 2005. Simulated rill depths are in the right order of magnitude, especially for the SOCN model. The MB model generally underestimated the rill depth.

Visual comparison between the simulation of the SOCN model and the measurements of the individual rills showed that the main rills were captured well by the model (Figure 4.5a and 4.5b). Generally, the length extension of the rills is simulated realistically, although for some of the rills (#3 and #7) the simulated rill was too short. Simulated total rill length for the SOCN approach is 3365 m (83 % of the measured total network length). The modelled rill density for the entire catchment is 0.07 m^{-1} (78 % of measurements), whereas the backslope accounts for 0.04 m^{-1} (80 % of measurements) and the footslope for 0.11 m^{-1} (65 % of measurements), respectively. Average rill depth and maximum simulated rill depth are 0.18 m and 0.77 m (measured value 0.81 m), respectively. The SOCN model predicted the deepest rill segment in the western part of the weir (Figure 4.5b). Comparing the rill depth simulated by the SOCN model with the measured rill depths (Table 4.1) it became clear that the model was able to reproduce the correct magnitude of the rill depths. For the 18 selected points the model simulated rill depths between 0.05 and 0.65 m. Also the general characteristics of decreasing rill depth with increasing distance from the lake and large depths for the main rill and smaller depths for rills beside were well represented.

Comparing the results of the Manning approach with the measurements (Figure 4.5a and 4.5c), it could be seen that the locations of the main rills were simulated reasonably well. However, two main differences between measured and simulated rill network exist: First, the simulated rill network is not continuous, meaning that not every rill cell is connected with the lake. This is also apparent in the reduced total rill network length of only 2459 m (60 % of measured length). The reason for this is the strong erosion-deposition interplay for this modelling approach. It became especially evident in the lake-near part of the catchment, where simulated rills only formed scarcely, because deposition preponderated over erosion in this area. Because of the non-continuous network the allocation of an individual rill number was not always trivial (e.g. #3, #4 and #5). However, for most of the simulated rills the corresponding measured individual could be found. Second, the simulated rill density of the backslope was equal to the measured rill density (0.05 m^{-1}). This was in contrast to the visual impression of a higher backslope rill density for the simulation. However, the impression only occurred because the simulated rill cells did not form to a continuous structure and were distributed loosely on the backslope area. The low rill density on the footslope ($0.06\,\mathrm{m}^{-1}$) could also be explained by the non-continuous rill network leading to a shorter total rill length. As the location of the measured maximum rill depth, the MB model simulated the location of the deepest incision in the North of the weir (Figure 4.5c). Although the simulated maximum rill depth of 0.89 m was well in accordance with the measured value (0.81 m), the average rill depth for the Manning approach (0.07 m) was much smaller than for the SOCN approach. This was also visible from three-dimensional plots of the simulated rills (Figure 4.6) and from the comparison of rill depths between laser scanning measurements and simulation (Table 4.1). Although the range of simulated rill depth was reasonable (0.01 m – 0.53 m) rills were generally simulated too shallow. However, the trend of shallower rills besides the main middle rill was reproduced and the rill depths for the main rill are in the right order of magnitude. The characteristic decrease of rill depths with increasing distance from the lake is less obvious than for the SOCN model and for the measurements.

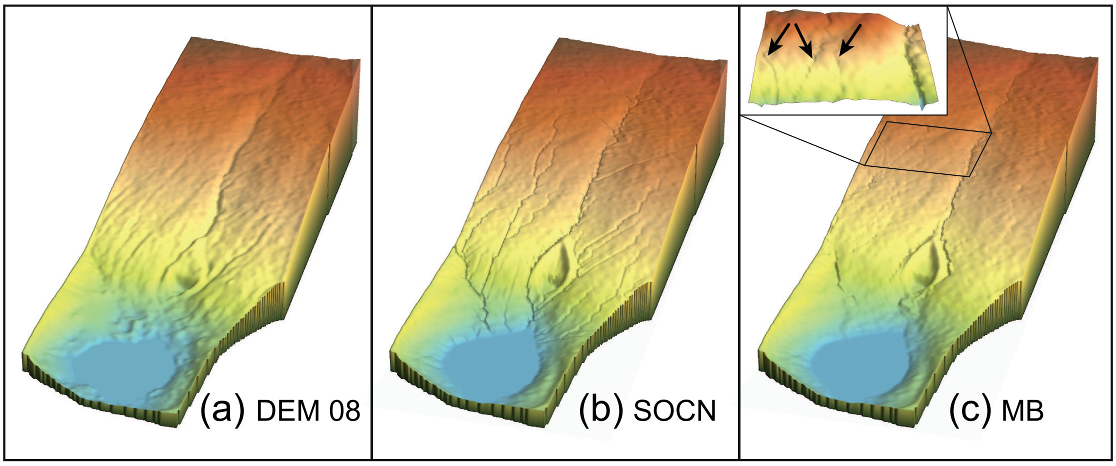

Figure 4.6: Three-dimensional plots (vertical scale-up 5× of the rill network (a) derived from the DEM 2008, (b) simulated with the SOCN model and (c) simulated with the MB model. The visual comparison reveals that the average rill depth simulated with the SOCN model is in good agreement with the average rill depth observed in the catchment. The average rill depth simulated with the MB model apparently is underestimated and is, apart from the major middle rill, difficult to identify at this scale. The inset in (c) displays a detail view of the MB simulation (vertical scale-up 10×) in which also smaller rills are shown (indicated by arrows).

4.3.3 Simulated rill network evolution

Figure 4.7 shows different snapshots in the evolution of the rill network for both models. In the MB model an evolution step corresponds to the addition and run-off of 1.8 mm of precipitation, whereas in the SOCN model a step represents an iteration in which the elevation for the cell with maximum critical shear stress ex-

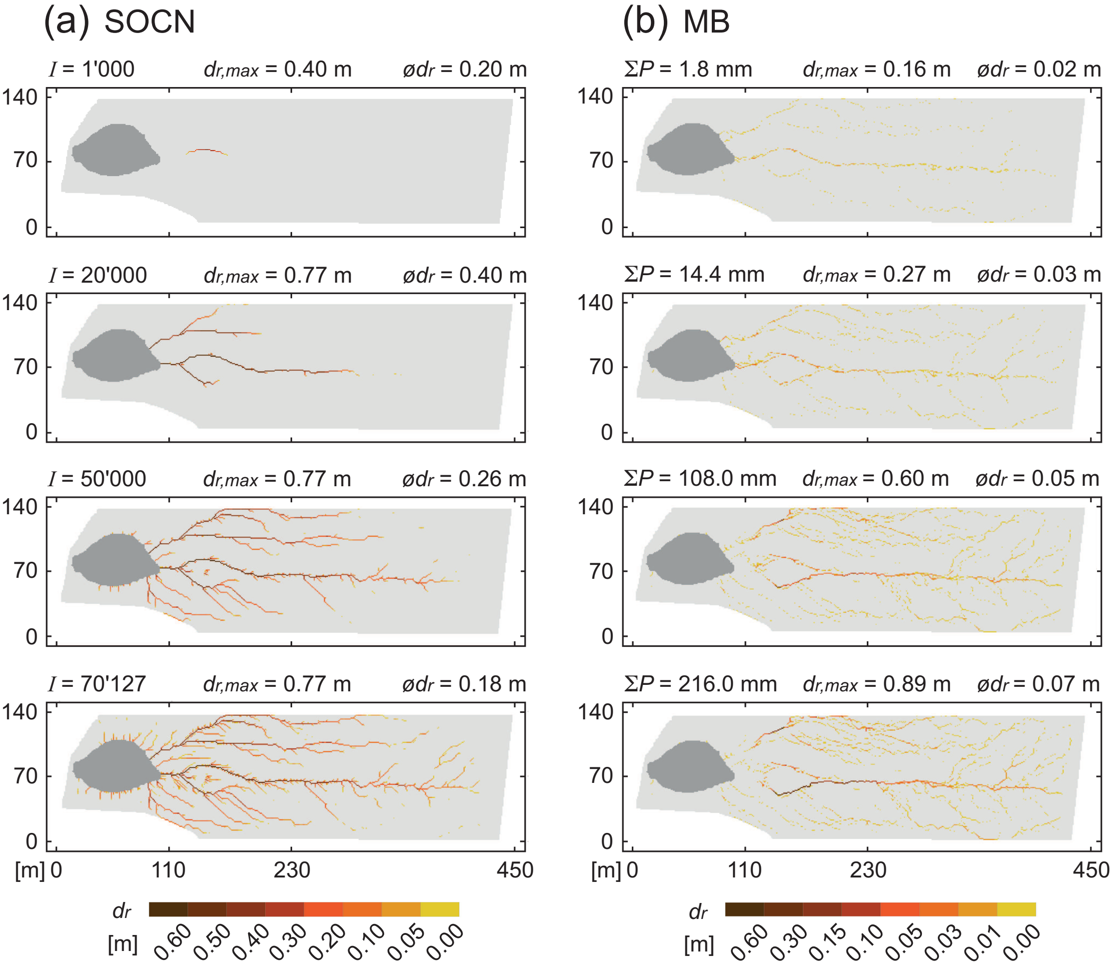

Figure 4.7: Simulated network evolution starting from an unrilled state, where I is the iteration step, P is precipitation, $d_{r,max}$ is maximum rill depth and $\varnothing d_r$ is average rill depth. (a) Results of the SOCN model. The network in the SOCN model evolves until reaching a steady state, i.e. until $\tau < \tau_{ce}$ for all model sites (at $I = 70\,127$). (b) Results of the MB model. For the MB model the final state is reached after the application of 120 times 1.8 mm rainfall (at $\sum P = 216\,\text{mm}$). Note the difference and the nonlinearity of the rill depth scales.

ceedance was decreased. For the SOCN model the maximum rill depth developed rather quickly when the network was only short resulting in a high average rill depth. Network length increased and average depth decreased with proceeding iterations until a steady state ($\tau < \tau_{ce}$ for all cells) was reached. The increasing erosive power in deepening rills (due to steeper slopes and larger contributing areas) was gradually reduced according to the model rule accounting for the consolidation of soil with depth.

The network evolution for the MB model was quite different. The extent of the network established relatively quickly after adding about 20 times the rainfall amount of 1.8 mm. However, maximum rill depth gradually increased with increasing rainfall amount, and so did average rill depth, until the end of the simulation when the total of 216 mm of rainfall had been added.

4.3.4 Change of surface flow patterns

The change of surface flow patterns due to erosion rill development was assessed by comparing the contributing areas of the original surface (DEM of 2005) with the contributing areas of the simulated evolved DEMs, i.e. after reaching a steady state for the SOCN simulation and after adding 120 times 1.8 mm of rainfall for the MB simulation, respectively.

The same threshold of contributing area ($A_{crit} = 35\,\mathrm{m}^2$; Section 4.2.1.3) was applied to delineate the flow networks of the original surface and the evolved surface. The change of surface flow paths due to the development of erosion rills is visualised in Figure 4.8. The main change in the surface flow network of the SOCN simulation is a reduction of the number of flow paths. The erosion of a model cell, that is the source of a rill, likely attracts the drainage direction of neighbouring cells, due to the new topographic gradient. This increases the contributing area of the rill cell. Conversely, due to the redirection of drainage paths the contributing areas of some cells next to the rills may drop below the threshold to delineate flow paths (A_{crit}). For a few cells the evolving rill structures lead to the diversion of surface flow paths. The changes between the initial contributing area and the contributing area of the evolved surface simulated by the MB model are much more pronounced. Although the reduction of surface flow paths is observed, the diversion of the flow paths is dominant. Whereas for the SOCN model the majority of the eroded material was deposited in the lake at the end of the simulation, more material was sedimented on the slope of the catchment for the MB model and caused flow paths to change or be interrupted. This becomes especially evident in areas of high deposition as the area between the lake and the lower footslope, where many initial flow paths disappeared and new ones evolved.

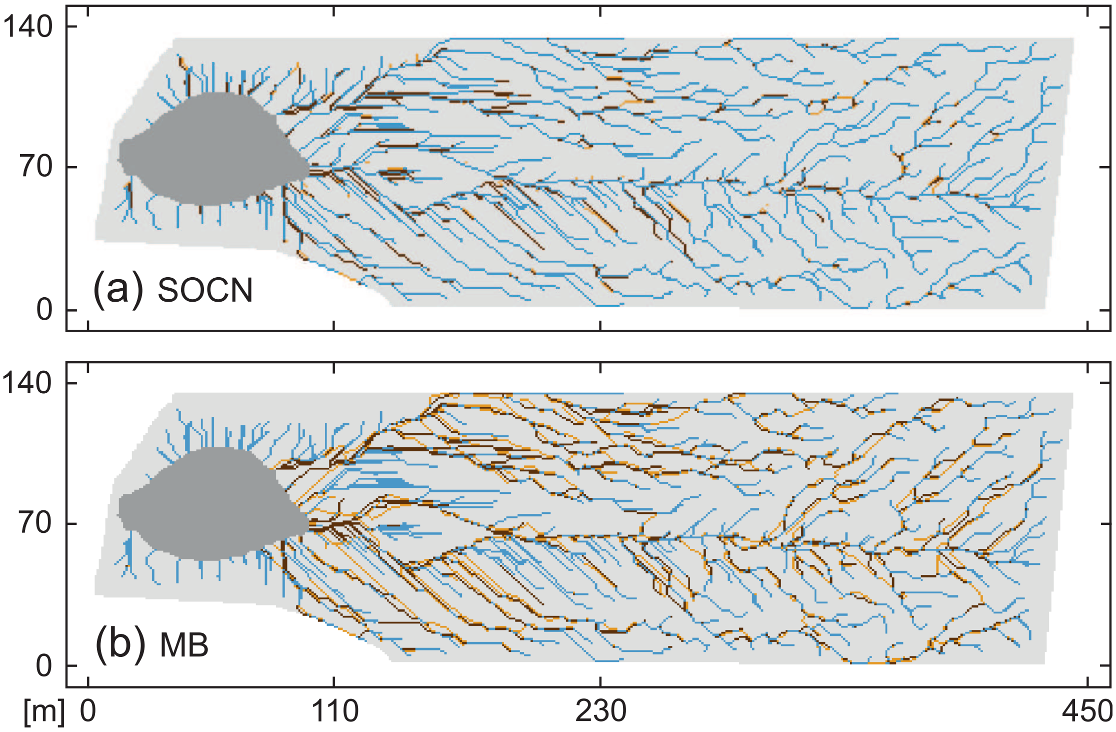

Figure 4.8: Comparison of the contributing area (representative for the surface flow paths) of the initial, unrilled surface topography and the evolved surface topography after (a) the SOCN model run and (b) the MB model run. Blue lines denote flow paths, which did not experience change due to the simulated erosion and deposition processes. The dark brown lines represent flow paths occurring on the initial topography, but not on the evolved surface anymore. The orange lines are flow paths, which were not present on the initial surface, but evolved due to the erosion and deposition induced change of topography.

4.4 Discussion

We used two different model approaches to simulate rill initiation and further growth of the rill network of the man-made catchment Chicken Creek. The catchment characteristics at the starting point of the project in 2005, a slightly sloping, unvegetated sand soil with a flattened, rill-free soil surface, provided excellent conditions to test erosion rill models at a larger scale than the usually studied flume or plot scale. The first model was based on the principle of minimal energy expenditure in the entire surface flow network (Rodríguez-Iturbe and Rinaldo, 1997), whereas the second model was based on well-established physical and empirical equations for surface water runoff and sediment entrainment. Both models display dynamic erosion phenomena, which finally trigger the geomorphology of the rill network.

4.4.1 Surface flow networks

Both methods for delineating the surface flow network, the contributing area on the one hand and the method based on the Manning equation on the other, were able to reproduce the main features of the measured rill network on the catchment's footslope and on the backslope for high flow convergence areas around the major middle rill. Comparing the initial contributing area presented in Figure 4.8 (dark brown and blue lines together) with the measured rill network it is obvious that the contributing area is a good indicator for predicting rill locations in steeper parts of the catchment (on the footslope) and in areas with high flow convergence (along the major rill on the backslope). However, using the contributing area (above a certain threshold) derived from a DEM as proxy for the rill network has several disadvantages when applied to the Chicken Creek catchment. (1) It overestimates the rill density found in flatter parts of the slope with low flow convergence. (2) It is not able to provide information on rill depths, and (3) the method does not account for the dynamics of an altering surface flow pattern due to the elevation change induced by erosion. To overcome these limitations the representation of flow paths has to be combined with erosion and deposition processes.

4.4.2 Erosion rills

Both models account for the dynamic change of topography induced by water erosion and sediment deposition as the topography is successively updated at the end of each iteration step and flow paths at the following iteration step are newly calculated based on the updated topography. Rill erosion in the SOCN model is a function of contributing area and local slope. Thus, for the rather flat areas on the backslope with low contributing areas only few rills are simulated and the rill density and rill depths on the backslope as well as on the footslope are properly reproduced. However, for the MB model the simulated rill network was very similar to the flow network, thus the rill density of the backslope was clearly overestimated. Additionally, the simulated rills were generally too shallow. A possible reason for these problems could stem from the way precipitation was represented in the MB model. For each precipitation step the same amount of rainfall was added (1.8 mm). Higher amounts of rainfall would cause higher flow depths, especially in flow convergence areas, resulting in increased erosion. Although precipitation data on a high temporal resolution (hours) are available for the Chicken Creek catchment there is limited information on the distribution of infiltrating water and surface runoff at a high temporal scale and how these are related to the rainfall threshold to produce runoff observed in the Chicken Creek. Further research is needed to clarify infiltration-runoff relationships for temporally high resolution rainfall data in order to estimate the real amount of water available for erosion relevant surface runoff. Nevertheless, the MB model was able to locate the evolving rills in the catchment and to distinguish zones of high and low erosion activity based on only very few general catchment characteristics (topography and average texture). The simulated evolving rill network changed surface flow patterns in many areas of the catchment, but only at a rather small spatial scale. Thus, the basic surface flow pattern did not alter fundamentally with erosion and deposition processes. Therefore, the initial topography of the Chicken Creek catchment was considered as the main control on determining the location of the erosion rills.

4.4.3 Rill network evolution and stability

The development steps of the SOCN model shown in Figure 4.7 reveal the transition of the initial system from non-equilibrium to steady state, where no further erosion takes place. The evolution of rills in the SOCN model does not necessarily progress strictly by headward growth, but is rather driven by local slope instabilities (Rodríguez-Iturbe and Rinaldo, 1997). However, the catchments topography with a steeper footslope where contributing areas are high (unstable slopes) favours the initiation of the rills in the area near the lake from where they propagate headwards. The good agreement between measured rills and those simulated with the SOCN model indicates that, until September 2006, the rill network of the Chicken Creek catchment formed according to the underlying process of the SOCN model, i.e. the minimisation of energy in the entire network. It is, however, not clear to what extent the steady state of the rill network reached in 2010 is controlled by energy minimisation. It is likely that the upcoming pioneer vegetation in spring 2007 and the increase of vegetation patterns thereafter played a major role for the decrease of rill formation. The increase and distribution of vegetation patterns in the Chicken Creek catchment is currently assessed and will allow for a more detailed investigation of the relationship between upcoming vegetation and rill formation.

For the MB model rill initiation started in zones of high flow convergence and developed along the main runoff paths of the surface flow network. The final state of the rill network is a product of the amount of precipitation added to the catchment. Network evolution will continue with proceeding time, i.e. additional precipitation. However, the series of evolution steps presented in Figure 4.7 indicates that further rill development is likely to occur especially as rill deepening and less as elongation of the rill network. Because of the increasingly important role of vegetation after the appearance of pioneer species in spring 2007, further rill deepening beyond the year 2006 cannot be understood without taking the vegetation and its effect on soil erosion (stabilisation of soil surface, change of infiltration capacities, retention of sediment) into account. However, regarding the spatial rill network extension the state in September 2006 can be considered as steady state.

4.4.4 Sensitivity of free parameters

4.4.4.1 Parameters in the SOCN model

An advantage of both models is the low number of parameters. Using the SOCN model three free parameters had to be defined: d_e describes the elevation reduction caused by erosion per iteration step for the model cell with maximum shear stress. In the original model of (Rinaldo et al., 1993) d_e was chosen dynamically at each iteration step so that the elevation of the cell was eroded to a value which yielded $\tau = \tau_{ce}$. Although producing reasonable rill patterns this method was not suitable for simulating the rill network in the Chicken Creek catchment, as rills can easily get as deep as several metres. In order to reduce the simulated rill depth, we defined d_e as a static parameter with the value of 0.01 m. The rill network length and especially the average rill depth are sensitive to changes in d_e. Decreasing d_e to 0.002 m reduced total rill network length by 28 % and average rill depth by 78 %. On the other hand, assuming a d_e of 0.02 m increased the total rill network length by 40 % and the average rill depth by 67 %.

The second free parameter is the critical value for deposition τ_{cd}. It has been argued by Partheniades (1977) and Mimura (1993) that erosion and deposition do not occur simultaneously. This means that the critical value for erosion τ_{ce} is equal to the critical value for deposition τ_{cd}. Thus, if the shear stress τ is higher than the critical value erosion takes place and for subcritical τ deposition occurs. This simple, binary approach of erosion and sedimentation has often been used (e.g. Mercier and Delhez, 2007) because of its straightforward implementation in models. However, other studies suggest erosion and deposition processes at the same time (Rose et al., 1983; Huang et al., 1999; Hairsine et al., 2002) indicating that the critical value for deposition is larger than the critical value for erosion ($\tau_{cd} > \tau_{ce}$). For shear stresses between τ_{ce} and τ_{cd} erosion, as well as deposition occur. We tested several values of τ_{cd} up to two times the τ_{ce} value to assess the condition of coexisting erosion and deposition processes and found low variance in simulated average rill depth and total network length ($< 10\,\%$). Significant changes occur only for $\tau_{cd} > 2\tau_{ce}$. Thus, we consider it justified to use $\tau_{ce} = \tau_{cd} = 0.81\,\mathrm{N\,m^{-2}}$ for the Chicken Creek catchment.

The last free parameter in the SOCN model is the erodibility factor H, which accounts for a decrease of soil erodibility with progressing erosion at a cell. Assuming an increasing density with soil depth due to compaction of the dumped sand body we chose a value of $H = 4\,\%$. Total network length, as well as average rill depth, is sensitive to changes of H. Choosing $H = 3\,\%$ increases total network length by 10 % and average rill depth by 22 %, whereas the selection of $H = 5\,\%$ decreases total network length by 6 % and average rill density by 17 %.

In summary, the SOCN model uses three free parameters only two of which are sensitive to changes (the elevation reduced by erosion and the erodibility factor). The range of reasonable values for these two parameters is rather narrow. Further research on the magnitude of eroded material per rainfall event and of the change of critical shear stress with soil depth is needed to determine the two sensitive free parameters.

4.4.4.2 Parameters in the Manning-based model

All free parameters of the MB model were derived from data or from empirical studies and therefore the possibility for varying parameters is limited. However, the particle diameter d_p should be further discussed as it is considered the most uncertain parameter and directly affects the erosion rate. We used a single grain size (0.4 mm diameter) representative for the texture class ‘middle sized sand’, which is the most abundant class occurring in the texture samples of the catchment. Decreasing d_p to the lower particle size boundary for sand (0.063 mm) has three effects: more sediment is eroded for a certain shear stress, sediment entrainment starts for lower shear stresses, and sediment is deposited at a reduced rate. Increasing d_p to the upper particle size boundary for sand (2 mm) has the opposite effects. The reduction of d_p to 0.063 mm increased the network length by 69 %. The average rill depth increased slightly by 14 %, mainly because of enhanced rill depths at the centre line of the catchment, where surface runoff concentrates (maximum simulated rill depth: 1.48 m). Choosing d_p equal to the upper particle diameter of 2 mm for sand reduced the rill network length by 74 % and increased the average rill depth by 71 %. The high simulated average rill depth is the result of the short, but relatively deep rill network with a maximum simulated rill depth of 0.72 m. A thorough investigation of the model behaviour for polydisperse sands is left to future research.

4.5 Conclusions

Both of the presented models were successful in simulating the initiation and further evolution of the main erosion rills emerging in the initial development phase of the Chicken Creek catchment. In steeper parts of the catchment and in zones of flow convergence the simulation of flow paths across the initial topography seems to be a reasonable indicator to predict the location of erosion rills. However, neither the dynamic change of topography and thus flow paths, nor the information on rill depth are represented in the simulation of flow paths. Therefore, the consideration of erosion and deposition and the successive adaptation of the surface topography due to these processes additionally had to be taken into account in the models.

Regarding the questions asked in the introduction, this work demonstrated that the location of the main surface erosion rills could be predicted by both of the model approaches. The measured main rills in the catchment developed during the first year and the lengthways rill evolution was much less pronounced thereafter and a steady state was reached in 2010. Both of the models succeeded in reproducing the observed convergence of the rill network length to a steady state. The simulations further showed that erosion and deposition processes forced the surface flow paths to change gradually during rill evolution. However, these changes affected the flow paths only locally. The initial topography of the catchment governed the general direction of water flow during the entire rill development and thus was the key factor in determining the location of the rills.

5 A new model concept to describe catchment-scale water flow

5.1 Motivation

Hydrological catchments are highly dynamic and complex systems encompassing a considerable degree of landscape heterogeneity and a variety of interacting and often nonlinear hydrological processes operating at many different spatial and temporal scales. Although many of the governing hydrological processes have been described and investigated in detail, the success of modelling flow and transport at the catchment scale is still limited. One of the reasons for limited predictability is the foundation of the present hydrological models on small-scale physics and theories (Kirchner, 2006). While the mathematical formulations of the described processes often are sophisticated and work fine at the small scale, they usually fail when applied to larger scales. A prominent example is the Richards equation describing water flow in unsaturated soil (Richards, 1931). Applied to soils dominated by matrix flow it is often consistent with point-scale measurements using tensiometers or TDR probes (McDonnell et al., 2007). However, at larger scales other flow regimes, such as preferential flow (Weiler and Naef, 2003), or nonlinear processes, such as the threshold behaviour between rainfall and runoff (Section 2.4.1) may become dominant and cannot be captured by the global application of equations valid only for a small scale.

Another problem of many hydrological models is the insufficient representation of spatial heterogeneity. We have seen that small-scale heterogeneities in the geometry of the Chicken Creek catchment and spatial distribution of soil physical properties determine the pattern of subsurface flow path connectivity at the catchment scale (Chapter 3). Similarly, the initial micro-topography of the surface dictated the macro-scale pattern of the surface erosion rill network (Chapter 4). Both, the subsurface flow and the surface erosion rill patterns can be regarded as emergent properties of the catchment, i.e. macro-scale properties, which are entirely unpredictable from the observation of the governing small-scale processes alone. These macro-scale patterns have to be considered in simulations, because they can have a significant impact on the hydrological behaviour of the catchment. For example, for slopes with rill development driven mainly by surface runoff, subsurface flow paths will be affected by the emergence of the rills, due to the increased saturated hydraulic conductivity in the rills (Biemelt et al., 2005; Gerwin et al., 2009b) and the abundant water supply caused by the convergence of surface runoff. At present, there are only very scarce information on how erosion rills affect the subsurface flow paths at the catchment scale.

While many hydrological models are able to reproduce the rapid and flashy stream flow response to rainfall input characteristic for small catchments, tracer studies raised the question if the simulation results of runoff are achieved for the right reasons (Kirchner, 2006), that is for the realistic description of flow processes and storage in the model. Analyses of passive tracer signals (e.g. isotopes, chloride) in rainfall and stream runoff revealed that stream peak flows consist mostly of pre-storm water released from the catchment (Buttle, 1994; Richey et al., 1998; Kendall and McDonnell, 1998; Kirchner et al., 2000) rather than of rainfall flowing quickly along the catchment into the stream. This finding is at odds with the processes describing the rapid rainfall-runoff response (e.g. saturation excess flow, pipe flow) commonly incorporated in models. Although the consideration of water transit times in models can provide important constraints on hypothesised mechanisms for stormflow generation (Kirchner, 2006; McGuire et al., 2007), the estimations of travel time distributions are usually based on the assumptions of steady-state flow and time invariance of flow paths (McDonnell et al., 2010) and are rarely reflecting natural conditions. To improve our process understanding of flow paths and the rainfall-runoff response, models allowing for the simulation of catchment runoff and of the correct and dynamic transit time distributions are required, since they are more likely to represent a valid conceptual and mathematical description of the runoff processes (McDonnell et al., 2010).

A new three-dimensional model is conceptualised in this chapter in order to tackle the drawbacks of current hydrological models described above. The idea was to combine concepts of the model based on Percolation Theory (PT model, Section 3.2) with common physical concepts describing water flow. The application of physical equations valid at the small scale (e.g. Darcy-based flow) is justified by using a high resolution model grid. Additionally, the high resolution accounts for a reasonable degree of heterogeneity of soil physical parameters, and thus allows for the eventual emergence of macro-scale patterns. The aim of this chapter is to present a model framework, which is capable to reproduce runoff processes, transit times, and the emergence and effect of hydrologically relevant structures at the macro-scale. The focus of this study is not on simulating runoff components as precise as possible compared to measurements, but rather on testing the feasibility of the new model concept. Furthermore, it should be emphasised that this model so far covers the most important physical processes and further work is needed to implement a more complete process description. Nevertheless, to demonstrate the practicability of the model, first simulation results of flow paths and travel time after a intense rainfall event are presented. Following questions are addressed:

- How do hydrological surface and subsurface flow paths connect in space and time?
- What are characteristic flow distances, times and velocities of surface water and how do they change in the presence of surface erosion rills?
- What effect do the erosion rills have on total surface water outflow?

In Section 5.2 the new hydrological model is conceptualised and the model setup for a single rainfall event is described in Section 5.3. The first results of the model test are presented in Section 5.4 and discussed in Section 5.5. Concluding remarks are summarised in Section 5.6.

5.2 Model description

In contrast to the static PT model (Section 3.2) the new model accounts for the spatiotemporal dynamics of infiltration, surface and subsurface water flows, and thus for the variability of soil water content in the catchment. Following basic concepts of the PT model were integrated into the new model: First, a free water capacity threshold (Section 3.2.4) was introduced to distinguish between slow and fast subsurface flow. Fast flow occurring at water contents above the free water capacity threshold was assumed to be equal to the saturated hydraulic conductivity (in contrast to flow at water contents below that threshold for which the hydraulic conductivity decreases with water content). Second, subsurface flow path connectivity is defined as cluster of model cells with water exchange. Thus, a model cell with soil water outflow and the neighbouring cell receiving the outflow both belong to the same flow path (cluster). Third, a small spatial resolution was considered to represent heterogeneities, and thus to allow for the eventual emergence of macro-scale structures. The model architecture and the processes considered in the model are described in detail below.

5.2.1 Model grid

As in the case of the two rill evolution models (SOCN and MB model, Sections 4.2.1 and 4.2.2, respectively) the surface flow paths were described on a two-dimensional Cartesian lattice containing the elevation information of the DEM. Each lattice cell is connected via the Moore neighbourhood defined by the four neighbours located in orthogonal direction and the four neighbours situated in diagonal direction. The spatial domain of the soil was constrained by the DEM of the surface (upper boundary) and the DEM of the clay layer (lower boundary). As in the case of the PT model the soil body was discretised into a three-dimensional face-centred cubic (fcc) lattice (Figure 5.1). The small resolution of 0.5 m was used for both, the two-dimensional surface lattice and the three-dimensional soil lattice. The fcc lattice comprises a total of 431 374 cells, each having the volume V_i of a rhombic dodecahedron of 250 litres.

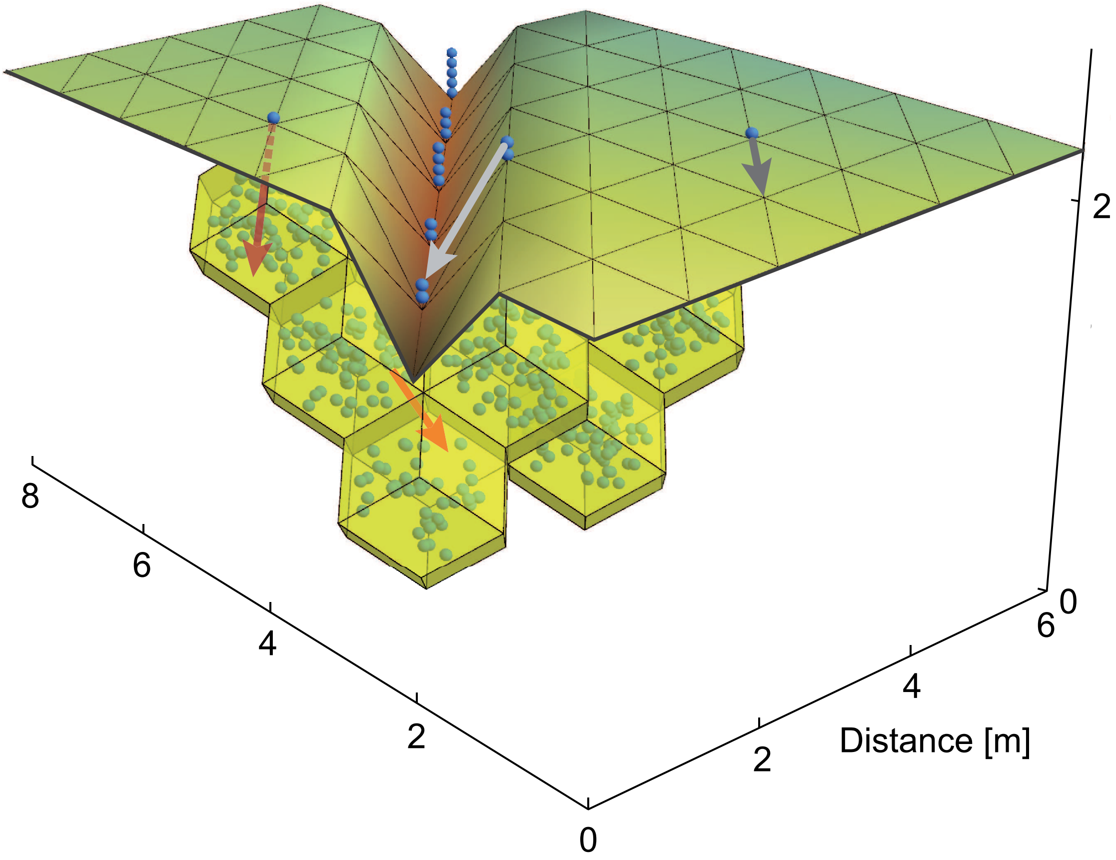

Figure 5.1: Schematic description of the hydrological model for a sub-system including a rill and six selected fcc soil cells (yellow dodecahedrons). For the sake of clarity a reduced number of water elements (blue spheres) is shown corresponding to the water content of 5 % in the lowest fcc cell and 8 % in the other fcc cells. The arrows describe modelled water transport processes: surface runoff along the steepest slope gradient (light and dark grey arrows), infiltration, (red arrow) and soil water flow (orange arrow) along the maximum hydraulic gradient.

5.2.2 Water flow as transport of water elements

Water in the model is transported in discrete volume units called 'water elements'. The advantage of moving discrete water elements is that the flow path of each individual element can directly be tracked from the location of its formation to the final position at the end of the simulation. Additionally, for every water element the time period needed to cover the distance of its flow path can be analysed. Thus, the transit times of all water occurring in the system can be computed. A water element in the model has the volume of 0.1 litres. Depending on the soil properties the water content of a model cell at saturation corresponds to approximately 950 water elements. Rainfall hitting the soil is stored until the surface water volume allows the building of a water element. Thereafter, the water element either is infiltrated, transported as surface runoff, or not moved at all (Figure 5.1) according to the rules described in the following sections. Evaporation from the catchment surface is assumed to be negligible during rainfall events and thus is not considered in the presented version of the model.

5.2.3 Potential water transport capability: From continuous to discrete water flow

The soil-physical equations for infiltration, surface runoff and subsurface water flow (Sections 5.2.4, 5.2.5 and 5.2.6) are based on non-discrete fluxes and volumes of water and must be adapted for our model with discrete water elements. For that purpose a corresponding ‘potential water transport capability’ for each flow processes was introduced as explained here for infiltration. Consider at time step t a water element on a horizontal soil surface and an infiltration capacity (defined by Philip’s theory of infiltration) of half of a volume unit per time step. The problem in such a case is that the infiltration capacity would be overestimated if the water element is allowed to infiltrate and would be underestimated if the water element is not allowed to do so. To solve this problem the ‘potential infiltration capability’ was introduced and defined based on the infiltration capacity at time step t and the infiltration history as follows: The algorithm decides randomly whether the water element is infiltrating or not. The potential infiltration capacity stores the value of overestimation (infiltration surplus, positive capability) or underestimation (infiltration deficit, negative capability) of the infiltration capacity. At the next time step $t + 1$ the updated infiltration capacity, defined as the sum of the infiltration capacity at $t + 1$ (determined by Philip’s theory) and the potential infiltration capability determined at t, decides whether a water element can infiltrate or not.

5.2.4 Infiltration

The representation of rainfall water at the soil surface is a key property for modelling the hydrology of ecosystems prone to extensive surface runoff and erosion and must be modelled as adequate as possible. We used Philip's model (based on Richards equation) with time compression approximation to describe infiltration (see below). Infiltration depends on the initial soil water content θ_0, the rainfall intensity P, and the hydraulic conductivity K at the soil surface. The infiltration rate in the model is calculated based on the infiltration theory of Philip (1957) and the estimation of sorptivity (capacity to adsorb water based on capillarity) according to Parlange (1975). Philip's equation describes the decrease of the infiltration rate φ with time as

$$\varphi(t) = \frac{1}{2} S t^{-1/2} + \varphi_{fin} \tag{5.1}$$

where t is time, φ_{fin} is the final infiltration rate estimated as $\varphi_{fin} = K_s/2$ and S is sorptivity. Following Parlange (1975) sorptivity is expressed as function of soil water diffusivity $D(\theta)$:

$$S^2 = 2\left(\theta_s - \theta_0\right) \int_{\theta_0}^{\theta_s} D\left(\theta\right) d\theta \tag{5.2}$$

$$D\left(\theta\right) = K\left(\theta\right) \frac{dh}{d\theta} \tag{5.3}$$

where θ is water content, θ_s is water content at saturation, θ_0 is initial water content, K is hydraulic conductivity, and h is suction pressure head. At the beginning of a rainfall event the potential infiltration rate determined by Equation (5.1) will exceed the precipitation rate until the time point t_p is reached, where the potential infiltration rate and the rainfall rate are equal. Thereafter, the precipitation rate exceeds the infiltration rate and ponding of surface water starts. Thus infiltration rate equals

$$\varphi(t) = \begin{cases} P & \text{for } 0 \leq t \leq t_p \\ \frac{1}{2} S t^{-1/2} + \varphi_{fin} & \text{for } t > t_p \end{cases} \tag{5.4}$$

According to Philip's infiltration theory, the time to ponding t_p can be derived by setting Equation (5.1) equal to P and solving for time:

$$t_p = \frac{S^2}{4\left(P - \varphi_{fin}\right)^2} \tag{5.5}$$

However, for conditions of constant flux P (and as opposed to Philip's constant head assumption), a flux-based time correction, known as time compression approximation (TCA), must be considered (Rigby, 2009). The corrected time to ponding t_c can be determined by using cumulative infiltration as surrogate for time (Liu et al., 1998). Assuming that the infiltration calculated with the Philip equation and cumulated up to the time t_p is equal to the cumulative infiltration under the constant flux up to the time t_c the time to ponding is defined by:

$$\int_0^{t_p} \varphi(t) dt = P t_c \tag{5.6}$$

where $\varphi(t)$ is defined in Equation (5.1). After solving for t_c and inserting Equation (5.5) for t_p the corrected time to ponding is given as

$$t_c = \begin{cases} \frac{S^2\left(2P - \varphi_{fin}\right)}{4P\left(P - \varphi_{fin}\right)^2} & \text{for } P > \varphi_{fin} \\ \infty & \text{for } P \leq \varphi_{fin} \end{cases} \tag{5.7}$$

According to the corrected time of ponding the infiltration rate given in Equation (5.1) is modified to:

$$\varphi(t) = \begin{cases} P & \text{for } 0 \leq t \leq t_c \\ \frac{1}{2} S \left(t - \left(t_c - t_p\right)\right)^{-1/2} + \varphi_{fin} & \text{for } t > t_c \end{cases} \tag{5.8}$$

5.2.5 Surface flow

Water that cannot infiltrate due to a limiting infiltration capacity is transported at the surface to the neighbour cell in the direction of the steepest gradient based on the Manning equation (Equation (4.4)) and according to Equation (4.6).

5.2.6 Subsurface flow

Each model grid cell is defined to be in one of two possible states: 'wet' with saturated hydraulic conductivity and 'dry' with unsaturated hydraulic conductivity according to the water content of a grid cell. As in the PT model, the free water capacity threshold θ_t (Equation (3.3)) is used to distinguish between the two states. Subsurface runoff was then based on Darcy flow (Scheffer and Schachtschabel, 2002):

$$Q_{soil} = K(\theta)\left(\frac{-dh_w}{d\Delta z} + 1\right) \qquad \text{for 'dry' conditions } (\theta \leq \theta_t) \tag{5.9}$$

$$Q_{soil} = K_s\left(\frac{-dh_w}{d\Delta z} + 1\right) = K_s \qquad \text{for 'wet' conditions } (\theta > \theta_t) \tag{5.10}$$

where Q_{soil} is subsurface runoff, $K(\theta)$ is unsaturated hydraulic conductivity, K_s is saturated hydraulic conductivity, h_w is hydraulic head, and Δz is depth.

5.2.7 Model time step

Since surface flow generally occurs with higher velocities than subsurface flow, two separate dynamic time steps are calculated by the model: one for surface flow t_{surf} and the other for subsurface flow t_{soil}. The surface flow time step, limited by the maximum surface flow velocity v_{max}, is calculated according to Equation (4.7). The time step for subsurface flow is calculated accordingly except that v_{max} is replaced by the maximum saturated hydraulic conductivity of the soil. To assure steady, temporally smooth simulation results of the flows a maximum time step

t_{crit} was defined and surface or subsurface time steps larger than t_{crit} were set equal to t_{crit}. We chose $t_{crit} = 60\,\mathrm{s}$ as this was a reasonable trade-off between simulation result smoothness and computer processing time.

5.3 Model setup

5.3.1 Random distribution of soil characteristics

For each of the 316 texture sample sites described in Section 2.3.1 the set of van Genuchten parameters (n, α, θ_r, θ_s) was determined by a pedotransfer function (Section 2.3.2). We assume that the soil hydraulic properties are randomly distributed in space. In the model, we assigned a random number between 0.0 and 1.0 to all of the lattice cells. This random number was then translated to a n-value according to the sum distribution of the 316 n-parameters (analogue to Figure 3.4b). If the value of the random number lays between two n-values on the sum curve, the n-value closer to the random number was selected. The selected parameter n was then assigned, together with its corresponding remaining van Genuchten parameters (α, θ_r, θ_s), to the model grid cell.

5.3.2 Initial soil water content

The initial soil water content was defined upon the assumption of an increasing moisture gradient with soil depth. The soil water content of the lowest model cell in a soil column was set to field capacity, defined as the water content at a suction of $-0.65\,\mathrm{m}$ (Scheffer and Schachtschabel, 2002). The water contents for the cells in the soil column lying above the lowest cell were determined by a linearly decreasing suction gradient of $0.1\,\mathrm{m}$ per cell. The average soil water content in the system determined by this method was $19\,\%$ corresponding to about 180 water elements in a model cell.

5.3.3 Rainfall input and catchment outlet

The hydrologic response to a single rainfall event occurring in the early phase of ecosystem development (May/June 2006) with a total of 35.6 mm rainfall was modelled. To simplify computations we used a constant rainfall rate of 2.1 mm h^{-1} defined as half of the events maximum measured precipitation intensity. The duration of the event in the simulation, defined by this constant precipitation intensity and the measured total rainfall amount of the event, was 61 029 s (Figure 5.2). The total duration of the simulation was set to 100 000 s to allow water elements remaining at the surface after the rainfall event to infiltrate or run off along the surface. The total water amount of the rainfall event corresponds to 15 684 240 water elements. The outlet of surface and subsurface water is the boundary of the lake basin defined as the area with a surface elevation lower than 126.5 m above sea level. The outlet boundary is characterised by the constant negative pressure potential of -150 m.

5.3.4 Adaptation of the surface saturated hydraulic conductivity

Limited infiltration capacities caused intense surface erosion in the very beginning of the ecosystem development (October 2005 – September 2006). The influence of exfiltrating groundwater as erosion agent was excluded, since groundwater levels in the catchment never rose higher than about one metre below soil surface in this period (Mazur et al., 2011).

Relating the twelve precipitation events occurring between October 2005 and September 2006 (Section 4.2.2) to the infiltration rates calculated by the Philip equation revealed that none of the events showed large enough precipitation intensities to generate surface runoff (Figure 5.2). In fact, the estimated saturated hydraulic conductivity of the surface had to be decreased by a factor $f \approx 1/5000$ in order to produce realistic surface flow patterns. The test of simulating surface runoff with a physically-based one-dimensional model (COUP model; Jansson and Karlberg, 2001) was neither successful, even with a highly restrictive parameter

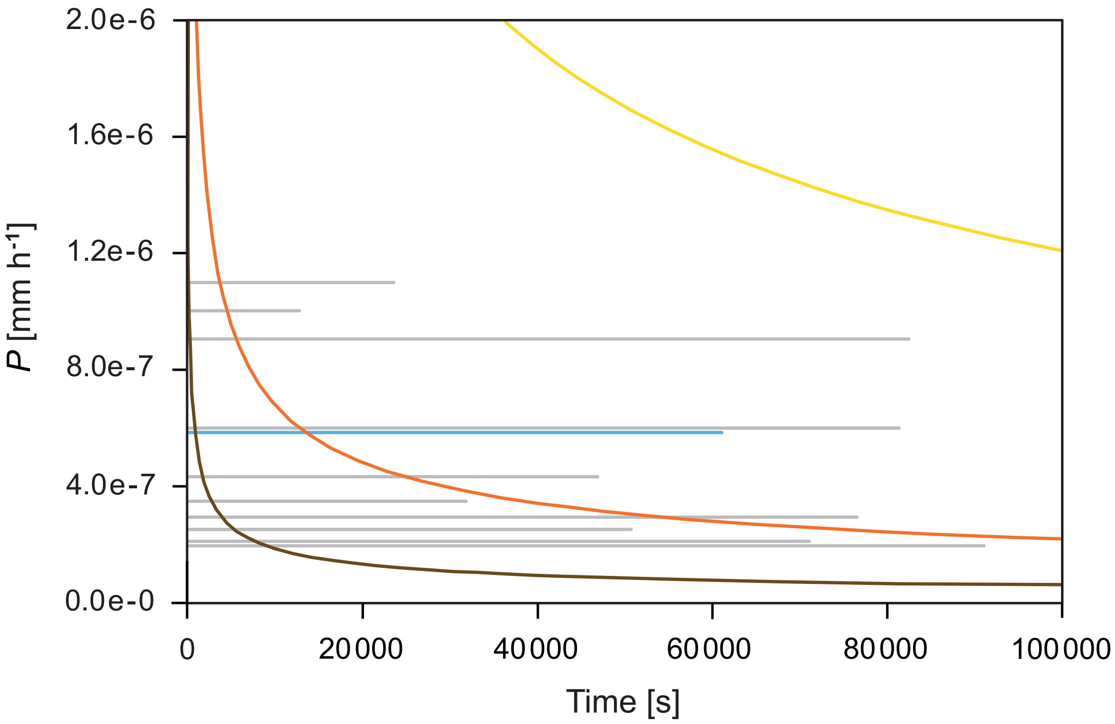

Figure 5.2: Infiltration rates determined with the Philip equation. Since the infiltration rate depends on soil texture, the range of infiltration rates defined by the most sandy (yellow curve) and the least sandy (brown curve) of the measured soil textures is shown. The orange curve represents the infiltration rate for the average soil texture. The rainfall intensities for all rainfall events between October 2005 and September 2006 are depicted as grey lines, whereas the representative event used in this study is shown in blue. Note that without the reduction of the saturated hydraulic conductivity at the surface by the factor f all the infiltration rates would shift upwards on the y-axis and no surface runoff would occur.

setting (Stähli, pers. comm.). These findings indicate that other mechanisms than sorptivity that are not represented in the Richards equation or the Philip equation determine the occurrence of surface flow. The reduction of saturated hydraulic conductivity at the surface is further discussed in Section 5.5.2.2.

5.3.5 Simulations

To investigate the effect of the erosion rills on the surface and subsurface flow paths and on surface flow distances, times and velocities, two simulations with the same rainfall event were conducted: one with the initial non-rilled surface topography and one with the developed topography including the rill network resulting from the SOCN model run (Section 4.3.3). The DEMs of the initial and the developed topography originally available at 1 m resolution were downscaled by interpolation to the 0.5 m resolution used for the model described in this chapter. Based on a comparison of measurements between rill and interrill areas of a mining dump (Biemelt et al., 2005) the saturated hydraulic conductivity of a rill model cell was multiplied by a factor of 40. Due to the steep topographic gradients next to the rills, the concentration of surface flow and the higher saturated hydraulic conductivities in the rills, the flow paths are likely to change qualitatively and quantitatively whether surface rills are present or not.

5.4 Results

5.4.1 Surface runoff

For both simulations (without and including erosion rills) all the water elements had either infiltrated or left the system via outflow at the end of the simulation (after 100 000 s). For each single water element the flow path along the surface was recorded until the water element infiltrated or flowed out of the system. Water elements infiltrating on the same location as they originated do not constitute a flow path, thus flow paths comprise at least two surface model cells (the cell the water element is originating from and the receiving cell). Figure 5.3 shows the temporal evolution of the flow paths along the initial surface topography (no rills). To prevent the figure from being overloaded the flow paths of only every 500th water element are shown. According to Philip's infiltration theory, the catchment is governed by infiltration in the beginning of a rainfall event. This is reflected in Figure 5.3 showing that up to 30 000 s (ca. half of the rainfall events duration) only scarce and short surface flow paths were built. With enduring rainfall more and more model grid cells reach the point where the infiltration capacity decreases below the rainfall intensity. Therefore, an increasing amount of water is available for surface runoff, which gradually leads to longer flow paths. Although the flow

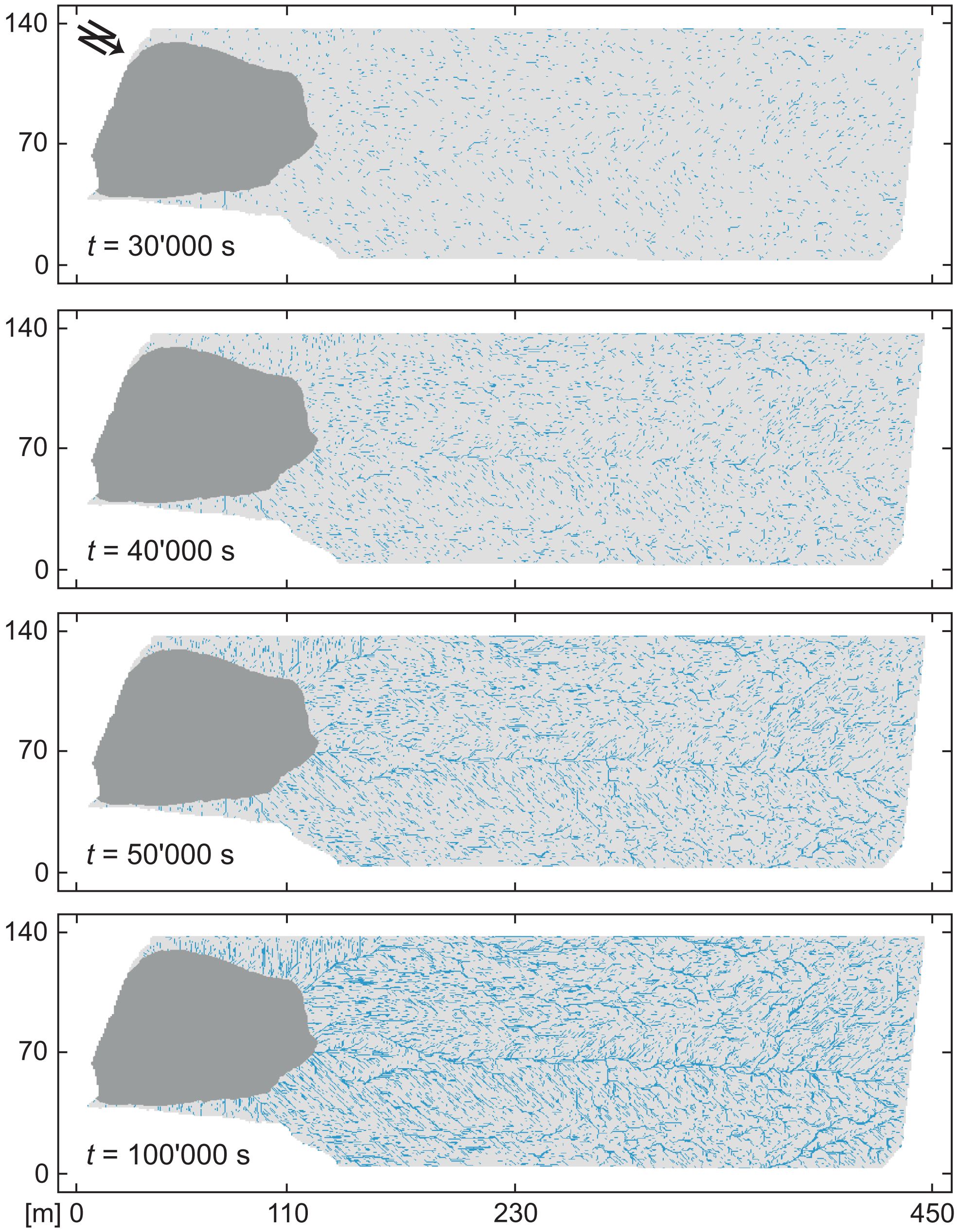

Figure 5.3: Temporal evolution of the surface flow paths defined by tracking every 500th water element. Up to 30 000 s the system is dominated by infiltration and surface flow paths are maximally a few metres long. As the infiltration capacity of more and more model grid cells decreases, surface runoff becomes increasingly important and the flow paths of the water elements start to grow. The flow path tracks of the water elements at the end of the simulation resemble closely those presented in Section 4.3.1 (Figure 4.3). Especially the main runoff path in the middle of the catchment and the flow paths in the backslope are well visible.

path of only every 500th water element is displayed in Figure 5.3, surface runoff structures are clearly identifiable after 100 000 s and they closely resemble the flow paths determined for the self-organised critical network model (i.e. the contributing area) or the Manning-based model (Figures 4.3b and 4.3c, respectively).

Figure 5.4 emphasises this similarity by superposition of simulated flow paths at the end of the simulation with the corresponding contributing area. Obviously, the method of discretising rainfall into water elements and representing surface flow by displacing these elements is successful in describing realistic surface flow patterns. Figure 5.4 also shows the comparison between the simulated flow paths based on the initial topography and the flow paths resulting from the developed topography including the erosion rills.

Generally, the flow paths between the two simulations are very similar. However,

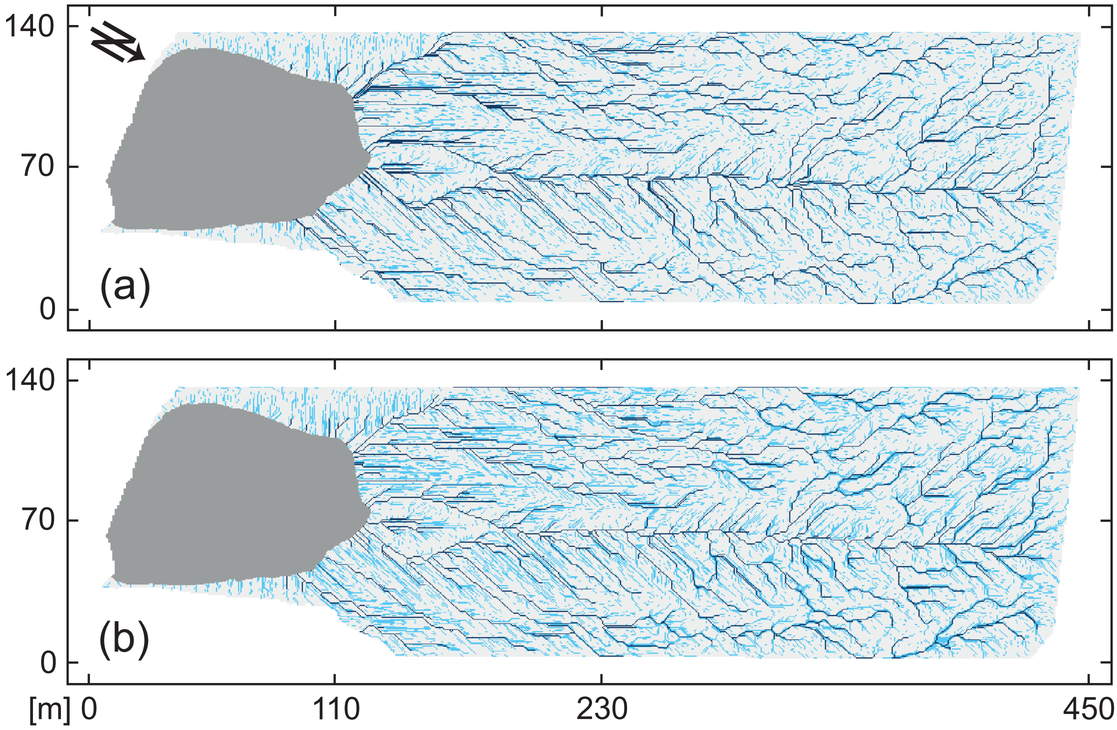

Figure 5.4: Surface flow paths (light blue) of every 500th water element displayed at t = 100 000 s for (a) the simulation with the initial surface topography and (b) the developed surface topography including the rill network. The dark blue lines show the contributing area and confirm general flow patterns depicted by the flow simulations of discrete water elements.

for the simulation including the rills, the flow network is apparently denser and more connected. On the one hand the higher degree of connection implies that individual water elements covered larger flow path distances. On the other hand the denser flow network indicates that less water elements had infiltrated and instead run off along the surface. Indeed, the simulation including the rills produced about three times more total surface runoff compared to the simulation without considering the rills (Figure 5.5). The lower total amount of infiltration for the simulation with rills may be surprising, since the model parameter setting promotes infiltration in the rills. Truly, the amount of infiltration in the rills was higher, but the steep topographic gradients next to the rills caused water elements to be transported more quickly to the rills and thus reduced their chance of infiltration

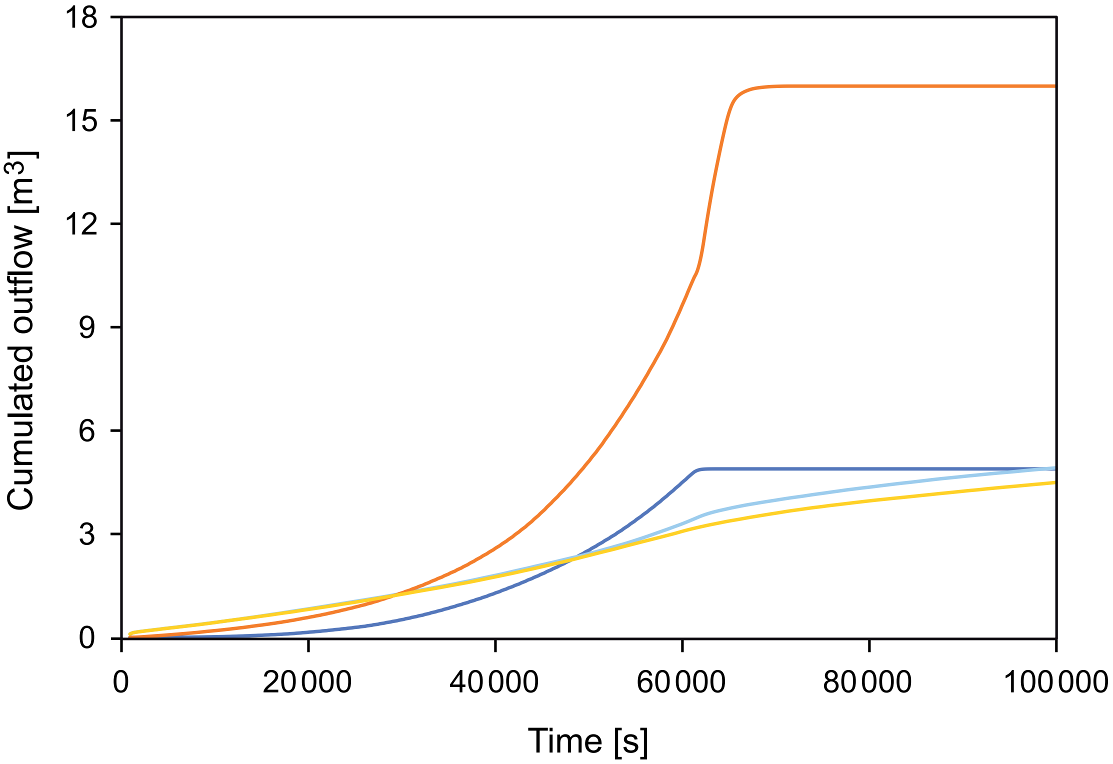

Figure 5.5: Cumulated surface runoff for the simulation with the initial surface topography (dark blue) and for the developed topography including the rills (orange) and cumulated subsurface outflow for the simulation with the initial topography (light blue) and for the developed topography (yellow). The curves were filtered by a 15-period moving average. The erosion rills have a significant effect on surface flow, but only a small influence on subsurface outflow.

in non-rill areas. Each water element flowing off from a cell reduces the cell's surface water level, allowing for higher flow depth gradients and replenishment by other water elements.

The larger the number of water elements moving along the surface, the higher is the probability that water accumulates locally, forcing the following water elements to alter their flow route, due to the change of the hydraulic gradient. This is reflected in the wider flow paths of the simulation with rills, especially in the relatively flat and rill-free backslope of the catchment (Figure 5.4b). Flow in the rills is concentrated again, since, due to the relatively high rill walls, the steepest gradient is always in the downslope direction of the rill. Therefore, the first visual inspection of Figure 5.4 can be somewhat misleading as it may give the impression that the wider flow paths conduct more water than the thinner ones constrained by the rill structures.

Figure 5.6 displays the relation between surface flow path length and surface flow time for each water element for simulations with and without erosion rills. While the flow path patterns for both simulations are very similar (Figure 5.4) the distance-time relationships of the water elements of the two simulations are considerably different. Water elements flowing along the initial surface topography are defined by shorter flow path lengths (maximum 90 m) and flow times (maximum 6442 s), and by a relatively low variance of the data points around the trendline representing the velocity $0.009\,\mathrm{m\,s^{-1}}$. In contrast, and as already indicated by Figure 5.4, the distance covered by a water element is generally much longer (up to 400 m) and flow times are higher (maximum 12 320 s) for the simulation including the erosion rills. Despite the higher flow times for the system with developed erosion rills the average velocity of $0.036\,\mathrm{m\,s^{-1}}$ is much larger than without rills. Although the infiltration capacity is higher in the rills, the steeper gradients account for large water supply to the rill exceeding eventually infiltration capacity and water elements are effectively transported through the narrow rills.

As already indicated by the temporal evolution of the surface flow paths (Figure 5.3), it can be seen that in the first half of the simulated rainfall event surface outflow to the lake basin is only marginal, but increases rapidly thereafter until rainfall stops at $t = 61\,029\,\mathrm{s}$ (Figure 5.5). While the simulation without erosion

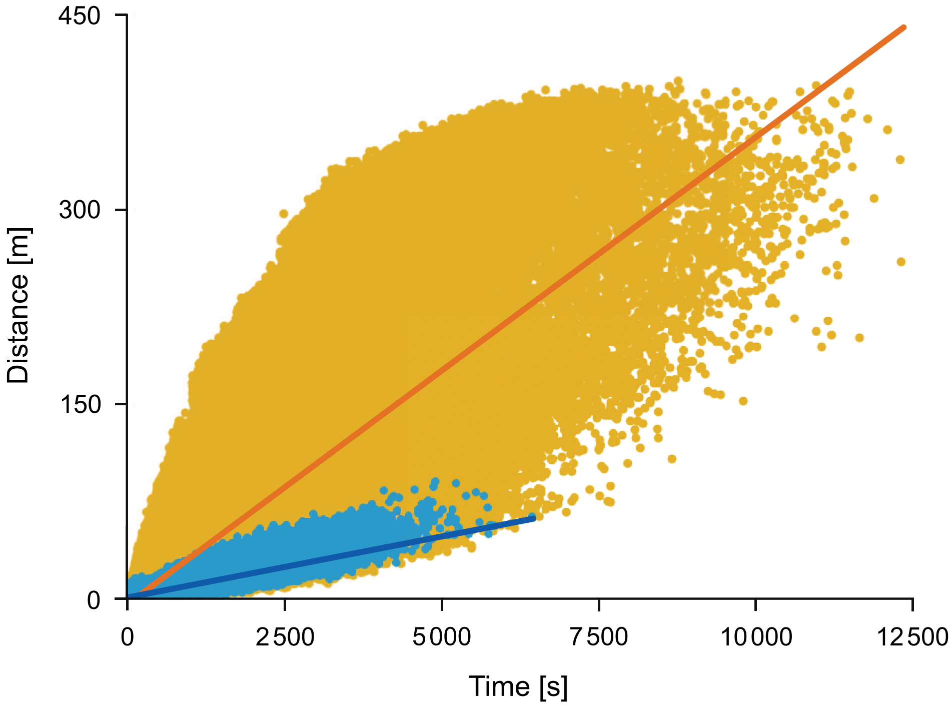

Figure 5.6: Relation between flow path length and time needed to cover the distance of each water element until it is infiltrating or reaching the outflow. Data are shown for the simulation with the initial surface topography (blue dots) and for the developed topography including the rills (yellow dots). Generally, runoff over the developed surface topography reached longer distances at a longer timescale and at higher characteristic velocities (indicated by the slope of the trendlines) than runoff over the initial surface.

rills produces surface runoff only from about 20 000 s onwards, outflow for the simulation with rills starts much earlier. This is because some of the rills near the lake basin reach down to the impermeable clay layer. Rainfall hitting such areas is immediately and rapidly transported within the rill to the outlet.

5.4.2 Subsurface flow

Figure 5.7 shows the temporal evolution of the subsurface flow paths for the simulation using the initial topography. The subsurface flow paths are defined by clusters of hydrologically connected soil cells (cells with subsurface in- or outflow during the simulation). Each cluster gets its individual cluster number. When

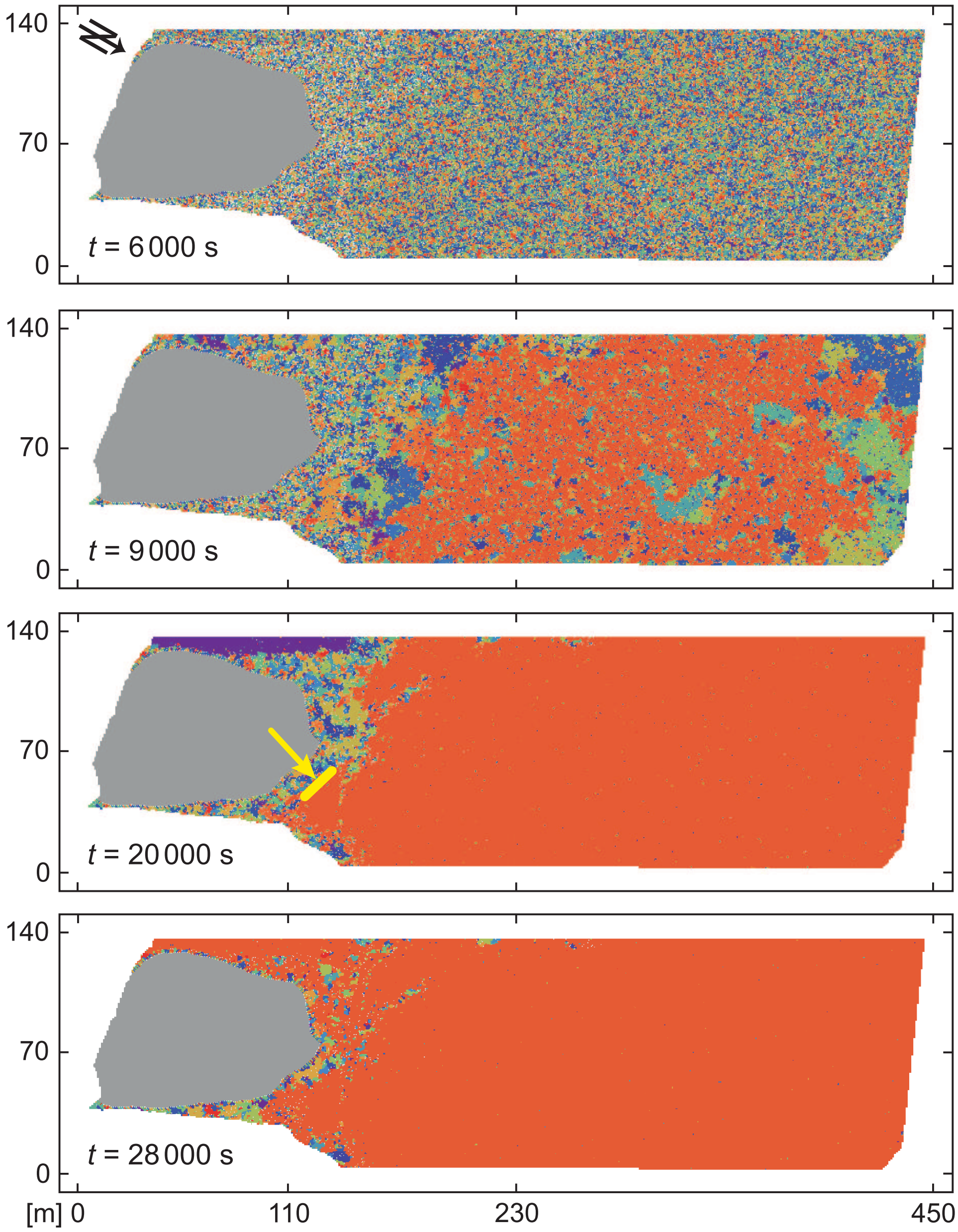

Figure 5.7: Temporal evolution of hydrologically connected clusters in the soil. After 6000 s only small clusters have formed in the catchment. The clusters then grew by merging until a large cluster spanning almost the entire system upslope from the clay wall was built (at $t = 9000$ s). After 20 000 s this large cluster connected with areas lakewards from the clay wall. The yellow bar indicated by the arrow marks the location of the soil moisture pattern (Figure 2.7). The connecting of flow paths is inhibited in this area and water flow is dammed resulting in the pattern of high moisture. After 28 000 s the large cluster covered almost the whole catchment and connected to the lake basin.

two clusters grow together the one with the larger number of cells persists and transmits its cluster number to all the cells belonging to the smaller cluster. The results of the three-dimensional model are displayed as vertical projection. If at a location (x, y) several model cells exist in z-direction (soil depth) and the cells belong to different clusters, the most abundant cluster number occurring in the soil column is shown in the projection. In the first 6000 s of the simulation (no rills) the initially fully unconnected system developed a fairly homogeneous distribution of small clusters scattered over the entire catchment. Thereafter, the clusters located headwards from the clay wall started to merge and grow. After 9000 s a connected cluster spanning almost the whole catchment northwards from the wall had formed. This large cluster further expanded lakewards over the clay wall on the orographic left and right hand side of the weir. Between $t = 20\,000$ s and $t = 28\,000$ s the southern boundary of the large cluster at the orographic left hand side remained stable and coincided well with the wet patch shown in Figure 2.7. This indicates that the subsurface water flow is locally impeded by the clay wall. However, water finally flows over the clay wall and causes the observed moisture pattern on the soil surface (Section 2.4.2). Finally, after 28 000 s the large cluster connected to the lake basin area.

By investigating the time series of subsurface flow path evolution shown in Figure 5.7, it appeared that the lake-near part of the catchment generally connected considerably less easily than the area upslope from the wall. The reasons for this are the shallow soil depths near the lake resulting in a lower chance of flow path connection and the generally lower hydraulic gradients due to the rather flat area. Additionally, the clay wall acts as a barrier for lateral flow.

The cumulated subsurface outflow to the lake basin is displayed in Figure 5.5 for both simulations. The erosion rills had no impact on subsurface outflow almost until the end of the rainfall event. Thereafter, the subsurface outflow for the simulation including the rills remained slightly lower than for the simulation without rills. This is not surprising, since less water elements infiltrated in the simulation including the rills (as discussed in Section 5.4.1). Thus, on the one hand less water elements were available for subsurface runoff and on the other hand the soil remained somewhat drier and thus less conductive. The subsurface flow did not reach equilibrium until the end of the simulations.

5.5 Discussion

5.5.1 Practicability of the new model concept

The new model uses similar approaches to describe water transport as hydrological cellular automata models describing stream channel flow (e.g. Murray and Paola, 1994; Thomas and Nicholas, 2002; Parsons and Fonstad, 2007; Rinaldi et al., 2007) or subsurface flow (e.g. Mendicino et al., 2006). But instead of focussing only on a certain flow process the new model presented in this chapter connects the processes of rainfall, infiltration, surface runoff and soil water flow and allows a more comprehensive hydrological perception of the water flows in the catchment. However, the main difference to current cellular automata models is the discretisation of the rainfall acting as model input into 'water elements' and the introduction of the 'potential water transport capability' to use the discrete water elements with non-discrete physically-based flow equations. The idea of describing water flows with discrete units is not new. A special case of cellular automata models to model water flow are lattice gas models that were applied as well for modelling subsurface flow (e.g. Di Pietro et al., 1994). But while the discretisation of water volumes in lattice gas models (or expressing water density distributions in a discrete set of velocities as in lattice Boltzmann models, e.g. Pan et al., 2004) usually aims to describe water flow in agreement with Navier–Stokes solutions (a lattice Boltzmann approach to the Richards equation was propsed by Ginzburg et al., 2004), the water flow in our model is governed by Darcy flow.

The new hydrological model concept is attractive, since the description of runoff processes, the calculation of water transit times and the emergence of macro-scale structures all can be represented in the same model framework. The temporal resolution of model simulations is not restricted to single rainfall events. If the required computational resources are provided the model can also be used to simulate time series of multiple events, especially because the discretisation into single elements is optimal for parallel computing. Additionally, the model approach is very flexible and may be expanded easily by further processes including spatiotemporal changes of model variables, for example the colonisation of unvegetated areas by plants and the accompanied change of evapotranspiration. The high computational expenses originating from the high spatial and temporal resolution of the model can be compensated by the possibility of parallel programming utilising the explicit nature of the described numerical schemes.

The focus of the study was, in the first instance, on testing the feasibility of the new model concept to reproduce runoff processes, transit times, and the emergence of hydrologically relevant structures at the macro-scale. The results presented in Section 5.4 demonstrated that the model is able to simulate reasonable surface and subsurface flow patterns as well as distance-time relationships of water elements flowing along the catchment surface. So far, we analysed transit times for surface flow only but the tracking of any flow path of a water element is straightforward. Furthermore, the model was able to capture differences in the flow regime and flow structures between the simulation based on the initial surface topography and the simulation including the erosion rill network. These are valuable factors for demonstrating the role of surface evolution on catchment hydrology. However, in the current version of the model there are still a number of open issues, which are discussed in the next section.

5.5.2 Open issues concerning the current model state

5.5.2.1 Subsurface flow

The soil physical properties randomly scattered in the simulated catchment determine the spatial and temporal development of subsurface flow patterns. In this chapter only a single realisation of the distribution of soil physical properties was analysed. However, the study of a set of multiple simulations with different realisations would be required to investigate if macro-scale flow patterns are independent of the distribution of soil physical properties. It is expected that, similar to the PT model, different realisations alter flow paths locally, but that the macro-scale characteristics of the flow patterns change only marginally.

The initial water content in the catchment was set to field capacity for the lowest model grid cell in the soil column and decreased for the cells above according to a linear function. The groundwater body, which was observed to develop immediately after the completion of the catchment (Mazur et al., 2011), was not considered in the simulation. The overall low water content in the simulated catchment, the disregard of groundwater and the relatively low hydraulic conductivities determined by the software 'Rosetta' (Schaap et al., 2001) are reflected in the very low simulated subsurface outflow to the lake basin. For both simulations, with and without rills, only about 2 % of the measured total outflow (213 m^3) were calculated as subsurface outflow (total simlated outflow accounted for about 5 % in case of no rills and 10 % when rills were included). Under these boundary conditions most of the precipitation infiltrating at the surface is stored in the soil and effective subsurface water flow occurred only rarely, since soil water contents seldom exceeded the free water capacity threshold. For the simulation of realistic outflow quantities the initial groundwater body and groundwater flow have to be included in the model.

5.5.2.2 Surface flow

The amount of simulated surface runoff is largely a function of f, the reduction factor of the saturated hydraulic conductivity at the surface. The low value of $f = 1/5000$ had to be chosen in order to reproduce similar surface flow patterns as described in Section 4.3.1. Even though a fairly low f was applied for the simulations, only a very small amount of rainfall flowed off as surface runoff (0.3 % for the simulation without rills and 1 % for the simulation with rills). The causes for the apparently massively reduced saturated hydraulic conductivity at the surface of the Chicken Creek catchment are not fully identified yet. Possible explanations are the intense compaction of the surface during the construction works of the catchment, the effect of hydrophobic biocrusts and the clogging of soil pores by sediment aggradation.

5.5.2.3 Validation against measurements

The main goal of this section study was to develop a prototype of a model to track water flow paths at complex surfaces after intense rainfall events. The successful test of the simulation results against observed surface flow path structures and qualitative characteristics, such as soil wetness patterns, were first indicators of the validity of the model. After embedding adequate flow processes and initial conditions for the groundwater, it will, of course, be necessary to relate the simulation results also to further measured data, such as total catchment outflow or surface runoff. The quality of the model can only be fully assessed by comparing such measurements for several rainfall events with simulation results.

5.5.2.4 Effect of discretisation

To account for the spatial heterogeneity of soil physical properties, surface and subsurface topography, and to justify the application of small-scale physical equations, the catchment must be discretised into a grid of high resolution. A three-dimensional orthogonal model grid of 0.5 m resolution was used and subsequently modified to a face-centred cubic lattice. The resolution was small enough to produce reasonable flow patterns on the surface and in the soil. However, to assure the independence of the development of these patterns from the model grid resolution and structure, simulations with lower resolutions would be required.

The discretisation of rainfall into water elements also has an effect on the water flows. The predefined volume of the water elements mainly affects the timing of water flow. The larger the size of a water element is chosen, the longer it takes until a water element can be built from rainfall and then be infiltrated or transported. Due to the introduction of the potential water flow capabilities, which are based on non-discrete physical equations, the total amount of water flow at a location (x, y, z) is less affected by the discretisation.

Generally, it can be concluded that the higher the model grid resolution and the smaller the volume of the water elements the more accurate the simulation results. However, the high simulation accuracy is only achieved at the expense of computer processing time, and thus a trade-off between acceptable processing time and high simulation reliability has to be made.

5.6 Summary

A new model framework was conceptualised to describe water flow at the catchment scale, transit times of water volumes, and the evolution of hydrologically relevant macro-scale patterns emerging from small-scale processes. Water flow in the new model is based on the combination of well-established physical equations, concepts of Percolation Theory, and the relocation of discrete volume units called ‘water elements’. The link between the equations describing non-discrete water flows and the discrete transport of the water elements is done by introducing the concept of ‘potential water transport capability’. The main aim of this chapter was to test the general feasibility of this model prototype and to assess first results concerning the hydrological effects of the surface erosion rills.

Based on the discrete flow of water elements generated from rainfall the model managed to reproduce surface flow structures and to simulate the temporal development of macro-scale subsurface flow patterns. The relationship between surface flow distance and time used to cover this path (i.e. the surface flow velocity) could be determined for each water element flowing along the catchment surface. Depending on the presence or absence of erosion rills, distinct differences in the surface flow regime could be detected. Flow paths of water elements along initial surface topography without erosion rills were generally shorter than for the simulation including the erosion rills. In the presence of rills, the characteristic surface flow velocity of the water elements was four times higher than for surface water flows along the initial topography without rills. Total surface outflow was about three times higher in the presence of rills. In contrast to surface flow patterns, total subsurface water flow was much less affected by the erosion rills. However, due to the generally low initial water contents chosen for this set of simulations and the disregard of the initial groundwater body, the simulated outflow values were clearly underestimated with the model. To simulate realistic outflow quantities the initial conditions in the model have to be adapted and groundwater flow has to be considered adequately.

6 Future work in the light of current issues in hydrological catchment modelling

6.1 Modelling hydrological processes

For many hydrological issues (e.g. flood prediction, water management for hydropower generation) the measure of total catchment runoff is of major interest. Total runoff, integrating all within catchment processes to a single signal, has been simulated with a variety of different hydrological models with some success (Singh and Frevert, 2002). However, many models estimate total runoff without thoroughly understanding the internal catchment processes. It is often assumed that the processes are correct if total runoff is reasonably accurate at some scale (Sidle, 2006). Although a variety of processes contributing to catchment runoff were suggested (e.g. infiltration excess overland flow, saturation excess overland flow, subsurface stormflow, macropore flow), there is still no consensus on the general hydrological 'functioning' of catchments.

With this thesis we added further insights into the internal hydrological processes of a man-made catchment. The difficulty of understanding the flow processes in a catchment is related to the highly complex nature of unsaturated soils. To represent this high complexity in the models (Chapter 3 and Chapter 5) a low model grid resolution was chosen and soil hydraulic properties based on a manifold of soil texture measurements were ascribed to the grid cells. The investigations have shown that the state of hydraulic connectivity of soil elements and the evolution of the erosion rills were essentially governed by micro-scale processes and conditions (e.g. hillslope geometry, soil depths, surface runoff) in the catchment. Furthermore, first simulations with the new model described in Chapter 5 indicated that the consideration of evolving erosion rills has a considerable impact on the spatial distribution of infiltration and on the amount of surface runoff. The future consideration of groundwater flow in the new model is indispensable to simulate the catchment outflow in the correct order of magnitude. Thereafter, several objectives will be investigated. For example, the effect of erosion rills on catchment runoff and on surface and subsurface flow paths, the ability of the model to reproduce both, regular low flow conditions and the threshold-like rainfall-runoff behaviour of the catchment, and the characteristic transit times of surface and subsurface water.

6.2 Application of small-scale equations

The representation of a small spatial scale is important not only with respect to data, but also to process descriptions in the model. This became evident when simulating the hydrologic connectivity and the evolution of erosion rills in the catchment. Most of the distributed hydrological models are based on water transport described by the Richards equation or the Buckingham–Darcy equation. The application of these small-scale nonlinear descriptions of water fluxes at the scale usually used in hydrological modelling (say 10 m – 1000 m) is questionable (Beven, 2001). Richards equation was used for so long only because it is consistent with the measurement scales of soil physical measurements (Beven, 2001).

In contrast to most experimental catchments much information on the soil of the Chicken Creek catchment is available. The many soil texture probes have shown that soil heterogeneity is relatively low compared to mature natural catchments. Macropores due to faunal activities (e.g. earthworm pipes or animal burrows) or a dense plant root network were considered to be negligible in the initial phase of catchment development. Additionally, the lower boundary (clay layer) was well characterised in terms of substrate and the topographies (subsurface and surface) were described by a high resolution Digital Elevation Model. Due to the relatively undisturbed soil and the knowledge of the boundary conditions, the application of the Buckingham–Darcy equation is justified in the high-resolution model developed in Chapter 5. Furthermore, the model will constitute a valuable test of the general applicability of the Darcy equation in catchment hydrology.

6.3 Model validation

It is difficult to verify the processes actually dominating the water fluxes of a catchment. This is mainly because there is still no technique available to directly measure subsurface water fluxes in the field (Beven, 2006). This poses a major problem for hydrological modelling, because the governing flow processes included in a model cannot be validated and remain uncertain to a considerable degree. There is a need for new measurement methods to provide spatially distributed data on subsurface water fluxes at the appropriate scale. The alternative to using direct measurements is inferring the required information from indirect measurements. For example, information on soil water flows was inferred from the dynamic patterns of soil water content sampled by repeated Ground-Penetrating Radar (GPR) (Gish et al., 2002; Huisman et al., 2002; Lunt et al., 2005) or subsurface electrical resistance (ERT) measurements (Samouëlian et al., 2005; Vanderborght et al., 2005), or from saturation levels measured in a dense spatial network of piezometers (Tromp-van Meerveld and McDonnell, 2006; Lehmann et al., 2007). The geochemical characterisation of different water sources (Kendall and McDonnell, 1998) is another promising tool to improve our understanding of subsurface flows. The adequate spatial sampling of data with these techniques allows a powerful test of distributed modelling capabilities as they can provide valuable information on water flow processes or constrain the model prediction uncertainties (e.g. Bronstert and Plate, 1997; Houser et al., 2001; Western and Grayson, 2001).

It will be of major importance to compare the simulation results of the new model (Chapter 5) with field observations from the catchment. Unfortunately, there are no data from geophysical methods available covering the entire catchment. However, single ERT measurements were made, but only at a few points in time and space. Additionally, groundwater level data from 17 observation wells, soil moisture data taken at six depths at 16 points in the catchment, surface runoff data from two flumes installed in erosion rills and total catchment runoff data are now available. These data provide a decent degree of spatial information on hydrological variables to validate the new model.

6.4 Model uncertainty

A further issue in hydrological modelling is the assessment of the uncertainty of model results. In this context, the principle of equifinality was widely discussed in the scientific literature in the last few years (e.g. Beven and Freer, 2001; Todini, 2007). Equifinality refers to more than one parameter set providing an equally good (or poor) representation of the integrated response (Ebel and Loague, 2006). To investigate the related uncertainties of model results frameworks for uncertainty estimation have been developed, such as Markov Chain Monte Carlo simulations (Vrugt et al., 2008) or the Generalised Likelihood Uncertainty Estimation (Beven and Binley, 1992).

Many processes such as macropore flow or plant transpiration can be neglected in the initial phase of catchment development and thus the parameter space of a corresponding model is substantially reduced. This also means that the chance of equifinality is low and thus also the uncertainty of the model results. Additionally, using only a small set of parameters considerably decreases computer processing time for uncertainty estimation. Besides the uncertainty analysis of model results, a thorough study of the model sensitivity regarding model architecture is also needed to assure that the simulation results are fully independent of the chosen model grid resolution and cell neighbourhood. Such a test would additionally provide the information needed to specify the optimal relation between model grid resolution and computational expenses.

Following the above discussion, it becomes clear that there are still many issues and uncertainties in hydrological modelling. Nevertheless, models provide a helpful tool to test hypotheses, for example, on the dominant hydrological processes of a catchment. Kirkby (1996) pointed out that ‘the most important role of models is as a qualitative thought experiment, testing whether we have a sufficient and consistent theoretical explanation of physical processes’. In this sense, the simulation results achieved by the successful application of the new models developed in this thesis constitute a step forward in identifying, testing and understanding the theoretical concepts of the governing physical processes leading to hydrologically relevant structures in catchments.

References

Alberts, E. E., Nearing, M. A., Weltz, M. A., Risse, L. M., Pierson, F. B., Zhang, X. C., Laflen, J. M., and Simanton, J. R., 1995. Chapter 7: Soil component. In: Flanagan, D. and Nearing, M. A. (eds.), *U.S.D.A.-Water erosion prediction project - Hillslope profile and watershed model documentation*, West Lafayette, Indiana, USA, vol. NSERL Report No. 10.

Amos, C. L., Daborn, G. R., Christian, H. A., Atkinson, A., and Robertson, A., 1992. In situ erosion measurements on fine-grained sediments from the Bay of Fundy. *Marine Geology*, **108**, 175–196.

Arnell, N., 2002. *Hydrology and global environmental change.* Pearson Education, Essex, UK.

Ascough, J. C., Baffaut, C., Nearing, M. A., and Liu, B. Y., 1997. The WEPP watershed model: I. Hydrology and erosion. *Transactions of the ASAE*, **40**(4), 921–933.

Barling, R. D., Moore, I. D., and Bryan, R. B., 1994. A quasi-dynamic wetness index for characterizing the spatial distribution of zones of surface saturation and soil water content. *Water Resources Research*, **30**(4), 1029–1044.

Bates, B. C., Kundzewicz, Z. W., Wu, S., and Palutikof, J. P. (eds.), 2008. *Climate Change and Water. Technical Paper of the Intergovernmental Panel on Climate Change.* IPCC Secretariat, Geneva.

Beven, K., 2001. Dalton Medal Lecture: How far can we go in distributed hydrological modelling? *Hydrology and Earth System Sciences*, **5**(1), 1–12.

Beven, K. (ed.), 2006. *Streamflow Generation Processes: Benchmark Papers in Hydrology.* IAHS Press, Wallingford, UK.

Beven, K. and Binley, A., 1992. The future of distributed models: Model calibration and uncertainty prediction. *Hydrological Processes*, **6**, 279–298.

Beven, K. and Freer, J., 2001. Equifinality, data assimilation, and uncertainty estimation in mechanistic modelling of complex environmental systems using the GLUE methodology. *Journal of Hydrology*, **249**(1-4), 11–29.

Beven, K. and Kirkby, M. J., 1979. A physically based, variable contributing area model of basin hydrology. *Hydrological Sciences Bulletin*, **24**, 43–69.

Biemelt, D., Schapp, A., Kleeberg, A., and Grünewald, U., 2005. Overland flow, erosion, and related phosphorus and iron fluxes at plot scale: a case study from a non-vegetated lignite mining dump in Lusatia. *Geoderma*, **129**, 4–18.

Bobrovitskaya, N. N. and Vorozhbitov, I. I., 1979. Investigation of the temporary rill network by aerial methods. *Soviet Hydrology: Selected Papers*, **18**(4), 270–274.

Bracken, L. J. and Croke, J., 2007. The concept of hydrological connectivity and its contribution to understanding runoff-dominated geomorphic systems. *Hydrological Processes*, **21**, 1749–1763.

Bradford, J. M. and Grossman, R. B., 1982. In-situ measurement of near-surface soil strength by the fall-cone device. *Soil Science Society of America Journal*, **46**, 685–688.

Broadbent, S. R. and Hammersley, J. M., 1957. Percolation processes I. Crystals and mazes. *Proceedings Of The Cambridge Philosophical Society*, **53**(3), 629–641.

Bronstert, A. and Bárdossy, A., 1999. The role of spatial variability of soil moisture for modelling surface generation at the small catchment scale. *Hydrology and Earth System Sciences*, **3**(4), 505–516.

Bronstert, A. and Plate, E. J., 1997. Modelling of runoff generation and soil moisture dynamics for hillslopes and micro-catchments. *Journal of Hydrology*, **198**(1-4), 177–195.

Brunton, D. A. and Bryan, R. B., 2000. Rill network development and sediment budgets. *Earth Surface Processes and Landforms*, **25**, 783–800.

Bryan, R. B. and Poesen, J., 1989. Laboratory experiments on the influence of slope length on runoff, percolation and rill development. *Earth Surface Processes and Landforms*, **14**, 211–231.

Buttle, J., 1994. Isotope hydrograph separations and rapid delivery of pre-event water from drainage basins. *Progress in Physical Geography*, **18**(1), 16–41.

Chaplot, V., Coadou le Brozec, E., Silvera, N., and Valentin, C., 2005. Spatial and temporal assessment of linear erosion in catchments under sloping lands of northern Laos. *Catena*, **63**(2-3), 167–184.

Chatzis, I. and Dullien, F. A. L., 1977. Modelling pore structure by 2-D and 3-D networks with applications to sandstones. *Journal of Canadian Petroleum Technology*, **16**(1), 97–108.

Daba, S., Rieger, W., and Strauss, P., 2003. Assessment of gully erosion in eastern Ethiopia using photogrammetric techniques. *Catena*, **50**(2-4), 273–291.

de Linares, M. and Belleudy, P., 2007. Critical shear stress of bimodal sediment in sand-gravel rivers. *Journal of Hydraulic Engineering*, **133**(5), 555–559.

Desmet, P. J. J. and Govers, G., 1997. Two-dimensional modelling of the within-field variation in rill and gully geometry and location related to topography. *Catena*, **29**, 283–306.

Di Pietro, L. B., Melayah, A., and Zaleski, S., 1994. Modeling water infiltration in unsaturated porous media by interacting lattice gas-cellular automata. *Water Resources Research*, **30**(10), 2785–2792.

Dingman, S. L., 2008. *Physical Hydrology.* Waveland Press, Inc., Long Grove, Illinois, 2 ed.

Ebel, B. A. and Loague, K., 2006. Physics-based hydrologic-response simulation: Seeing through the fog of equifinality. *Hydrological Processes*, **20**(13), 2887–2900.

Einstein, H., 1950. The bed-load function for sediment transportation in open channel flow. *Technical Bulletin No. 1026, U.S. Department of Agriculture*, Washington, D.C.

Ewing, R. P. and Gupta, S. C., 1993. Modeling percolation properties of random media using a domain network. *Water Resources Research*, **29**(9), 3169–3178.

Fairfield, J. and Leymarie, P., 1991. Drainage networks from grid digital elevation models. *Water Resources Research*, **27**(5), 709–717.

Favis-Mortlock, D., 1998. A self-organizing dynamic systems approach to the simulation of rill initiation and development on hillslopes. *Computers & Geosciences*, **24**(4), 353–372.

Favis-Mortlock, D. T., Boardman, J., Parsons, A. J., and Lascelles, B., 2000. Emergence and erosion: a model for rill initiation and development. *Hydrological Processes*, **14**, 2173–2205.

Freer, J., Mcdonnell, J. J., Beven, K., Brammer, D., Burns, D., Hooper, R. P., and Kendall, C., 1997. Topographic controls on subsurface storm flow at the hillslope scale for two hydrologically distinct small catchmetns. *Hydrological Processes*, **11**(9), 1347–1352.

Freer, J., McDonnell, J. J., Beven, K., Peters, N. E., Burns, D. A., Hooper, R. P., Aulenbach, B., and Kendall, C., 2002. The role of bedrock topography on subsurface storm flow. *Water Resources Research*, **38**(12), 5/1–5/16.

Garrison, T., 2009. *Essentials of Oceanography.* Brooks/Cole, Cengage Learning, Belmont, CA, 5th ed. ed.

Gburek, W. J. and Folmar, G. J., 1999. A groundwater recharge field study: site characterization and initial results. *Hydrological Processes*, **13**(17), 2813–2831.

Gerwin, W., Raab, T., Biemelt, D., Bens, O., and Hüttl, R. F., 2009a. The artificial water catchment "Chicken Creek" as an observatory for critical zone processes and structures. *Hydrology and Earth System Sciences Discussions*, **6**, 1769–1795.

Gerwin, W., Schaaf, W., Biemelt, D., Fischer, A., and Winter, S., 2009b. The artificial catchment "Chicken Creek" (Lusatia, Germany)–A landscape laboratory for interdisciplinary studies of initial ecosystem development. *Ecological Engineering*, **35**, 1786–1796.

Giménez, R. and Govers, G., 2001. Interaction between bed roughness and flow hydraulics in eroding rills. *Water Resources Research*, **37**(3), 791–799.

Giménez, R., Planchon, O., Silvera, N., and Govers, G., 2004. Longitudinal velocity patterns and bed morphology interaction in a rill. *Earth Surface Processes and Landforms*, **29**(1), 105–114.

Ginzburg, I., Carlier, J., and Kao, C., 2004. *Lattice Boltzmann approach to Richards' equation.* CMWR Proceedings, North Carolina, USA.

Gish, T. J., Dulaney, W. P., Kung, K. J. S., Daughtry, C. S. T., Doolittle, J. A., and Miller, P. T., 2002. Evaluating use of ground-penetrating radar for identifying subsurface flow pathways. *Soil Science Society of America Journal*, **66**, 1620–1629.

Govers, G., Giménez, R., and Van Oost, K., 2007. Rill erosion: Exploring the relationship between experiments, modelling and field observations. *Earth-Science Reviews*, **84**(3-4), 87–102.

Gumiere, S. J., Le Bissonnais, Y., and Raclot, D., 2009. Soil resistance to interrill erosion: Model parameterization and sensitivity. *Catena*, **77**(3), 274–284.

Gómez, J. A., Darboux, F., and Nearing, M. A., 2003. Development and evolution of rill networks under simulated rainfall. *Water Resources Research*, **39**(6), ESG 1/1–1/14.

Hairsine, P. B., Beuselinck, L., and Sander, G. C., 2002. Sediment transport through an area of net deposition. *Water Resources Research*, **38**(6), 22/1–22/7.

Hancock, G. R., Crawter, D., Fityus, S. G., Chandler, J., and Wells, T., 2008. The measurement and modelling of rill erosion at angle of repose slopes in mine spoil. *Earth Surface Processes and Landforms*, **33**(7), 1006–1020.

Hogan, J. F. and Blum, J. D., 2003. Tracing hydrologic flow paths in a small forested watershed using variations in 87Sr/86Sr, [Ca]/[Sr], [Ba]/[Sr] and δ18O. *Water Resources Research*, **39**(10), HWC 1/1–1/12.

Holden, J., 2004. Hydrological connectivity of soil pipes determined by ground-penetrating radar tracer detection. *Earth Surface Processes and Landforms*, **29**, 437–442.

Horton, R. E., 1945. Erosional development of streams and their drainage basins: hydro-physical approach to quantitative morphology. *Geological Society of America Bulletin*, **56**(3), 275–370.

Houser, P., Goodrich, D., and Syed, K., 2001. Runoff, Precipitation, and Soil Moisture at Walnut Gulch. In: *Spatial Patterns in Catchment Hydrology*, Cambridge University Press, Cambridge, UK.

Huang, C., Wells, L. K., and Norton, L. D., 1999. Sediment transport capacity and erosion processes: Model concepts and reality. *Earth Surface Processes and Landforms*, **24**, 503–516.

Huang, C., Gascuel-Odoux, C., and Cros-Cayot, S., 2001. Hillslope topographic and hydrologic effects on overland flow and erosion. *Catena*, **46**, 177–188.

Huisman, J., Snepvangers, J., Bouten, W., and Heuvelink, G., 2002. Mapping spatial variation in surface soil water content: comparison of ground-penetrating radar and time domain reflectometry. *Journal of Hydrology*, **269**(3-4), 194–207.

Hunt, A. G. and Ewing, R., 2009. *Percolation theory for flow in porous media.* Springer, Berlin, Heidelberg.

Jansson, P. and Karlberg, L., 2001. *Coupled heat and mass transfer model for soil-plant atmosphere systems. Model manual.* Royal Institute of Technology, Department of Civil and Environmental Engineering, Stockholm. (ftp://www.lwr.kth.se/CoupModel/CoupModel.pdf).

Jetten, V., de Roo, A., and Favis-Mortlock, D., 1999. Evaluation of field-scale and catchment-scale soil erosion models. *Catena*, **37**, 521–541.

Jetten, V., Govers, G., and Hessel, R., 2003. Erosion models: quality of spatial predictions. *Hydrological Processes*, **17**, 887–900.

Kendall, C. and McDonnell, J., 1998. *Isotope Tracers in Catchment Hydrology.* Elsevier Science, Amsterdam, the Netherlands.

Kendall, C., McDonnell, J. J., and Gu, W., 2001. A look inside 'black box' hydrograph separation models: a study at the Hydrohill catchment. *Hydrological Processes*, **15**(10), 1877–1902.

Kendzia, G., Reissmann, R., and Neumann, T., 2008. Targeted development of wetland habitats for nature conservation fed by natural inflow in the post-mining landscape of Lusatia. *World of Mining – Surface and Underground*, **60**(2), 88–95.

Kirchner, J. W., 2006. Getting the right answers for the right reasons: linking measurements, analyses, and models to advance the science of hydrology. *Water Resources Research*, **42**, W03S04.

Kirchner, J. W., Feng, X., and Neal, C., 2000. Fractal stream chemistry and its implications for contaminant transport in catchments. *Nature*, **403**, 524–527.

Kirkby, M. J., 1996. A Role for Theoretical Models in Geomorphology? In: Rhoads, B. L. and Thorn, C. E. (eds.), *The scientific nature of geomorphology: proceedings of the 27th Binghamton Symposium in Geomorphology, held 27-29 September, 1996*, John Wiley & Sons Ltd, Chichester, UK.

Knapen, A., Poesen, J., Govers, G., Gyssels, G., and Nachtergaele, J., 2007. Resistance of soils to concentrated flow erosion: A review. *Earth-Science Reviews*, **80**(1-2), 75–109.

Koenker, R., 2011. quantreg: Quatile Regression. R package version 4.67. http://CRAN.R-project.org/package=quantreg.

Kramer, S. and Marder, M., 1992. Evolution of river networks. *Physical Review Letters*, **68**(2), 205–208.

Leheny, R. L. and Nagel, S. R., 1993. Model for the evolution of river networks. *Physical Review Letters*, **71**(9), 1470–1473.

Lehmann, P., Hinz, C., McGrath, G., Tromp-van Meerveld, H. J., and McDonnell, J. J., 2007. Rainfall threshold for hillslope outflow: an emergent property of flow pathway connectivity. *Hydrology and Earth System Sciences*, **11**, 1047–1063.

Lehmann, P., Assouline, S., and Or, D., 2008. Characteristic lengths affecting evaporative drying of porous media. *Physical Review E*, **77**(5), 056309/1–056309/16.

Lemonds, P. J. and McCray, J. E., 2007. Modeling Hydrology in a Small Rocky Mountain Watershed Serving Large Urban Populations. *Journal of the American Water Resources Association*, **43**(4), 875–887.

Li, Z., Liu, W., Zhang, X., and Zheng, F., 2009. Impacts of land use change and climate variability on hydrology in an agricultural catchment on the Loess Plateau of China. *Journal of Hydrology*, **377**(1-2), 35–42.

Liu, M., Parlange, J., Sivapalan, M., and Brutsaert, W., 1998. A note on the time compression approximation. *Water Resources Research*, **34**(12), 3683–3686.

Lorenz, C. D. and Ziff, R. M., 1998. Universality of the excess number of clusters and the crossing probability function in three-dimensional percolation. *Journal of Physics A*, **31**, 8147–8157.

Lunt, I., Hubbard, S., and Rubin, Y., 2005. Soil moisture content estimation using ground-penetrating radar reflection data. *Journal of Hydrology*, **307**, 254–269.

Mazur, K., Schoenheinz, D., Biemelt, D., Schaaf, W., and Grünewald, U., 2011. Observation of hydrological processes and structures in the artificial Chicken Creek catchment. *Physics and Chemistry of the Earth, Parts A/B/C*, **36**(1-4), 74–86.

McDonnell, J. J., 2003. Where does water go when it rains? Moving beyond the variable source area concept of rainfall–runoff response. *Hydrological Processes*, **17**, 1869–1875.

McDonnell, J. J., Sivapalan, M., Vaché, K., Dunn, S., Grant, G., Haggerty, R., Hinz, C., Hooper, R., Kirchner, J., Roderick, M. L., Selker, J., and Weiler, M., 2007. Moving beyond heterogeneity and process complexity: A new vision for watershed hydrology. *Water Resources Research*, **43**, W07301.

McDonnell, J. J., McGuire, K., Aggarwal, P., Beven, K., Biondi, D., Destouni, G., Dunn, S., James, A., Kirchner, J., Kraft, P., Lyon, S., Maloszewski, P., Newman, B., Pfister, L., Rinaldo, A., Rodhe, A., Sayama, T., Seibert, J., Solomon, K., Soulsby, C., Stewart, M., Tetzlaff, D., Tobin, C., Troch, P., Weiler, M., Western, A., Wörman, A., and Wrede, S., 2010. How old is streamwater? Open questions in catchment transit time conceptualization, modelling and analysis. *Hydrological Processes*, **24**(12), 1745–1754.

McGuire, K., Weiler, M., and McDonnell, J., 2007. Integrating tracer experiments with modeling to assess runoff processes and water transit times. *Advances in Water Resources*, **30**(4), 824–837.

Mendicino, G., Senatore, A., Spezzano, G., and Straface, S., 2006. Three-dimensional unsaturated flow modeling using cellular automata. *Water Resources Research*, **42**, W11419.

Mercier, C. and Delhez, E. J. M., 2007. Diagnosis of the sediment transport in the Belgian Coastal Zone. *Estuarine, Coastal and Shelf Science*, **74**, 670–683.

Merz, B. and Plate, E. J., 1997. An analysis of the effects of spatial variability of soil and soil moisture on runoff. *Water Resources Research*, **33**(12), 2909–2922.

Meyer-Peter, E. and Müller, R., 1948. Formulas for bed-load transport. In: *Proceedings, 2nd Congress International Association for Hydraulic Research*, Rotterdam, the Netherlands, 39–64.

Mimura, N., 1993. Rates of erosion and deposition of cohesive sediments under wave action. In: Mehta, A. J. (ed.), *Coastal and estuarine studies - Nearshore and estuarine cohesive sediment transport*, American Geophysical Union, Washington, DC.

Mitchener, H. and Torfs, H., 1996. Erosion of mud/sand mixtures. *Coastal Engineering*, **29**, 1–25.

Mouzai, L. and Bouhadef, M., 2011. Shear strength of compacted soil: effects on splash erosion by single water drops. *Earth Surface Processes and Landforms*, **36**, 87–96.

Murray, A. B. and Paola, C., 1994. A cellular model of braided rivers. *Nature*, **371**(6492), 54–57.

Nearing, M. A., Norton, L. D., Bulgakov, D. A., Larionov, G. A., West, L. T., and Dontsova, K. M., 1997. Hydraulics and erosion in eroding rills. *Water Resources Research*, **33**(4), 865–876.

Nicolau, J., 2002. Runoff generation and routing on artificial slopes in a Mediterranean–continental environment: the Teruel coalfield, Spain. *Hydrological Processes*, **16**(3), 631–647.

Nyberg, L., 1995. Water flow path interactions with soil hydraulic properties in till soil at Gårdsjön, Sweden. *Journal of Hydrology*, **170**, 255–275.

O'Callaghan, J. F. and Mark, D. M., 1984. The extraction of drainage networks from digital elevation data. *Computer Vision, Graphics, and Image Processing*, **28**, 323–344.

Ocampo, C. J., Sivapalan, M., and Oldham, C. E., 2006. Field exploration of coupled hydrological and biogeochemical catchment responses and a unifying conceptual model. *Advances in Water Resources*, **29**, 161–180.

Pachepsky, Y. A., Rawls, W. J., and Lin, H. S., 2006. Hydropedology and pedotransfer functions. *Geoderma*, **131**(3-4), 308–316.

Pan, C., Hilpert, M., and Miller, C. T., 2004. Lattice-Boltzmann simulation of two-phase flow in porous media. *Water Resources Research*, **40**, W01501.

Papanicolaou, A. N., Sanford, J. T., Dermisis, D. C., and Mancilla, G. A., 2010. A 1-D morphodynamic model for rill erosion. *Water Resources Research*, **46**, W09541.

Parker, G., 1979. Hydraulic geometry of active gravel rivers. *Journal of the Hydraulics Division*, **105**(9), 1185–1201.

Parlange, J., 1975. On solving the Flow Equation in Unsaturated Soils by Optimization: Horizontal Infiltration. *Soil Science Society of America Journal*, **39**(3), 415–418.

Parsons, A. J., Wainwright, J., Abrahams, A. D., and Simanton, J. R., 1997. Distributed dynamic modelling of interrill overland flow. *Hydrological Processes*, **11**, 1833–1859.

Parsons, J. A. and Fonstad, M. A., 2007. A cellular automata model of surface water flow. *Hydrological Processes*, **21**, 2189–2195.

Partheniades, E., 1977. Unified view of wash load and bed material load. *Journal of the Hydraulics Division*, **103**(9), 1037–1057.

Philip, J. R., 1957. The Theory of Infiltration: 1. the Infiltration Equation and its Solution. *Soil Science*, **83**(5), 345–358.

Planchon, O. and Darboux, F., 2001. A fast, simple and versatile algorithm to fill the depressions of digital elevation models. *Catena*, **46**, 159–176.

Planchon, O. and Mouche, E., 2010. A Physical Model for the Action of Raindrop Erosion on Soil Microtopography. *Soil Science Society of America Journal*, **74**(4), 1092–1103.

Planchon, O., Esteves, M., Silvera, N., and Lapetite, J., 2000. Raindrop erosion of tillage induced microrelief: possible use of the diffusion equation. *Soil and Tillage Research*, **56**, 131–144.

Poesen, J., 1984. The influence of slope angle on infiltration rate and Hortonian overland flow volume. *Zeitschrift für Geomorphologie N.F. Supplement-Band*, **49**, 117–131.

Poesen, J., Nachtergaele, J., Verstraeten, G., and Valentin, C., 2003. Gully erosion and environmental change: importance and research needs. *Catena*, **50**, 91–133.

Prestrud Anderson, S., Dietrich, W. E., Montgomery, D. R., Torres, R., Conrad, M. E., and Loague, K., 1997. Subsurface flow paths in a steep, unchanneled catchment. *Water Resources Research*, **33**(12), 2637–2653.

Richards, L. A., 1931. Capillary conduction of liquids through porous mediums. *Physics*, **1**, 318–333.

Richey, D. G., McDonnell, J. J., Erbe, W. E., and Todd, M. H., 1998. Hydrograph separations based on chemical and isotopic concentrations: a critical appraisal of published studies from New Zealand, North America and Europe. *Journal of Hydrology (NZ)*, **37**(2), 95–111.

Rigby, J., 2009. *Intermittency and Irreversibility in the Soil-Plant-Atmosphere System*. Duke University, Durham (USA). Dissertation.

Rinaldi, P. R., Dalponte, D. D., Vénere, M. J., and Clausse, A., 2007. Cellular automata algorithm for simulation of surface flows in large plains. *Simulation Modelling Practice and Theory*, **15**(3), 315–327.

Rinaldo, A., Rodríguez-Iturbe, I., Rigon, R., Ijjasz-Vasquez, E., and Bras, R. L., 1993. Self-organized fractal river networks. *Physical Review Letters*, **70**(6), 822–825.

Rodríguez-Iturbe, I. and Rinaldo, A., 1997. *Fractal river basins: Chance and self-organization*. Cambridge University Press, Cambridge.

Rodríguez-Iturbe, I., Rinaldo, A., Rigon, R., Bras, R. L., Marani, A., and Ijjasz-Vasquez, E., 1992. Energy dissipation, runoff production, and the three-dimensional structure of river basins. *Water Resources Research*, **28**(4), 1095–1103.

Rodríguez-Iturbe, I., Marani, M., Rigon, R., and Rinaldo, A., 1994. Self-organized river basin landscapes: Fractal and multifractal characteristics. *Water Resources Research*, **30**(12), 3531–3539.

Rose, C. W., Williams, J. R., Sander, G. C., and Barry, D. A., 1983. A mathematical model of soil erosion and deposition processes: I. Theory for a plane land element. *Soil Science Society of America Journal*, **47**, 991–995.

Ruckstuhl, A., Unternaehrer, T., and Locher, R., 2010. IDPmisc: Utilities of Institute of Data Analyses and Process Design. R package version 1.1.10. http://CRAN.R-project.org/package=IDPmisc.

Sahimi, M., 1994. *Applications of percolation theory.* Taylor & Francis, London.

Samouëlian, A., Cousin, I., Tabbagh, A., Bruand, A., and Richard, G., 2005. Electrical resistivity survey in soil science: a review. *Soil and Tillage Research*, **83**(2), 173–193.

Schaap, M. G., Leij, F. J., and van Genuchten, M. T., 2001. ROSETTA: a computer program for estimating soil hydraulic parameters with hierarchical pedotransfer functions. *Journal of Hydrology*, **251**(3), 163–171.

Scheffer, F. and Schachtschabel, P., 2002. *Lehrbuch der Bodenkunde.* Spektrum Akademischer Verlag, Heidelberg.

Schneider, A., Gerke, H. H., and Maurer, T., 2011. 3D initial sediment distribution and quantification of mass balances of an artificially-created hydrological catchment based on DEMs from aerial photographs using GOCAD. *Physics and Chemistry of the Earth, Parts A/B/C*, **36**(1-4), 87–100.

Shields, A., 1936. Application of similarity principles and turbulence research to bed-load movement. *Mitteilungen der Preussischen Versuchsanstalt für Wasserbau und Schiffbau*, Berlin.

Sidle, R. C., 2006. Field observations and process understanding in hydrology: essential components in scaling. *Hydrological Processes*, **20**(6), 1439–1445.

Silliman, S. E., 1990. The influence of grid discretization on the percolation probability within discrete random fields. *Journal of Hydrology*, **113**, 177–191.

Silliman, S. E. and Wright, A. L., 1988. Stochastic analysis of paths of high hydraulic conductivity in porous media. *Water Resources Research*, **24**, 1901–1910.

Simpson, G. and Schlunegger, F., 2003. Topographic evolution and morphology of surfaces evolving in response to coupled fluvial and hillslope sediment transport. *Journal of Geophysical Research*, **108**(B6), ETG 7/1–7/16.

Singh, V. P. and Frevert, D. K. (eds.), 2002. *Mathematical models of large watershed hydrology*. Water Resources Publication, LLC, Highlands Ranch, Colorado.

Sivapalan, M., Beven, K., and Wood, E. F., 1987. On hydrologic similarity: 2. A scaled model of storm runoff production. *Water Resources Research*, **23**(12), 2266–2278.

Sivapalan, M., Takeuchi, K., Franks, S. W., Gupta, V. K., Karambiri, H., Lakshmi, V., Liang, X., McDonnell, J. J., Mendiondo, E. M., O'Connell, P. E., Oki, T., Pomeroy, J. W., Schertzer, D., Uhlenbrook, S., and Zehe, E., 2003. IAHS Decade on Predictions in Ungauged Basins (PUB), 2003-2012: Shaping an exciting future for the hydrological sciences. *Hydrological Sciences Journal*, **48**(6), 857–880.

Slattery, M. C. and Bryan, R. B., 1992. Hydraulic conditions for rill incisoion under simulated rainfall: A laboratory experiment. *Earth Surface Processes and Landforms*, **17**, 127–146.

Soil Science Society of America, 2008. Glossary of Soil Science Terms. Soil Science Society of America, Madison, WI, https://www.soils.org/publications/soils-glossary#.

Spence, C. and Woo, M. K., 2003. Hydrology of subartic Canadian Shield: soil-filled valleys. *Journal of Hydrology*, **279**, 151–166.

Stauffer, D. and Aharony, A., 1992. *Introduction to percolation theory*. Taylor & Francis, London.

Stieglitz, M., Shaman, J., McNamara, J., Engel, V., Shanley, J., and Kling, G. W., 2003. An approach to understanding hydrologic connectivity on the hillslope and the implications for nutrient transport. *Global Biogeochemical Cycles*, **17**(4), 16/1–16/15.

Strahler, A. N., 1957. Quantitative analysis of watershed geomorphology. *Transactions of the American Geophysical Union*, **8**(6), 913–920.

Takken, I., Jetten, V., Govers, G., Nachtergaele, J., and Steegen, A., 2001. The effect of tillage-induced roughness on runoff and erosion patterns. *Geomorphology*, **37**, 1–14.

Thomas, R. and Nicholas, A. P., 2002. Simulation of braided river flow using a new cellular routing scheme. *Geomorphology*, **43**(3-4), 179–195.

Todini, E., 2007. Hydrological catchment modelling: past, present and future. *Hydrology and Earth System Sciences*, **11**(1), 468–482.

Torri, D., Sfalanga, M., and Chisci, G., 1987. Threshold conditions for incipient rilling. *Catena Supplement*, **8**, 97–105.

Tromp-van Meerveld, H. J. and McDonnell, J. J., 2006. Threshold relations in subsurface stormflow: 2. The fill and spill hypothesis. *Water Resources Research*, **42**, W02411.

van Genuchten, M. T., 1980. A closed-form equation for predicting the hydraulic conductivity of unsaturated soils. *Science Society of America Journal*, **44**, 892–898.

Vanderborght, J., Kemna, A., Hardelauf, H., and Vereecken, H., 2005. Potential of electrical resistivity tomography to infer aquifer transport characteristics from tracer studies: A synthetic case study. *Water Resources Research*, **41**, W06013.

Vogel, H., Hoffmann, H., and Roth, K., 2005. Studies of crack dynamics in clay soil: I. Experimental methods, results, and morphological quantification. *Geoderma*, **125**, 203–211.

Vrugt, J. A., Braak, C. J. F., Gupta, H. V., and Robinson, B. A., 2008. Equifinality of formal (DREAM) and informal (GLUE) Bayesian approaches in hydrologic modeling? *Stochastic Environmental Research and Risk Assessment*, **23**, 1011–1026.

Watson, A. and Evans, R., 1991. A comparison of estimates of soil erosion made in the field and from photographs. *Soil and Tillage Research*, **19**(1), 17–27.

Waythomas, C. F., Scott, W. E., and Nye, C. J., 2010. The Geomorphology of an Aleutian Volcano following a Major Eruption: the 7–8 August 2008 Eruption of Kasatochi Volcano, Alaska, and Its Aftermath. *Arctic, Antarctic, and Alpine Research*, **42**(3), 260–275.

Weiler, M. and Naef, F., 2003. An experimental tracer study of the role of macropores in infiltration in grassland soils. *Hydrological Processes*, **17**(2), 477–493.

Western, A. and Grayson, R., 2001. Soil Moisture and Runoff Processes at Tarrawarra. In: *Spatial Patterns in Catchment Hydrology*, Cambridge University Press, Cambridge, UK.

Zobeck, T. M. and Onstad, C. A., 1987. Tillage and rainfall effects on random roughness: A review. *Soil and Tillage Research*, **9**, 1–20.

Curriculum vitae

Educational background

Jan 2012 – present	Swiss Federal Research Institute WSL, Switzerland Temporary employment (30 %) in the Research Unit *Mountain Hydrology and Mass Movements*
Sept 2007 – present	Teaching diploma for secondary education, University of Zurich, Switzerland
Sept 2007 – Dec 2011	**PhD** (rer. nat.), Technische Universität Braunschweig, Germany
Oct 2001 – Jun 2007	**MSc in Geography**, University of Zurich, Switzerland (main subject) Thesis: *Water fluxes along a boreal hillslope in northern Sweden under current and possible future climate conditions* **Geobotany** at the ETH Zurich, Switzerland (first minor subject) **Forest sciences** at the ETH Zurich, Switzerland (second minor subject)
Sept 2004 – Jun 2005	Geography, University of Sheffield, United Kingdom One-year study exchange supported by the European Union's education and training program *Erasmus*
Feb – Mar 2004	Swiss Federal Research Institute WSL, Switzerland Six-week practical training in the Research Unit *Ecological Genetics*
Aug 1995 – Jan 2000	High School at Kantonsschule Enge in Zurich, Switzerland

Work experience

Aug 2005 – Jul 2007	Swiss Economic Institute KOF, ETH Zurich, Switzerland Part-time job (50 %) in the secretariat
Nov 2003 – Aug 2004	BAT Switzerland SA, Switzerland Part-time job (25 %) in promotion and advertising
Mar 2002 – Aug 2004	Swiss Economic Institute KOF, ETH Zurich, Switzerland Part-time job (25 %) as office all-rounder
Mar 2002	Tax Office Zurich, Switzerland One-month work experience in the secretariat of the Tax Office Zurich
Apr – Sept 2001	Swisscom (telecommunication company), Switzerland Six-month work experience as office all-rounder
Jul – Nov 2000	Swiss Life (insurance company), Switzerland Five-month work experience as office all-rounder

Appendix

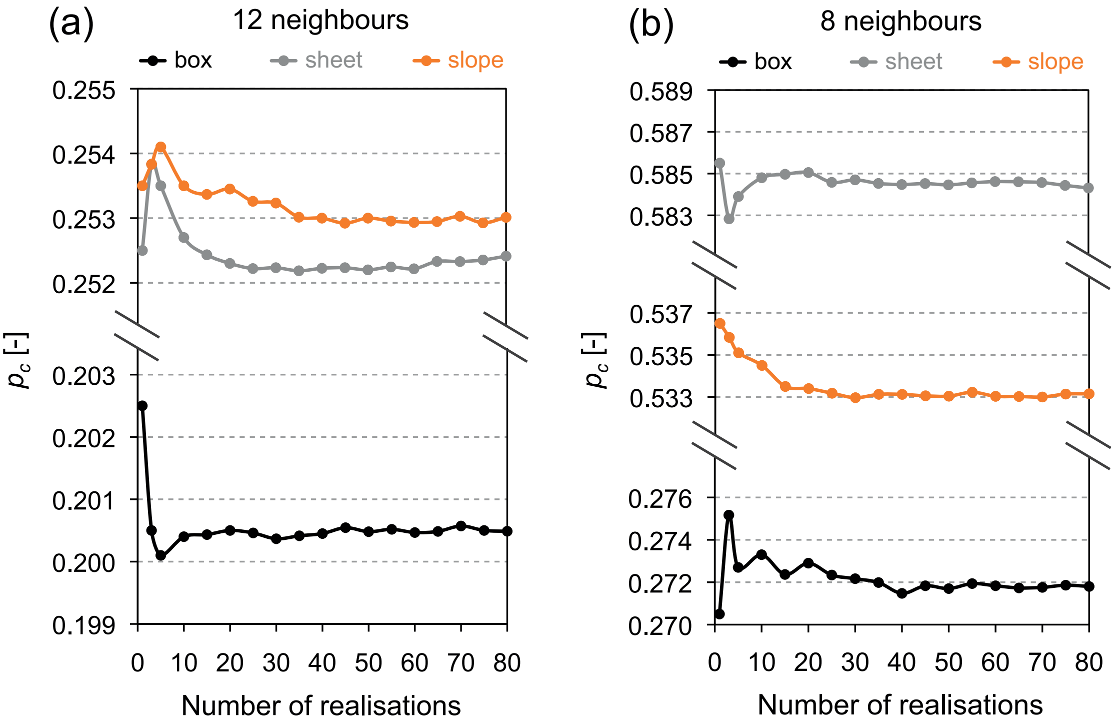

Figure A.1: Minimum number of realisations needed in order to determine the percolation threshold p_c of each of the three lattice configurations ('box', 'sheet' and 'slope') with the full fcc (a) and the modified fcc neighbourhood (b). Since after 50 realisations only the fourth decimal place of p_c was affected for all lattices, the minimum number of 50 realisations was considered appropriate to determine the percolation threshold.